

國 立 清 華 大 學

物 理 系

博 士 論 文

在質心能量為 1.8 TeV 的質子—反質子對撞機中

測量底夸克重子 Λ_b 的生命期

Measurement of Λ_b Lifetime in p pbar Collisions

At $\sqrt{s} = 1.8$ TeV

研究生: 827308 張博舜 Student: Po-Shun Chang

指導教授: 耿朝強 Advisor: Chao-Qiang Geng
鄧炳坤 Ping-Kun Teng
葉恭平 Gong-Ping Yeh

中 華 民 國 八 十 八 年 六 月

Measurement of Λ_b Lifetime in $p\bar{p}$ Collisions
at $\sqrt{s} = 1.8$ TeV

by

Po Shun Chang

A dissertation submitted in partial fulfillment
of the requirements for the degree of
Doctor of Philosophy
in Department of Physics

National Tsing Hua University

June 1999

國立清華大學博士班研究生

論文指導教授推薦書

物理

學系 張博昇
研究所

君所提之論文

Measurement of Λ_b lifetime in PP Collisions
at $\sqrt{s} = 1.8 \text{ TeV}$ (題目),

係由本人指導撰述，同意提付審查。

張朝陽

葉恭平

指導教授

鄧炳坤

(簽章)

88年6月21日

國立清華大學博士班研究生

論文口試委員審定書

物理

學系研究所 張博昇

君所提之論文

Measurement of Λ_b Lifetime in $p\bar{p}$

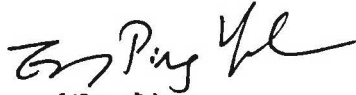
Collisions at $\sqrt{s} = 1.8$ TeV

(題目),

經本委員會審議，認為符合博士資格標準。

論文口試委員會

~~主持人~~

葉恭平 

~~召集人~~

(簽章)

委

員

王名倫

王正輝

陸達之

鄭海揚

主持人

李世名

陳錫鋒

鄧炳坤

耿朝治

中華民國 88 年 6 月 21 日

授權書
(博碩士論文)

本授權書所授權之論文為本人在 國立清華 大學(學院) 物理 系所

組 1717 學年度第 二 學期取得 博 士學位之論文。

論文名稱: 在質心能量為 1.8 TeV 的質子-反質子對撞機中
測量底夸克重子 Λ_b 的生命期

同意 不同意

本人具有著作財產權之論文全文資料，授予行政院國家科學委員會科學技術資料中心、國家圖書館及本人畢業學校圖書館，得不限地域、時間與次數以微縮、光碟或數位化等各種方式重製後散布發行或上載網路。

本論文為本人向經濟部智慧財產局申請專利的附件之一，請將全文資料延後兩年後再公開。(請註明文號:)

同意 不同意

本人具有著作財產權之論文全文資料，授予教育部指定送繳之圖書館及本人畢業學校圖書館，為學術研究之目的以各種方法重製，或為上述目的再授權他人以各種方法重製，不限地域與時間，惟每人以一份為限。

上述授權內容均無須訂立讓與及授權契約書。依本授權之發行權為非專屬性發行權利。依本授權所為之收錄、重製、發行及學術研發利用均為無償。上述同意與不同意之欄位若未鉤選，本人同意視同授權。

指導教授姓名: 耿朝強, 鄧炳坤, 葉恭平

研究生簽名: 張博舜 學號: 1827308
(親筆正楷) (務必填寫)

日期: 民國 88 年 6 月 21 日

1. 本授權書請以黑筆撰寫並影印裝訂於書名頁之次頁。
2. 授權第一項者，請再交論文一本予畢業學校承辦人員或逕寄 106-36 台北市和平東路二段 106 號 1702 室 國科會科學技術資料中心 王淑貞。(本授權書諮詢電話: 02-27377746)
3. 本授權書於民國 85 年 4 月 10 日送請內政部著作權委員會 (現為經濟部智慧財產局) 修正定稿。
4. 本案依據教育部國家圖書館 85.4.19 台(85)圖編字第 712 號函辦理。

To My Family

摘 要

費米實驗室(Fermilab)之 Tevatron 是一質心能量為 1.8 TeV 之質子—反質子對撞機. 大型高能粒子偵測器 CDF 在 1992 至 1995 年之間共搜集了總亮度為 110 pb^{-1} 的數據. 本文利用此數據測量底夸克重子 Λ_b 之生命期. 所分析的衰變模式為 $\Lambda_b \rightarrow e^+ \nu \Lambda_c^-$, 其中 Λ_c^+ 衰變為 $\Lambda \pi^+ \pi^+ \pi^-$. 藉由分析 57 ± 12 個事例之衰變長度分佈, 所測得的 Λ_b 生命期為 $\tau_{\Lambda_b} = 1.36_{-0.51}^{+0.39}(\text{stat.})_{-0.20}^{+0.19}(\text{syst.}) \text{ ps}$.

Abstract

The lifetime of the Λ_b baryon is measured using the semileptonic decay $\Lambda_b \rightarrow e^- \bar{\nu}_e \Lambda_c^+$, where $\Lambda_c^+ \rightarrow \Lambda \pi^+ \pi^+ \pi^-$ and $\Lambda \rightarrow p \pi^-$. The data sample consists of 110 pb^{-1} of $p\bar{p}$ collisions at $\sqrt{s} = 1.8 \text{ TeV}$, collected by the CDF detector at the Fermilab Tevatron collider during 1992-1995. From a fit to the decay length distribution of the $\Lambda_c^+ e^-$ system from 57 ± 12 events, the lifetime of Λ_b is measured to be $\tau_{\Lambda_b} = 1.36_{-0.51}^{+0.39}(\text{stat.})_{-0.20}^{+0.19}(\text{syst.}) \text{ ps}$.

Acknowledgement

I would like to use this opportunity to express my deep gratitude to many people who help me have a chance to do physics analysis in CDF and finish my PhD thesis. At the first, I have to thank my advisor in National Tsing Hua University(NTHU), Chao-Qiang Geng, and Prof. Darwin Chang. They taught me the fundamental knowledge of particle physics and directed me to join the high energy group in Institute of Physics, Academia Sinica(IPAS). Dr. Shih-Chang Lee and Dr. Ping-Kun Teng deserve special thanks for their efforts to organize the high energy group in IPAS and provide enough support for students to stay at Fermilab in a long-term basis.

I never forgot my first project in CDF: the SVXII simulation. Dr. Jaroslav Antoř taught me a lot in my first step toward high energy physics. When I just arrived at Fermilab, I had benefited considerably from Dr. Ping Yeh's experiences in using CDF's software. Thanks for your help.

My special thanks and acknowledgements go to my advisor in CDF, Dr. Gong-Ping Yeh, who provided me guidance and gave me support to finish this thesis. His instructions in our group meetings helped me grow up in the field of particle physics. When I was seeking for a thesis topic, it's Dr. Ting Miao who kindly showed me a way and brought me into the wonderful world of B physics. Without his help, I won't have a chance to study the lifetime of Λ_b baryon. No word can express my gratitude to him.

When I encountered difficulties in my analysis, the constant discussions from Dr. Paoti Chang, Dr. Chung-Hsiang Wang, and Dr. Yen-Chu Chen were invaluable to me. I also thanks Dr. Ming-Jer Wang for his discussion about the concepts of statistics. Many thanks to my

friends in Department of Physics of NTHU: Chan-Peng Kao, I-Jen Hsu, Chung-Yuan Ren and Ms. Kuei-Chang Peng. Without their help, I could not have been working abroad.

I can not thank my family enough for the love and support they have given me. Bina and Kevin, thanks for your accompanying with me during the past years. I am grateful to Dr. Yi-Cheng Liu, Dr. Frank Hsieh and Ms. Danny Huang Hsieh for their help in proofreading of the draft of my thesis and for their friendship to my family.

Finally, I would like to gratefully acknowledge those people who had built and operated the Tevatron collider and the CDF detector. Without their great accomplishment, this thesis is impossible.

This work was supported by Academia Sinica and National Science Council of Republic of China.

Contents

1	Introduction	1
1.1	Development of Particle Physics	2
1.2	$b\bar{b}$ Production	8
1.3	b Quark Fragmentation	12
1.4	Spectator Model of B Hadron Decay	13
1.5	Heavy Quark Effective Theory	14
1.6	Λ_b Lifetime	16
2	Experimental Apparatus	20
2.1	The Fermilab Tevatron Collider	21
2.2	Collider Detector at Fermilab	23
2.2.1	Tracking System	27
2.2.2	Calorimeter System	33
2.2.3	Muon System	37
2.2.4	Triggering	39

3	Event Selection and Reconstruction	42
3.1	Event Reconstruction	43
3.1.1	Track Reconstruction	44
3.1.2	Primary Vertex and Beam Position	45
3.2	Electron Identification	46
3.2.1	Longitudinal and Transverse Shower Sharing	46
3.2.2	Shower Profile in $r - \phi$ View and z View	49
3.2.3	Match between CTC Track and Energy Cluster	51
3.2.4	Non-B Electron Removal	51
3.3	Monte Carlo Generation	56
3.3.1	Generation of b Quarks and Λ_b Hadrons	56
3.3.2	Decay of the Λ_b Hadron	56
3.3.3	Detector Simulation	56
3.4	$e\Lambda$ Sample Selection	60
3.5	$\Lambda_c^+ \rightarrow \Lambda \pi^+ \pi^+ \pi^-$ Reconstruction	62
3.5.1	Pre-selection Cuts	66
3.5.2	Kinematics and Vertex Cuts	66
3.5.3	K_s^0 Reflection Removal and dE/dX	75
3.5.4	Λ_c Signal Result	75
3.6	Background	79
4	Lifetime Fitting	85

4.1	Λ_b Vertex and Decay Length	86
4.2	Proper Decay Length and Fitting Procedure	90
4.3	Systematic Error	99
5	Conclusion and Future Prospects	109
A	Purification of the Λ Sample	111

List of Tables

1.1	Masses and charges of quarks and leptons	8
1.2	Fundamental interactions and gauge bosons	8
1.3	Comparison of charm and B hadron lifetimes.	14
1.4	The measurements of Λ_b lifetime.	17
2.1	Geometrical parameters of SVX	31
2.2	CDF calorimeter systems.	35
3.1	Summary of electron identification cuts.	55
3.2	Generation conditions for Λ_b Monte Carlo sample in BGENERATOR.	56
3.3	Requirements for the Monte Carlo data reduction prior to detector simulation.	58
3.4	Selection requirement of Λ in the vicinity of electron.	66
3.5	$\Lambda 3\pi$ pre-selection cuts.	68
3.6	Event selection cuts for $\Lambda_c \rightarrow \Lambda 3\pi$ signal search.	78
3.7	The examples of charm mesons decays with the K_s^0 plus 3 tracks.	83
4.1	Fitting parameters.	99

4.2 Fitting parameters for two different fitting procedure and two different restricted range of $c\tau^*$ 107

4.3 Summary of systematic errors. 108

List of Figures

1.1	Leading order $b\bar{b}$ (α_s^2) production processes in $p\bar{p}$ collision.	9
1.2	Next-To-Leading order (α_s^3) $b\bar{b}$ production processes in $p\bar{p}$ collision.	10
1.3	Integrated b quark production cross section versus P_T at CDF	11
2.1	A schematic diagram of Tevatron. The position of CDF detector is shown in the diagram.	22
2.2	A side view of the CDF detector. The interaction point is at the lower right corner.	24
2.3	An isometric cut-away of CDF detector.	25
2.4	The projection of a track on the transverse plane.	27
2.5	An isometric view of SVX barrel.	29
2.6	A SVX ladder consists of 3 silicon detectors. The readout chips are at the upper end in this diagram.	30
2.7	A cross section view of VTX module(left) and a side view of a wedge (right) . .	31
2.8	CTC end plate. The structure of cell and superlayer are shown.	32
2.9	Central calorimeter wedge.	36
2.10	A schematic view of CES, showing the structure of strips and wires.	37
2.11	One wedge of central muon detector(CMU). Each wedge consists of 3 towers. .	38

2.12	Cross section view of a CMU towers. The 4×4 arrangement of CMU cells is shown.	39
3.1	The ratio of energy deposition in CHA and CEM for Run 1 inclusive electron data. The spike near zero is contributed from those electrons which were absorbed completely in CEM.	47
3.2	The multiplicity of 3-D tracks associated to electromagnetic cluster(a), and the lateral shower profile for three-tower case (b). The drop at 0.2 is due to the requirement of $L_{shr} < 0.2$ at level 3 electron trigger for two-tower cae.	48
3.3	The χ^2 of transverse profile match with test beam results, for z view strips and $r - \phi$ view wires in CES. The drops at $\chi^2 = 10$ for plot (a) and (b) are the results of level 3 electron trigger requirements for Run 1 data.	50
3.4	The x position difference between CTC track and CES wire cluster (a), and z position difference between CTC track and CES strip cluster (b) for Run 1 data.	52
3.5	The ratio of energy deposited in CEM calorimeter and momentum measured by CTC tracking chamber for electron candidates in Run 1 data.	53
3.6	(a) P_T spectrum of b quark, and (b) P_T spectrum of the semileptonic electron from BGENERATOR.	57
3.7	(a) Electron P_T spectrum before(solid line) and after(dash line) level 2 trigger simulation. The level 2 trigger efficiency is plotted in (b)	59
3.8	Cone size between daughter tracks of Λ and electron . (a) $\Delta R(e\Lambda_c)$, (b) $\Delta R(e\Lambda)$, (c) $\Delta R(e\pi_2)$ and (d) $\Delta R(ep)$, π_2 and p are daughter tracks of Λ	61
3.9	$M(e\Lambda)$ for real data(upper) and Monte Carlo(lower).	63

3.10	The distribution of Λ mass for the Λ candidates in the vicinity of electron for Run 1.	64
3.11	Λ mass for the cases of Λ_{CTC} and Λ_{SVX}	65
3.12	$M(\Lambda_c)$ in $\Lambda 3\pi$ channel with pre-selection cuts. No signal can be seen above the huge background.	67
3.13	$P_T(e)$ and $M(e\Lambda_c)$ distributions with pre-selection cuts. (a) and (b) are for real data, (c) and (d) are for Monte Carlo. The downward arrows indicate the values for final cut.	69
3.14	$P_T(\Lambda)$ and $P_T(3\pi)$ distributions with pre-selection cuts. (a) and (b) are for real data, (c) and (d) are for Monte Carlo. The downward arrows indicate the values for final cut.	70
3.15	$P_T(\Lambda_c)$ and $P_T(e\Lambda_c)$ distributions with pre-selection cuts. (a) and (b) are for real data, (c) and (d) are for Monte Carlo. The downward arrows indicate the values for final cut.	71
3.16	χ^2 of vertices fitting and $Lxy(\Lambda_c)$ significance distributions with pre-selection cuts. (a) and (b) are for real data, (c) and (d) are for Monte Carlo. The downward arrows indicate the values for final cut.	72
3.17	$Lxy(\Lambda_c)$ significance with all the other kinematic and vertex cuts(upper). After the cut $Lxy(\Lambda_c) > 1\sigma$ the signal become clear.	73
3.18	Solid(dash) line shows the result without(with) the cut $Lxy(\Lambda_c) > 1\sigma$. The signal is much better with this cut.	74
3.19	K_s^0 reflection spectrum with new mass assignment to Λ candidate (upper), and the Λ_c mass after K_s^0 reflection removal (lower).	76

3.20	Level(p) distribution for Λ_c candidates (upper), and the Λ_c mass after the cut of level(p) > 0.2.	77
3.21	The $M(\Lambda 3\pi)$ distribution of the final $\Lambda_c \rightarrow \Lambda \pi \pi \pi$ candidates. The shaded area is for wrong sign combination.	80
3.22	Data and Monte Carlo comparison for (a) $P_T(e)$, (b) $P_T(\Lambda_c)$, (c) $P_T(e\Lambda_c)$, and (d) $P_T(\Lambda)$, after side-band subtraction for the data.	81
3.23	Data and Monte Carlo comparison for (a) $P_T(3\pi)$, (b) $M(e\Lambda_c)$, and (c) impact parameter of electron D(e), after side-band subtraction for the data.	82
4.1	Schematic view of the decay $\Lambda_b \rightarrow e^- \bar{\nu}_e \Lambda_c^+ \rightarrow e^- \bar{\nu}_e \Lambda \pi^+ \pi^+ \pi^-$, in which the transverse decay length L_{xy} for Λ_b lifetime fitting is defined as the distance between (X_B, Y_B) and the primary vertex(PV).	87
4.2	Pull distribution test for (a) $V_X(\Lambda_c)$, (b) $V_Y(\Lambda_c)$, (c) $V_X(\Lambda_b)$, and (d) $V_Y(\Lambda_b)$. All the distributions are Gaussian function with mean value at 0 and width(Sigma) of about 1.	91
4.3	K factor distribution from Monte Carlo sample.	94
4.4	Pseudo proper decay length of Λ_b for side-band area events.	100
4.5	Pseudo proper decay length of Λ_b for peak area events.	101
4.6	The change in $-2 \ln L$ from its minimum as a function of $c\tau_{\Lambda_b}$	102
4.7	The comparison between input $c\tau$ and fitted $c\tau$ for 5 high statistics Monte Carlo samples. There is a shift of 15 μm in the lifetime fitting result. It's attributed to the systematic error for event selection cuts.	104

4.8	Background function(F_b) fitting for side-band area events with two different fitting procedure and two different restricted ranges of $c\tau^*$	105
4.9	Total function(F) fitting for peak area events with two different fitting procedure and two different restricted ranges of $c\tau^*$	106
A.1	Λ and its K_s^0 reflection spectrum for a Λ sample.	112
A.2	A typical relation between QCTC and particle momentum for e, μ, π, K and p	114
A.3	(upper) The Λ sample we use to study the dE/dX property of proton. (lower)After applying the cuts $ D > 3\sigma$ for p and π tracks, the signal to background ratio becomes better.	115
A.4	(upper)The normalized $\Delta QCTC$ for the p candidates in the peak area of $M(\Lambda)$ (solid line) and in the side-band (dash line). (lower) After side-band subtraction, the normalized $\Delta QCTC$ for the p candidates become a good Gaussian distribution.	116
A.5	The distribution of level(p) for proton in peak area (solid) and in side-band area (dash).	118
A.6	(a) and (c): the $M(\Lambda)$ and its K_s^0 reflection without dE/dX cut. (b) and (d): the $M(\Lambda)$ and its K_s^0 reflection with level(p) > 0.6 . The K_s^0 reflection is reduced significantly.	119

Chapter 1

Introduction

In the modern knowledge of the structure of matter, there are two major categories of fundamental building blocks, quarks and leptons. They are governed by four interactions: electromagnetic, weak, strong, and gravitational interactions. Quarks have 6 flavors: up, down, charm, strange, bottom and top. Leptons have six types: electron, muon, tau lepton and their associated neutrinos. Quarks and leptons are spin $1/2$ fermions. No free quarks have been observed. Quarks always come in the form of hadrons which consist of either 3 quarks(baryon), or quark-antiquark pairs(meson). The electromagnetic interaction is mediated by photons. The gravitational interaction is too weak to have detectable effect in the world of subatomic particles. Weak and strong interactions are mediated by the W , Z bosons and the gluon bosons respectively. This modern picture of fundamental particles and interactions took its shape from the results of numerous experiments in conjunction with a series of theoretical developments.

The developments of particle physics keep moving forward nowadays. Among the several important developments, the studies of CP violation in the B physics play a key role in answering the asymmetry between matter and antimatter. From the year 2000, a blooming era of B physics study is going to start. The knowledges of the B hadrons' fundamental properties, e.g., the masses and lifetimes, are necessary for the further studies of B physics. In this thesis we report

a lifetime measurement of Λ_b , the ground state of B baryon.

In section 1.1 we briefly describe how the experimental results and theoretical concepts pushed this field forward. We introduce the mechanism of b quarks production and fragmentation in section 1.2 and section 1.3. In section 1.4 we describe a simple model of the B hadron decays. The formal treatment is introduced in section 1.5. The Λ_b lifetime predictions and current measurements are described in section 1.6.

1.1 Development of Particle Physics

Electron is the first known fundamental particle. It was discovered by J. J. Thomson in cathode ray experiments in 1897. The uranic radiation, discovered by Becquerel in 1896, was soon to be realized to have at least two components, α - and β - particles, among them the β -particles were identified as electrons because of the same e/m ratio.

The energy spectrum of β -particle revealed a mystery. The α -particle carry discrete energy which was measured to be equal to the energy difference between the initial state and final state of the nucleus that the α -particle is emitted from. On the contrary, the β -particle has a continuous spectrum, and the emitted energy is smaller than the energy released by the decayed nucleus. The phenomena of missing energy found in β -particles emission violated the energy conservation law. This puzzle was resolved in 1933 by W. Pauli, who postulated that there exists a new particle which always accompanies the electron in the process of β -particle emission. This new particle was named neutrino ¹ and was discovered experimentally in 1956 [1].

Rutherford proposed a nuclear model of atom in 1911 based on the results of α -particles

¹Neutrino was named by Fermi. At the beginning Pauli called it neutron.

scattering experiment. In this model, atoms are made of electrons and protons. Later on a neutral particle, the neutron, was postulated to be another component inside the nucleus in addition to protons.

In 1932, Chadwick discovered neutron [2]. It brought new impact on nuclear physics. Fermi pointed out that the decay process of neutron into proton and electron-neutrino pair is the underlying mechanism behind the phenomena of β -particles emission. In 1934, Fermi proposed a theory of β decay and introduced the weak interaction. The weak interaction was later on described as mediated by the W boson in 1958 [3, 4]. In this model, the electron and its corresponding neutrino are the decay products of the W boson. In the theory of weak interaction, e and ν_e form a weak doublet $\begin{pmatrix} \nu_e \\ e \end{pmatrix}$.

From the subsequent nuclear physics studies it was gradually realized that the force binding protons and neutrons together within the nucleus was a new interaction, which is effective in short ranges and strong enough to overcome the electromagnetic repulsion between the protons. In 1935 Yukawa proposed a meson theory [5] in which he used the process of meson exchange between protons and neutrons to explain the nuclear force. The meson mass was estimated to be about 200 times of the electron mass based on the interaction range of the nuclear force. In 1936 a new particle with a mass of about 207 times of electron mass was discovered [6]. In the beginning, it was thought to be Yukawa's meson and named as the μ meson. But this new particle did not interact with the nucleus strongly enough to explain the nuclear force. The true Yukawa meson was discovered in 1947 by Powell [7], and was named as the π meson.

The μ meson mentioned above in fact is a cousin of the electron, and was appropriately named muon. Its associated neutrino was discovered in 1962 [8]. The two-family picture of $\begin{pmatrix} \nu_e \\ e \end{pmatrix}$ and $\begin{pmatrix} \nu_\mu \\ \mu \end{pmatrix}$ was extended to three families when τ , the tau lepton, was discovered in

1975 at SLAC [9, 10]. Because e , μ , τ and their associated neutrinos are not involved in strong interaction, they are called leptons.

Proton, neutron and π meson are classified as hadrons because they interact via the strong interaction with nucleus. After the discovery of the pion, more hadrons were found in cosmic rays and accelerator experiments, including K , Λ , Δ , Σ , Ξ ... etc. The facts that these hadrons can decay to other particles and that there are too many hadrons imply that there should exist another type of fundamental particles. In 1961 Gell-Mann and Ne'eman proposed a $SU(3)$ scheme to explain the family structure of hadrons [11, 12], and predicted a new hadron Ω . After the discovery of Ω in 1964, Gell-Mann and Zweig proposed that all hadrons are made of more fundamental particles, which they named "quarks". In this model there were three flavors of quarks: u , d and s . It explained the experimental results very well. But there was one conflict. In this model, Ω was made of 3 identical spin 1/2 s quarks, all in the same quantum state. It violated the Fermi-Dirac statistics. It was gradually realized that quarks should carry a new attribute, the color charge. Since hadron's color charges can not be detected experimentally, the bound states of quarks have to be colorless.

Color charges exist in three types, which may be called red, blue and green. They are the coupling charges of strong interaction which is mediated by spin 1 gluon bosons, just like the electric charge couples to electromagnetic interactions mediated by photons. A major difference between photon and gluon is that the gluon carry color charge while the photon does not carry electric charge. For electromagnetic interaction, an electric charge is surrounded by a cloud of photons and electrons generated in vacuum polarization. This is a screening effect. The effective strength of electrical coupling is stronger when two charges are closer. For the strong interaction, the gluon-gluon interaction will contribute an opposite effect to vacuum polarization and cause anti-screening effect. The coupling strength becomes smaller when two

quarks come closer. This is known as the asymptotic freedom. On the other hand, when two quarks move farther away, their coupling become stronger, eventually a new quark pair will be pulled out from the vacuum. Therefore, no free quark can exist. This effect is known as the color confinement. Asymptotic freedom and color confinement are two important features of the strong interaction. A $SU(3)_c$ non-Abelian gauge theory, known as quantum chromodynamics (QCD), can explain the behavior of asymptotic freedom and is thought to be the correct theory of strong interaction.

In the deep inelastic scattering experiment conducted in 1968 [13, 14], the proton was found to be consisted of partons. Among them some were identified as quarks. This experiment turned the "quark" from a theoretical concept into a physical object. Besides the valence quarks ($u u d$), the constituents of proton also include gluons and sea quarks. In the proton and antiproton collisions, the heavy quark pair production is contributed significantly from the gluon gluon interactions.

In the quark model, the neutron β decay can be explained by the process $d \rightarrow u + e^- + \bar{\nu}_e$. That means the u and d quarks are involved in the weak interaction and can also form a doublet $\begin{pmatrix} u \\ d \end{pmatrix}$, just like the $\begin{pmatrix} \nu_e \\ e \end{pmatrix}$ doublet. But actually the doublet structure among quarks is more complex. The strange meson decay $K^+ \rightarrow \pi^0 e^- \bar{\nu}_e$ can be explained by the corresponding quark level decay $s \rightarrow u + e^- + \bar{\nu}_e$, which implied that u and s might also form a doublet. In 1963 Cabibbo proposed a quark mixing theory in which d and s are mixed by an angle θ_c [15]. The u quark actually form a doublet with one of the mixing states of d and s quark as in the form of $\begin{pmatrix} u \\ d \cos \theta_c + s \sin \theta_c \end{pmatrix}$. However, one new problem was induced. This theory allowed the decay $K^0 \rightarrow \mu^+ \mu^-$, which was not observed in experiments. In 1970 Glashow, Iliopoulos and Maiani extended Cabibbo's theory and introduce a new flavor of quark, named the charm quark [16]. In this new model the charm quark and another mixing state of d and s quarks form a new

doublet of $\begin{pmatrix} c \\ -d \sin \theta_c + s \cos \theta_c \end{pmatrix}$. This new model is known as GIM mechanism. It eliminated the problem of the decay $K^0 \rightarrow \mu^+ \mu^-$ and gained its evidence when the bound state of $c \bar{c}$, the J/ψ meson, was discovered in 1974 [17, 18].

The quark mixing suggested in the GIM mechanism can be expressed by a mixing matrix, as follows,

$$\begin{pmatrix} d' \\ s' \end{pmatrix} = \begin{pmatrix} \cos \theta_c & \sin \theta_c \\ -\sin \theta_c & \cos \theta_c \end{pmatrix} \cdot \begin{pmatrix} d \\ s \end{pmatrix} \quad (1.1)$$

the d' and s' are called the weak eigenstates because they are coupled to the W bosons in the weak interaction. While the d and s are called the mass eigenstates.

More experimental results kept coming out to stimulate new concepts in quark model. In 1964 J. Cronin and V. Fitch observed the CP violation in the K^0 decay. With the structure of four quarks arranged in two families, it would need new mechanism to explain the phenomena of CP violation. In 1973 Kobayashi and Maskawa proposed that the phenomena of CP violation can be accommodated automatically if the two-family quark model is generalized to three-family [19]. In this theory they introduced two new quarks, the bottom(b) quarks and the top(t) quarks. The b quarks were discovered in 1977 by a Fermilab fixed-target experiment through the decay of $b\bar{b}$ bound states, the Υ mesons, to dimuon state [20]. The t quarks were discovered in 1995 by the CDF collaboration at Fermilab [21].

The mixing of three quark families is expressed as in the following equation,

$$\begin{pmatrix} d' \\ s' \\ b' \end{pmatrix} = V_{CKM} \cdot \begin{pmatrix} d \\ s \\ b \end{pmatrix} \quad (1.2)$$

where V_{CKM} is a 3×3 matrix,

$$V_{CKM} = \begin{pmatrix} V_{ud} & V_{us} & V_{ub} \\ V_{cd} & V_{cs} & V_{cb} \\ V_{td} & V_{ts} & V_{tb} \end{pmatrix} \quad (1.3)$$

The elements in the matrix V_{CKM} exhibit a hierarchy structure; the diagonal elements are of the order of unity, while the off-diagonal elements are roughly suppressed by the powers of the factor $\sin \theta_c \sim 0.22$. A more intuitive parameterization method to manifest this characteristic was proposed by Wolfenstein [22], as follows,

$$V_{CKM} = \begin{pmatrix} 1 - \lambda^2/2 & \lambda & A\lambda^3(\rho - i\eta) \\ -\lambda & 1 - \lambda^2/2 & A\lambda^2 \\ A\lambda^3(1 - \rho - i\eta) & -A\lambda^2 & 1 \end{pmatrix} \quad (1.4)$$

where λ is equivalent to $\sin \theta_c$, A , ρ and η are real numbers being of the order of unity. The existence of the complex term $i\eta$ in the 3×3 V_{CKM} matrix gives a room to describe the CP violation. In a 2×2 matrix the complex term can always be absorbed by re-defining the quark fields, therefore it is impossible to explain the CP violation for the case of 2-family quark model. On the complex plane the points $(0,0)$, $(1,0)$ and $(\rho, i\eta)$ form a triangle. The measurements of the three angles associated with this triangle are the key issue in the study of the CP violation.

Masses and charges of the quarks and the leptons are listed in Table 1.1. The hierarchy structure among quark masses is essential to our understanding of the hadrons. It is worth noting that the t quark mass is too heavy such that the semileptonic decay of $b \rightarrow t\ell^- \bar{\nu}_\ell$ is forbidden kinematically. The major semileptonic decay of b quark is $b \rightarrow c\ell^- \bar{\nu}_\ell$. However, the b quark to c quark decay is suppressed by the off-diagonal element V_{cb} in the V_{CKM} matrix. This suppression enhances the B hadron lifetimes significantly. The basic interactions except the gravitation are also summarized in Table 1.2.

Quarks			Leptons		
flavor	mass (GeV/c ²)	charge	flavor	mass (GeV/c ²)	charge
u	0.0015 - 0.005	2e / 3	ν_e	$< 1.5 \times 10^{-8}$	0
d	0.003 - 0.009	-e / 3	e	5.11×10^{-4}	-e
c	1.1 - 1.4	2e / 3	ν_u	$< 1.7 \times 10^{-4}$	0
s	0.06 - 0.17	-e / 3	μ	0.1057	-e
t	173.8 ± 5.2	2e / 3	ν_τ	< 0.018	0
b	4.1 - 4.4	-e / 3	τ	1.777	-e

Table 1.1: Masses and charges of quarks and leptons

Interaction	Mediate Boson	Range
Electromagnetic	γ	∞
Weak	W^\pm and Z	$\sim 10^{-18}$ m
Strong	gluons	$\sim 10^{-15}$ m

Table 1.2: Fundamental interactions and gauge bosons

1.2 $b\bar{b}$ Production

A static proton can be thought of as the combination of the valance quarks: (u, u, d) . However, in a dynamics situation like the $p\bar{p}$ collisions at $\sqrt{s} = 1.8$ GeV at Tevatron, the contributions from other partons like gluons and sea quarks have to be considered as well. Each parton possesses a fraction of proton's momentum. The probability of finding a parton carrying a momentum fraction x is described by the parton distribution function (PDF) $F_i(x, Q^2)$, where i is the parton type and Q^2 is the momentum transfer. The parton distribution functions are measured from the processes such as the deep inelastic scattering, Drell-Yan, jet and direct photon production. Several groups have been providing regular updates on the PDF when new data or theoretical developments are available. In the hadron collider experiments, the PDF provided by two major groups, the Martin-Roberts-Stirling(MRS) group [23, 24] and the

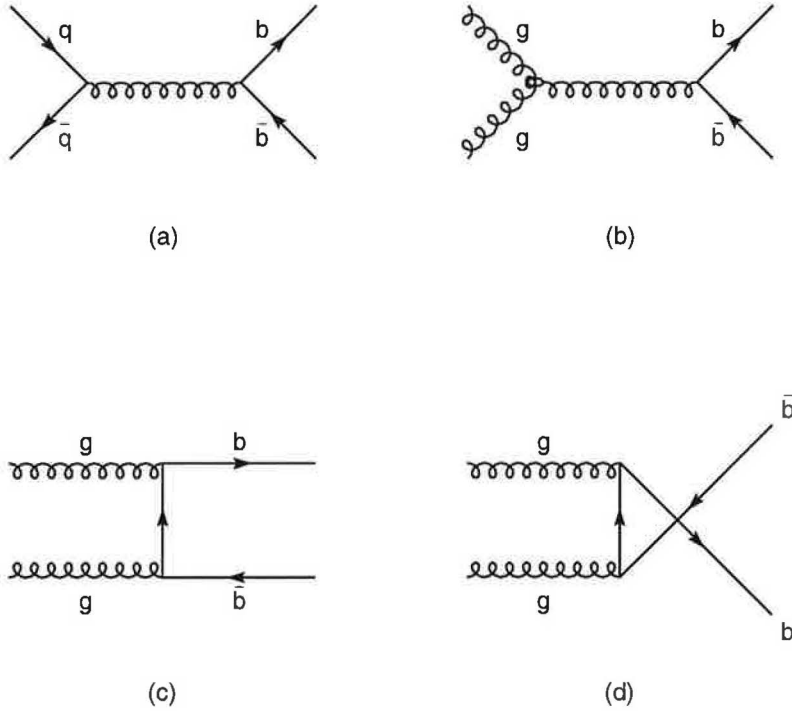


Figure 1.1: Leading order $b\bar{b}$ (α_s^2) production processes in $p\bar{p}$ collision.

CTEQ group [25], are commonly used.

In $p\bar{p}$ collisions, the $b\bar{b}$ pairs are produced via the hard scattering of partons inside p and \bar{p} . The Feynman diagrams of the leading order(LO) processes are shown in Figure 1.1, in which 1.1a is called the quark-antiquark annihilation process, and 1.1b-d are the gluon-gluon fusion processes.

When the quark mass is similar to or greater than the average momentum carried by each parton, the production will be dominated by quark-antiquark annihilation process. At Tevatron the average momentum is about $\langle x \rangle (\sqrt{s}/2) \sim 90$ GeV where $\langle x \rangle$ is the average momentum carried by each parton and is about 10% of the proton momentum. Therefore, the gluon-gluon

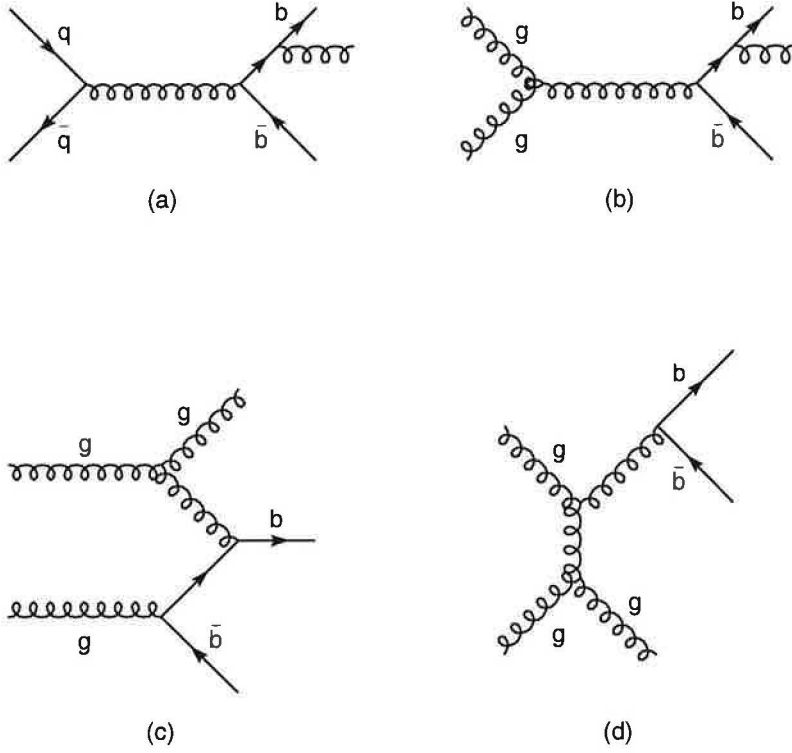


Figure 1.2: Next-To-Leading order (α_s^3) $b\bar{b}$ production processes in $p\bar{p}$ collision.

fusion processes dominate the $b\bar{b}$ production, in contrast to the $t\bar{t}$ production, where the quark-antiquark annihilation dominates. As a result, the next-to-leading order (NLO) contributions of $b\bar{b}$ production are not just correction terms; they are actually as important as leading order contributions. Some of the NLO processes are shown in Figure 1.2. Among them, 1.2a-b are gluon radiation processes, 1.2c is flavor excitation process, 1.2d is gluon splitting process. The complete contributions from NLO processes had been calculated by Nason, Dawson and Ellis (NDE) [26]. The b quark production cross section had been measured at CDF through several B decay channels. Figure 1.3 shows the results in a comparison to the NDE calculation.

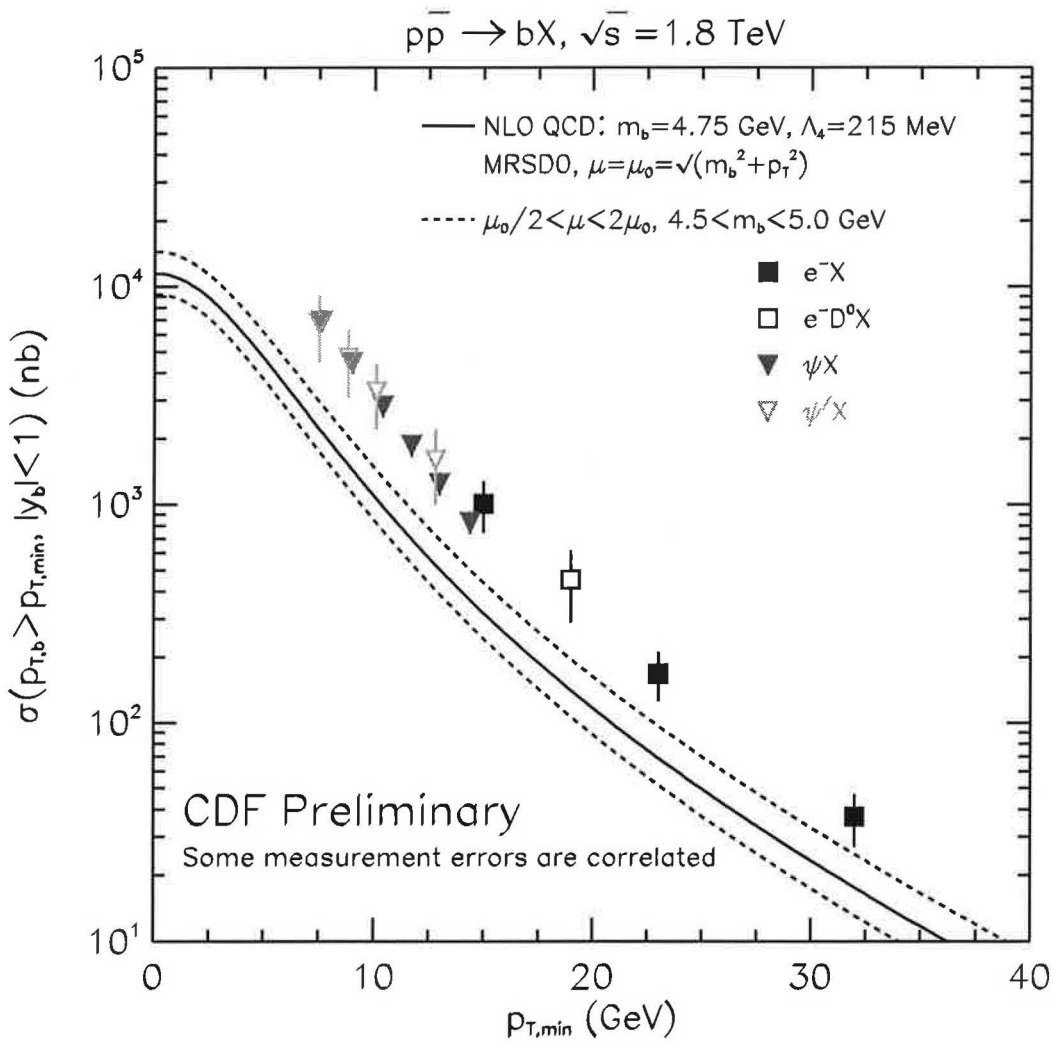


Figure 1.3: Integrated b quark production cross section versus P_T at CDF

The b and the \bar{b} produced via the leading order process are always back-to-back in ϕ -coordinate. In the next-to-leading order processes, a gluon or third light quark is involved in the calculation so that in this case b and \bar{b} are not back-to-back. For the gluon splitting case, the b and the \bar{b} can actually come very close to each other.

1.3 b Quark Fragmentation

When a b quark is produced, since it carries color charge, it will pull out a quark pair $q\bar{q}$ from the vacuum and form a hadron with the antiquark \bar{q} . Usually q is the light quarks such as u or d quark and sometimes it's s quark. If there is enough energy, the other quark q will also pull out another quark pair. This process is referred to as fragmentation or hadronization. Unlike the $b\bar{b}$ production, in which the hard scattering between partons is calculable by the theory of perturbative QCD(pQCD), fragmentation is a soft process and can not be calculated using pQCD. Usually fragmentation is described by phenomenological models. For collider environments, the Peterson model is commonly used [27]. This model describes the fragmentation by using the function $D_Q^H(z)$ which gives the probability of generating hadron H in the fragmentation of quark Q with energy-momentum fraction z . $D_Q^H(z)$ is expressed in equation (1.5),

$$D_Q^H(z) = \frac{1}{z[1 - 1/z - \epsilon_Q/(1 - z)]^2} \quad (1.5)$$

where the fraction z is defined as

$$z = \frac{E_H + P_{||}(H)}{E_Q + P_Q}, \quad (1.6)$$

with $P_{||}(H)$ being the hadron momentum component parallel to the parent quark. The ϵ_Q in equation (1.5) is an input parameter to be determined from experimental results. For the case of b quark fragmentation, $\epsilon_b = 0.006 \pm 0.001 \pm 0.002$ [28].

1.4 Spectator Model of B Hadron Decay

The hadron decay processes are difficult to calculate because of the involvement of soft processes which are beyond the regime of perturbative QCD. The semileptonic decay, on the other hand, is of special interest from the experimental and theoretical point of views. From the experimental aspect, the lepton produced in this decay mode is easier to be identified in the detector. From the theoretical aspect, since the lepton is not involved in the strong interaction, the lepton part can be decoupled from the hadron part in certain approximations and simplify the calculation. In addition, there is one more advantage in B hadron decays. Since the b quark is heavy, the semileptonic decay of the bound state $b\bar{q}$ meson or bqq' baryon is dominated by the process $b \rightarrow c\ell\bar{\nu}_\ell$, where $qq' \in (u, d, s)$. This approximation is called the *spectator model*, where the contribution from the light quark is neglected. The decay widths of B hadrons have similar expression as the μ decay:

$$\Gamma_{b \rightarrow c\ell\bar{\nu}_\ell} = \frac{G_F^2 m_b^5}{192\pi^3} |V_{cb}|^2 f(m_c/m_b) \quad (1.7)$$

where $f(x)$ is the phase space factor,

$$f(x) = 1 - 8x^2 + 8x^6 - x^8 - 24x^4 \ln x \quad (1.8)$$

and

$$x = \frac{m_c}{m_b} \quad (1.9)$$

In the spectator model, all the B hadrons have equal lifetimes, so do the charm hadrons if we take c quark as heavy quark. In Table 1.3 we compare the lifetimes of B hadrons and charm hadrons [29, 30]. The spectator model predictions fit the data much better for the B hadron sector than the charm hadron sector. It can be explained by the fact that the mass

of b quark is heavier than the mass of c quark, and therefore the spectator approximation is more reasonable for b quark. However, the differences among the lifetimes of B hadrons are distinguishable in current experimental precision. To explain these differences, we need to consider the non-spectator effects such as final state interference, annihilation diagram, and helicity suppression.

charm hadron lifetime		B hadron lifetime	
$\tau(D^0)$	0.415 ± 0.004 ps	$\tau(B^-)$	1.66 ± 0.03 ps
$\tau(D^+)$	1.057 ± 0.015 ps	$\tau(\bar{B}^0)$	1.55 ± 0.03 ps
$\tau(D_s)$	0.467 ± 0.017 ps	$\tau(\bar{B}_s^0)$	1.47 ± 0.06 ps
$\tau(\Lambda_c)$	0.206 ± 0.012 ps	$\tau(\Lambda_b)$	1.19 ± 0.05 ps

Table 1.3: Comparison of charm and B hadron lifetimes.

1.5 Heavy Quark Effective Theory

With the developments in B hadron theory, the corrections for the above intuitive phenomenological picture can be treated in a systematical way based on the following features of B hadrons [31],

$$M_b \gg \Lambda_{QCD} \gg M_q$$

where Λ_{QCD} is the QCD scale, ~ 0.2 GeV. The momentum transfer between the heavy quark b and the other light quark \bar{q} is of the order of Λ_{QCD} . The light quark mass M_q is smaller than the Λ_{QCD} (for the case of u and d quarks) or of the same order of Λ_{QCD} (for the case of s quark). Inside the B hadron, the light quark q is strongly fluctuated and therefore is treated as a light cloud surrounding the b quark. On the other hand, the heavy quark mass $M_b \sim 4.5$ GeV is about 20 times of the Λ_{QCD} ; the creation and annihilation processes of $b\bar{b}$ could not occur from the gluon field fluctuation. Therefore the quantum field theoretical treatment of b quark

can be simplified to a quantum mechanical treatment, in which the b quark serves as a static color charge source just like the nucleus providing static electrical charge source in atoms.

The above features of B hadrons bring a way to construct an effective QCD theory to treat B hadrons formally. We use the example of neutron β decay to illustrate the concept of effective theory. In the electroweak theory the neutron β decay is described by the propagation of a virtual weak gauge boson W^* between d quark and u quark, as follows,

$$\begin{aligned} d &\rightarrow W^{*-}u \\ W^{*-} &\rightarrow e^-\bar{\nu}_e \end{aligned}$$

The virtual W^* boson only lives over a short interval of time $\sim 1/M_W$. For a low energy effective theory, the W field as well as the gluon fields inside the neutron and proton can be integrated out, resulting a theory with the four-field operator $\psi_n\psi_p\psi_e\psi_{\nu_e}$ and a new vertex coupling $G_F/\sqrt{2}$. In fact this is the original β decay theory which Fermi proposed to explain the neutron β decay.

For the effective theory of B hadron decays, two fields are integrated out. At the first, the b quark is almost static inside B hadron, the antiparticle part of the Dirac spinor for the b quark ψ_b is not involved in the decay process and can be integrated out. This is also called the *Nonrelativistic Expansion*. Secondly, the high frequency components of the gluon fields and the b quark field are also integrated out because they are calculable using pQCD. The scale μ_{had} separating the high frequency and low frequency has to be larger than Λ_{QCD} to ensure the strong coupling constant $\alpha_s(\mu_{had})$ to be in the perturbative region. On the other hand, in order to expand this effective theory in the powers of $1/M_b$, the μ_{had} has to be smaller than M_b . Usually it is selected as about $2 \sim 3 \Lambda_{QCD}$. This step is an application of the *Operator Product*

Expansion. This theory is called the heavy quark effective theory(HQET). The characteristic energy scales involved in the HQET are listed below.

$$M_W \gg M_b \gg \mu_{had} \gg \Lambda_{QCD} \gg M_q$$

1.6 Λ_b Lifetime

HQET is useful in describing the B hadrons and charm hadrons spectroscopy as well as the lifetimes. Several groups had predicted the individual B hadron lifetimes and their ratio in the framework of HQET. The earliest predictions made by M. Neubert [32] are shown in equation (1.10).

$$\begin{aligned} \frac{\tau(B^-)}{\tau(B_d)} &= 1 + O(1/M_b^3) \\ \frac{\tau(B_s)}{\tau(B_d)} &= (1.00 \pm 0.01) + O(1/M_b^3) \\ \frac{\tau(\Lambda_b)}{\tau(B_d)} &= 0.98 + O(1/M_b^3) \end{aligned} \tag{1.10}$$

One of the other major predictions by I. Bigi [33] are also shown in equation (1.11),

$$\begin{aligned} \frac{\tau(B^-)}{\tau(B_d)} &= 1 + 0.05 \cdot \left[\frac{f_B}{200 \text{ MeV}} \right]^2 \\ \frac{\tau(B_s)}{\tau(B_d)} &\approx 1 \\ \frac{\tau(\Lambda_b)}{\tau(B_d)} &\approx 0.9 \end{aligned} \tag{1.11}$$

where f_B is the B meson form factor, ~ 200 to 250 MeV. The predictions of lifetime ratios for $\frac{\tau(B^-)}{\tau(B_d)}$ and $\frac{\tau(B_s)}{\tau(B_d)}$ are consistent with the experimental results. However, the $\frac{\tau(\Lambda_b)}{\tau(B_d)}$ ratio in

data is much smaller than the theoretical prediction, as shown in Table 1.3. The Λ_b lifetime measurements from the collaborations of ALEPH, DELHPI, and OPAL at LEP and the CDF Collaboration at Tevatron are shown in Table 1.4.

Experi.	Data set	# of event	Method	τ_{Λ_b} (ps)	Ref.
ALEPH	(91-95) 4×10^6 Z	$705 \pm 32 \pm 62$	$\Lambda \ell^-$	$1.20 \pm 0.08 \pm 0.06$	[34]
		137 ± 2	$\Lambda_c^+ \ell^-$ $\left\{ \begin{array}{l} \Lambda_c^+ \rightarrow pK^- \pi^+ \\ \Lambda_c^+ \rightarrow pK_s^0 \\ \Lambda_c^+ \rightarrow \Lambda \pi^+ \\ \Lambda_c^+ \rightarrow \Lambda \pi^+ \pi^+ \pi^- \end{array} \right\}$	$1.18^{+0.13}_{-0.12} \pm 0.03$	
		$39.5^{+1.8}_{-2.8}$	$\Lambda \ell^- \ell^+$	$1.30^{+0.26}_{-0.21} \pm 0.04$	
DELHPI	(91-94) 3.6×10^6 Z	82 ± 9	$\Lambda_c^+ \ell^-$ $\left\{ \begin{array}{l} \Lambda_c^+ \rightarrow pK^- \pi^+ \\ \Lambda_c^+ \rightarrow pK_s^0 \\ \Lambda_c^+ \rightarrow pK_s^0 \pi^+ \pi^+ \end{array} \right\}$	$1.11^{+0.19}_{-0.18} \pm 0.05$	[35]
		235 ± 25	$p \ell^-$	$1.19 \pm 0.14 \pm 0.07$	
OPAL	(90-94) 3.6×10^6 Z	490	$\Lambda \ell^-$ i.p.	$1.21^{+0.15}_{-0.13} \pm 0.10$	[36]
		356	$\Lambda \ell^-$ vtx.	$1.15 \pm 0.12 \pm 0.06$	
	(90-95) 4.4×10^6 Z	129 ± 25	$\Lambda_c^+ \ell^-$ $\left\{ \Lambda_c^+ \rightarrow pK^- \pi^+ \right\}$	$1.29^{+0.24}_{-0.22} \pm 0.06$	[37]
CDF	(92-95) 110 pb^{-1}	197 ± 25	$\Lambda_c^+ \ell^-$ $\left\{ \Lambda_c^+ \rightarrow pK^- \pi^+ \right\}$	$1.32 \pm 0.15 \pm 0.06$	[38]

Table 1.4: The measurements of Λ_b lifetime.

The ratio $\frac{\tau(\Lambda_b)}{\tau(B_d)}$ from LEP's measurements is 0.78 ± 0.04 [39], which is significantly reduced compared to the theoretical predictions. If the measurement of this ratio remains the same in future results, it might indicate that the assumption behind the heavy quark effective theory, the quark-hadron duality, has to be re-examined seriously. If the duality violation is true, then we can not trust the predictions of semileptonic branching ratio and charm yield in B decays, which are considered to be sensitive to new physics, within the framework of heavy quark expansion [40]. However, it is worth mentioning that the result from CDF's measurements is

0.87 ± 0.11 [38], which is closer to the predicted values. This result is based on the 197 ± 25 signal events in the channel $\Lambda_b \rightarrow \Lambda_c^+ \ell^- \bar{\nu}$, where $\Lambda_c^+ \rightarrow pK^-\pi^+$. The resolution is limited by the statistical uncertainty. It is of great interest to increase the statistics for the the Λ_b lifetime measurement from CDF's current data and, if possible, to clarify the problem of " Λ_b lifetime puzzel" [40]. Below we discuss the major methods for Λ_b lifetime measurement.

The best channel to study Λ_b lifetime is the decay channle $\Lambda_b \rightarrow J/\psi\Lambda$. But due to the low statistics for the Λ_b events currently collected and the low branching ratio of the J/ψ decay, so far the major measurements are from the data of Λ_b semileptonic decay $\Lambda_b \rightarrow \Lambda_c^+ \ell^- \bar{\nu}_\ell$, in which the Λ_c^+ is reconstructed through several methods, as described below:

- $\Lambda\ell^-$: In this method, the Λ_c^+ is reconstructed from the inclusive decay $\Lambda_c^+ \rightarrow \Lambda X$. The signal is determined from the excess of the right sign pair $\Lambda\ell^-$ over the wrong sign pair $\Lambda\ell^+$. The Λ_b lifetime is determined from the fit of the lepton impact parameter distribution or the fit of Λ_b proper decay length distribution. For the latter fit, the Λ_b vertex is reconstructed from the intersection points of Λ and lepton.
- $\Lambda\ell^-\ell^+$: In this method, the Λ_c^+ is reconstructed from the semileptonic decay $\Lambda_c^+ \rightarrow \Lambda\ell^+\nu_e$. The signal is the right sign pair $\Lambda\ell^+$ with invariant mass $M(\Lambda\ell^+) < 2.3 \text{ GeV}/c^2$ and the combination of $\Lambda\ell^-\ell^+$ with the invariant mass $M(\Lambda\ell^-\ell^+) > 2.3 \text{ GeV}/c^2$. The Λ_b vertex is determined from the intersection point of ℓ^- and ℓ^+ .
- $\Lambda_c^+\ell^-$: In this method, the Λ_c^+ is fully reconstructed from its hadronic decays such as $\Lambda_c^+ \rightarrow pK^-\pi^+$ and $\Lambda_c^+ \rightarrow \Lambda\pi^+\pi^+\pi^-$. The signal is the peak in the $M(\Lambda_c^+)$ spectrum with right charge correlation with the ℓ^- . The Λ_b vertex is determine from the intersection point of lepton and Λ_c^+ .

Among the above methods, the $\Lambda_c^+\ell^-$ method provides the best signal against the background and gives the best quality of Λ_b vertex. Therefore, in this thesis we attempt to fully reconstruct the Λ_c^+ from another channel: $\Lambda_c^+ \rightarrow \Lambda\pi^+\pi^+\pi^-$ in a hope to increase the statistics.

The chapter 2 of this thesis is dedicated to introducing the experimental facilities used for the events producing, data collecting and physics analyzing. The methods for the events selection and reconstruction are described in chapter 3. The lifetime fitting result is presented in chapter 4. The chapter 5 gives the conclusion of this analysis and its prospects in the future.

Chapter 2

Experimental Apparatus

The advances of particle physics rely heavily on the progress of particle acceleration and detection techniques. In this chapter, we describe the accelerator and detector systems used to obtain data for this analysis. The process of accelerating p and \bar{p} to collide with each other at center-of-mass energy $\sqrt{s} = 1.8$ TeV is described in section 2.1. The Collider Detector at Fermilab (CDF) is a hybrid of various detector components, including tracking chambers, calorimeters, front-end electronics, and on-line computer clusters. They are discussed in section 2.2 with emphasis on the components responsible for the track detection and energy measurement.

The data used in this analysis were collected during Tevatron Run 1, which started in Dec. 1992 and ended in Feb. 1996. Run 1 comprised of three separate data-taking periods, i.e., Run 1A Dec. 1992 - Jun. 1993, Run 1B Dec. 1993 - Jul. 1995 and Run 1C Dec. 1995 - Feb. 1996. Among them, Run 1C was dedicated to a special trigger data set, and not used in this analysis. The total integrated luminosity delivered to CDF during Run 1 was about 175 pb^{-1} . The collected integrated luminosity was 19 pb^{-1} for Run 1A, 90 pb^{-1} for Run 1B and 10 pb^{-1} for Run 1C. This analysis is based on the data collected in Run 1A and 1B, about 110 pb^{-1} in total.

2.1 The Fermilab Tevatron Collider

In the Tevatron, the proton accelerating process begins with an electrostatic accelerator called Cockcroft-Walton, which can be thought of as a 750 KV DC voltage source, where gaseous hydrogens are ionized into H^- ions and accelerated to 750 KeV. The resulting negative hydrogen ion beams are directed into a linear accelerator Linac, which consists of 5 drift tubes and 9 side-coupled cavities. Unlike the DC acceleration in Cockcroft-Walton, the charged ions are accelerated through AC electromagnetic wave generated by these cavities in Linac. As a result, the original continuous beams are separated into several pulses. After traveling through the 500 feet long Linac, the ion beams can be accelerated to 400 MeV.

The next stage is a synchrotron accelerator named Booster. Before the H^- ion beams enter Booster, they have to pass through a thin carbon foil to strip the two associated electrons. In Booster the resulting proton beam circulates around 20,000 times until they are accelerated to 8 GeV. Then, the proton beam is injected into another synchrotron accelerator Main Ring, which is 4 miles in circumference.

If running in fixed target mode, the proton beam will be switched to the Tevatron when they reach 150 GeV. While in collider mode, when the proton beam is accelerated to 120 GeV a fraction of it will be extracted to bombard a Tungsten target to produce antiprotons. The newly produced antiprotons have a wide spread in energy and direction. These randomly moving antiprotons are directed into the Debuncher to reduce their random motion through an important process known as stochastic cooling [41]. The cooled-down antiprotons are stored in the Antiproton Storage Ring. After sufficiently accumulated, the antiprotons are injected back into the Main Ring. When the energy of protons and antiprotons reach to 150 GeV, they are transferred to Tevatron where they will be accelerated to 900 GeV. The Tevatron shares

the same tunnel with the Main Ring, but it employs superconductor dipole magnets to provide strong magnetic field to bend these high energy protons and antiprotons. Inside the Tevatron, the proton and the antiproton beams are both divided into 6 bunches, each with length of ~ 30 cm. A schematic diagram of Tevatron is shown in Figure 2.1.

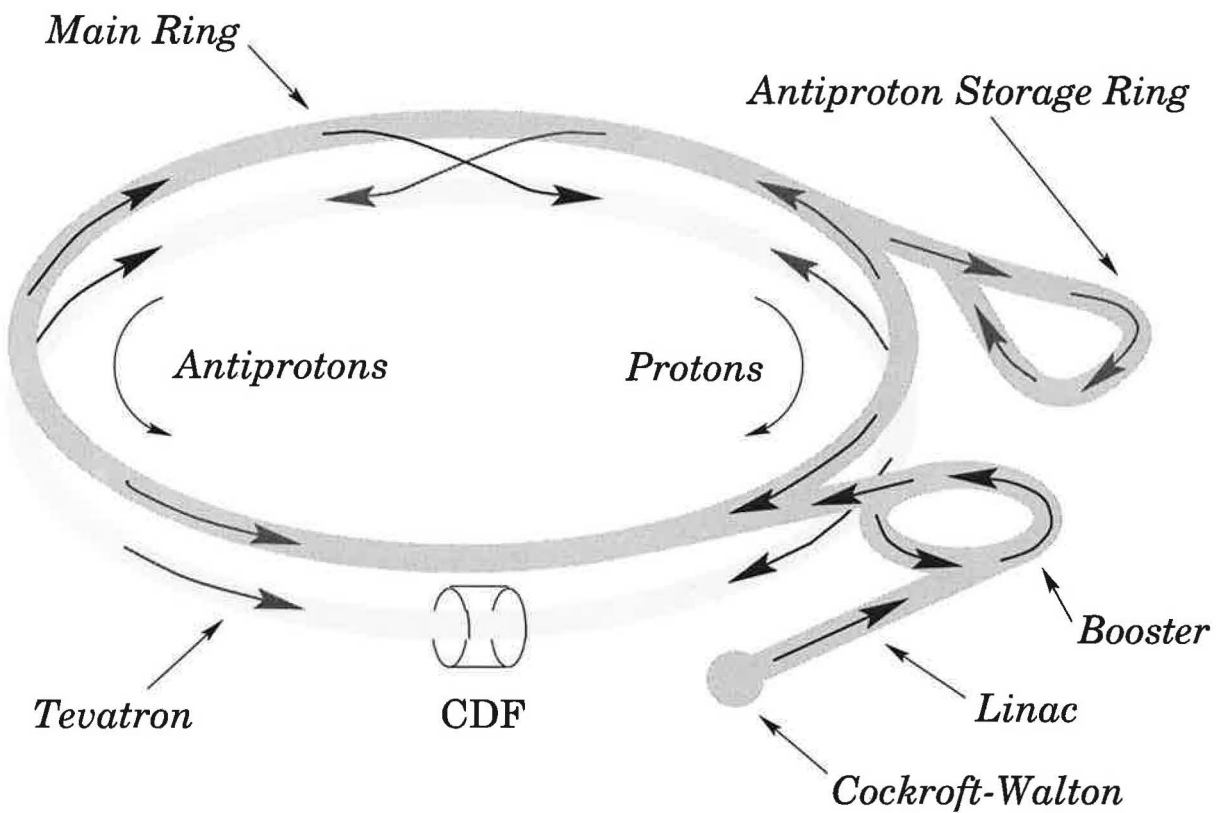


Figure 2.1: A schematic diagram of Tevatron. The position of CDF detector is shown in the diagram.

Along the Tevatron, there are two $p\bar{p}$ collision points, each with a separate collider detector: D0 and CDF. The quadrupole magnets at both ends of CDF focus the beams into a small

transverse cross sectional area with a radius of about $35 \mu\text{m}$. The instantaneous luminosity (L) can be expressed as

$$L = \frac{N_p N_{\bar{p}} N_B f}{4\pi\sigma_A^2} \quad (2.1)$$

where N_p and $N_{\bar{p}}$ are the numbers of particle in proton and antiproton bunches, about 2×10^{11} and 6×10^{10} respectively. N_B is the number of bunches, which is 6 in Run 1 operation mode. f is the revolution frequency at which proton or antiproton travel around the Tevatron, about 45K Hz. σ_A is the cross sectional area, about $(35 \mu\text{m})^2$. The average instantaneous luminosity for Run 1A and 1B were $0.54 \times 10^{31} \text{ cm}^{-2}\text{s}^{-1}$ and $1.6 \times 10^{31} \text{ cm}^{-2}\text{s}^{-1}$ respectively.

The $p\bar{p}$ collisions occur when two bunches are crossing each other. The collision points are peaked roughly at the center of the detector, forming a Gaussian distribution with $\sigma = 30$ cm along z direction. The time between each crossing is $3.5 \mu\text{s}$. It's an important parameter in detector design, especially for the front-end readout system. In each crossing there could be more than one $p\bar{p}$ collisions. They are called pile-up events. In the Tevatron, the average number of $p\bar{p}$ collisions in each crossing is 1.8 for Run 1A and 2.7 for Run 1B, respectively.

2.2 Collider Detector at Fermilab

The CDF detector [42] is a general-purpose detector designed for many topics of particle physics with $p\bar{p}$ collisions. This detector is capable of studying top, QCD, electroweak and heavy flavor physics, as well as searching for exotic particles. In the Tevatron, the proton and the antiproton beams are unpolarized and make head-on collision at the same energy. Accordingly, the detector is nearly cylindrically symmetric around the beam direction, and has forward-

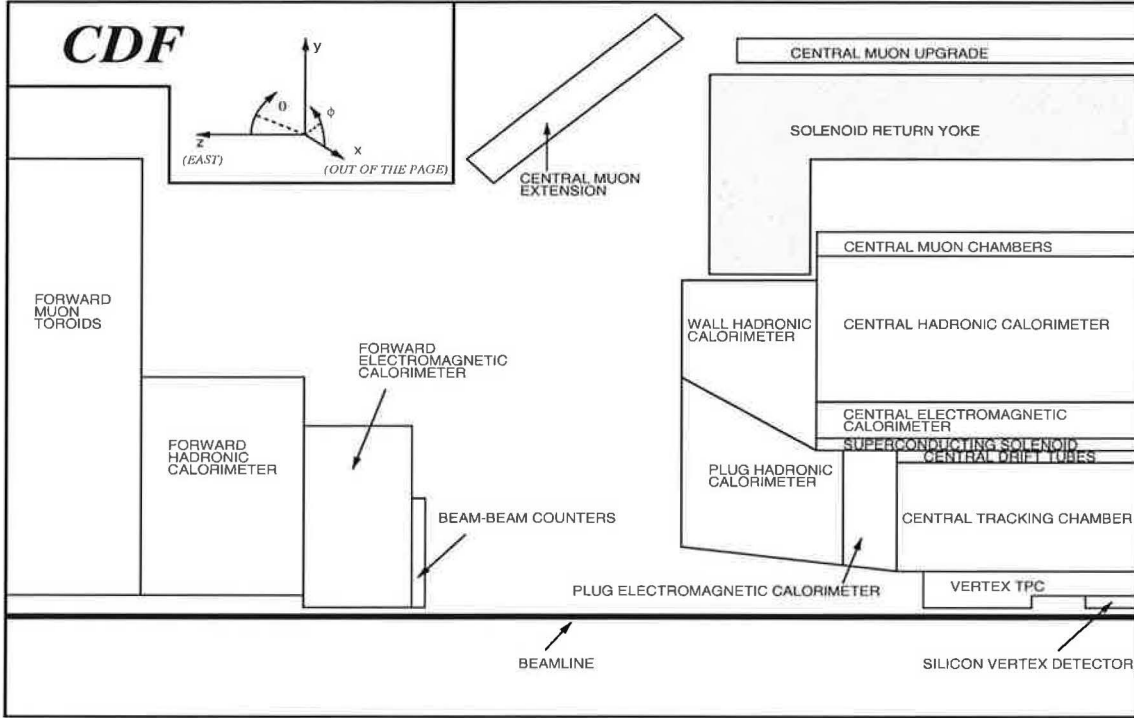


Figure 2.2: A side view of the CDF detector. The interaction point is at the lower right corner.

backward symmetry with respect to the interaction point. Figure 2.2 shows the side view of the CDF detector as well as the coordinate system. Figure 2.3 provides an isometric view.

A natural choice of z -axis in the CDF coordinate system is the beam direction. Positive z -axis is pointing to proton beam direction, positive x -axis is pointing outward horizontally and y -axis is pointing upward. The polar angle θ is measured from positive z -axis. A quantity called rapidity, defined as

$$y = \frac{1}{2} \ln\left(\frac{E + P_z}{E - P_z}\right) \quad (2.2)$$

is often used instead of the polar angle θ in the laboratory coordinate frame. Under a boost in z

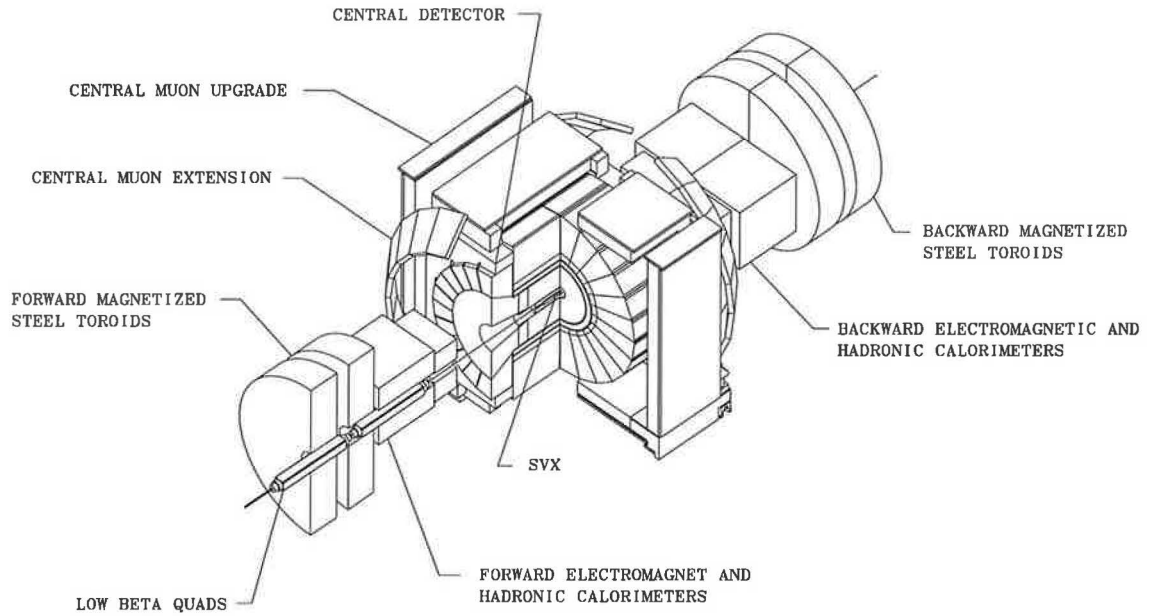


Figure 2.3: An isometric cut-away of CDF detector.

direction with velocity β , the rapidity will transform up to a constant, namely, $y' = y + \tanh^{-1} \beta$. The advantage is that the shape of rapidity distribution, dN/dy , is invariant under the Lorentz transformation. For high energy particles, $E \gg m$, the rapidity can be approximated by pseudo-rapidity,

$$\eta = \frac{1}{2} \ln \left(\frac{P + P_z}{P - P_z} \right) = -\ln \tan \left(\frac{\theta}{2} \right) \quad (2.3)$$

After being produced in the $p\bar{p}$ collisions, the particles will travel through the tracking system, which is enclosed by a superconducting solenoid providing a 1.4 T axial magnetic field. The tracks of charged particles in the magnetic field are helical curves with the helix axis parallel to Z-axis. The projection on the transverse plane is a circle, as shown in Figure 2.4. At CDF there are 5 tracking parameters used to describe a track : $(\cot \theta , C , Z_0 , D_0 , \phi)$ where θ is the polar angle, $\cot \theta = P_Z/P_T$. For a particle with charge Q , the half curvature C is equal to $1/2Q\rho$, ρ is radius of the circle on transverse plane. C is proportional to the inverse of transverse momentum P_T and has the same sign as charge. Z_0 is the z position of the closest approach point relative to the coordinate origin. D_0 is the minimum distance between the helix and the origin on transverse plane, as indicated in Figure 2.4. $D_0 = Q \cdot (\sqrt{x_0^2 + y_0^2} - \rho)$, (x_0, y_0) is the center position of circle. ϕ is the azimuthal angle at the closest approach point. D_0 is called the impact parameter. With properly translating the coordinate system from detector center to beam position in offline analysis, D_0 can be a good indication to distinguish tracks from the primary vertex and the secondary vertex.

Outside the tracking system is the the calorimeter system, including electromagnetic and hadronic calorimeters. Hadrons, electrons and photons deposit most of their energy in the calorimeter system.

Unlike hadrons and electrons, muons only deposit minimum ionization energy in the calorimeters. In order to identify muons, the muon systems located outside the calorimeter system are used.

The further details of the tracking system, calorimeter system and muon system are addressed in the following sections. In addition, the triggering method is also discussed.

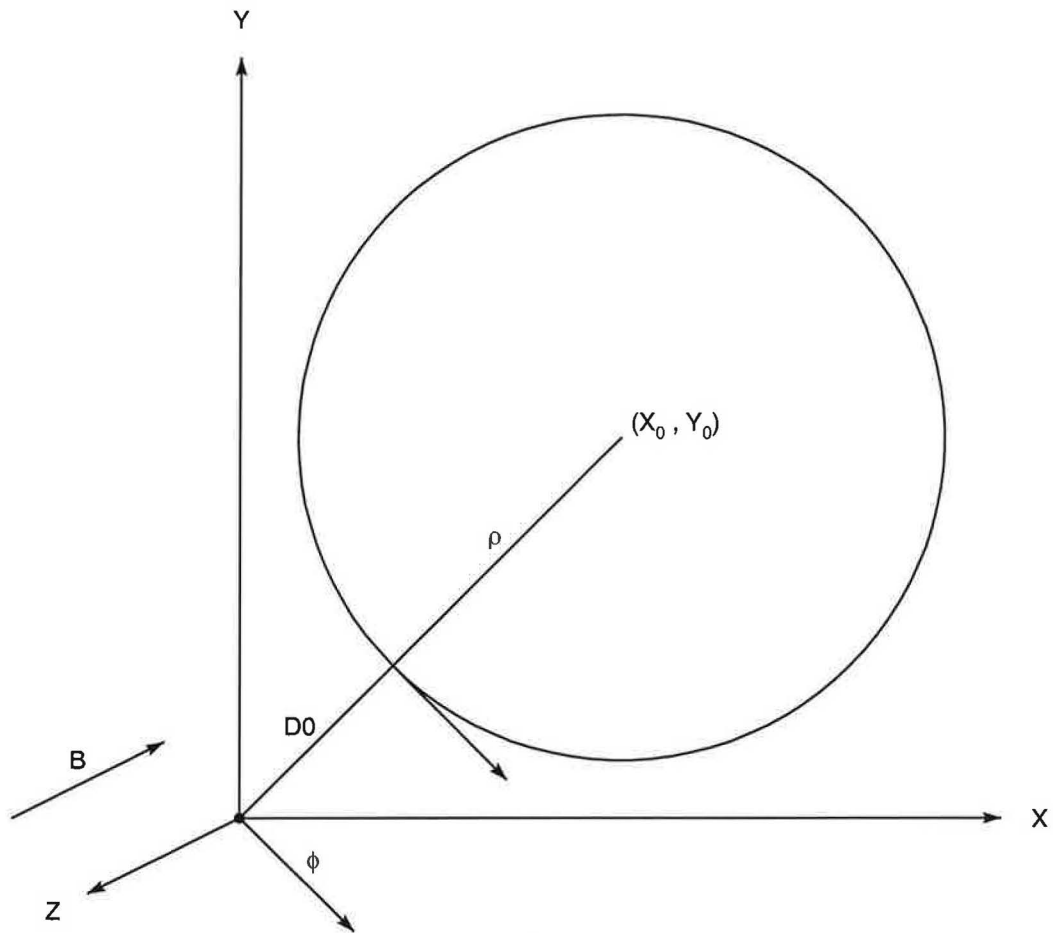


Figure 2.4: The projection of a track on the transverse plane.

2.2.1 Tracking System

There are three types of detectors in the tracking system. SVX is a silicon vertex detector providing excellent resolution in vertex and impact parameter measurements, and therefore

plays an important role in detecting events with B decays. VTX is a time projection chamber, used for the z position measurements of the primary vertices in an event. CTC is a central tracking chamber, which provides good track finding efficiency as well as good P_T measurement resolution for charged particles.

SVX

The SVX detector [43] consists of two identical barrels positioning along the z direction at both sides of the detector center. There is a gap of 2.15 cm between these two barrels. One of the barrels is shown in Figure 2.5. The length of SVX in z direction is 51 cm . Because the spread of $p\bar{p}$ collisions is about 30 cm, the geometrical acceptance of SVX is about 60 % .

Each barrel comprised 4 concentric layers of silicon microstrip detectors. The radii of these 4 layers are 3.0, 4.2, 5.7 and 7.9 cm. The 2π azimuth coverage of each layer is constructed from 12 identical ladders. The ladders at outer layers are wider to ensure the 30° coverage at different radius. The 4 ladders in the same azimuthal direction form a wedge. The detector read the data out by wedges.

The ladder structure is shown in Figure 2.6. Each ladder consists of three 8.5 cm long, $300\ \mu\text{m}$ thick rectangular silicon sensors. There are hundreds of metal strips on the surface of the silicon sensor. These strips run in the z direction and can provide $r - \phi$ hit information for tracks. The bulk of silicon sensor is p-type while underneath the metal strips are n-type regions. The interface of p-type and n-type region form a p-n junction. With proper reverse bias voltage the p-n junction becomes depletion region. When charged particles pass through the silicon sensor, a few thousand to hundred thousand electron-hole pairs are generated in the depletion region and collected by the metal strips. The pitches, or the separation between strips, are $60\ \mu\text{m}$ for the inner three layers and $55\ \mu\text{m}$ for the outermost layer. The hit resolution resulted

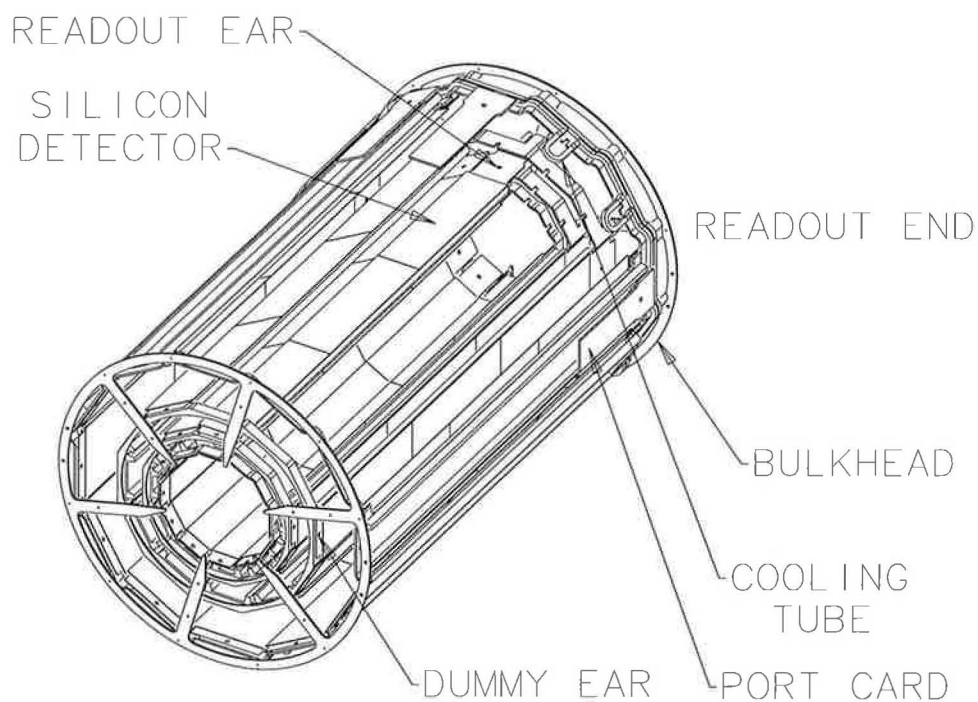


Figure 2.5: An isometric view of SVX barrel.

from these fine strips are $10\ \mu\text{m}$ to $25\ \mu\text{m}$, depending on the number of fired strips. The typical value is $15\ \mu\text{m}$. The impact parameter resolution can reach $50\ \mu\text{m}$ for tracks with $P_T \sim 1\ \text{GeV}$ and $15\ \mu\text{m}$ for tracks with $P_T \sim 10\ \text{GeV}$.

During the Run 1A data taking period, SVX had experienced a performance degradation due to radiation damage. For Run 1B, SVX was replaced with a new silicon detector SVX', featuring a higher radiation hardness, and lower noise level. In other aspects, SVX and SVX' had similar configuration.

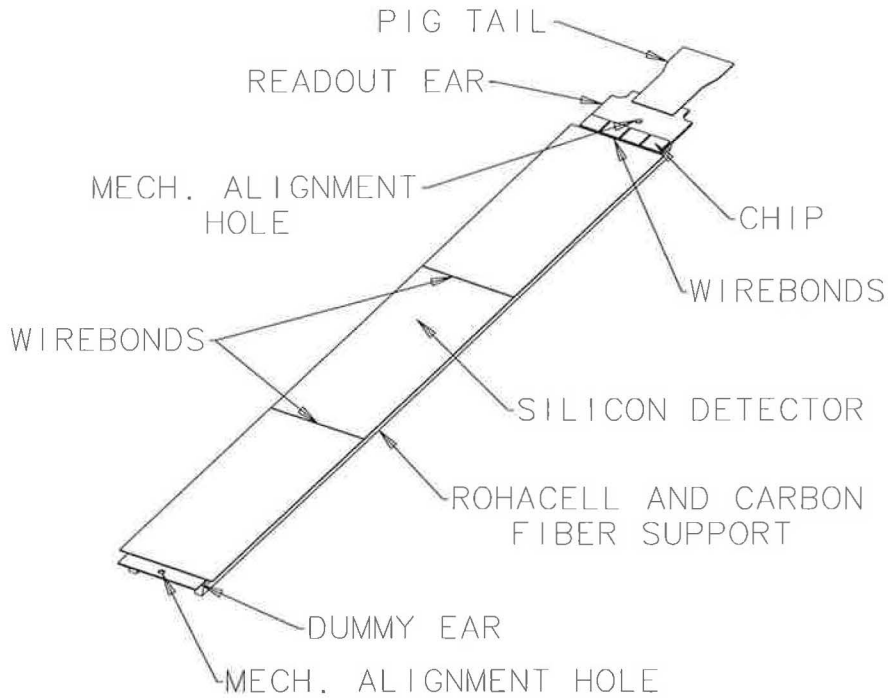


Figure 2.6: A SVX ladder consists of 3 silicon detectors. The readout chips are at the upper end in this diagram.

VTX

VTX is a time projection chamber to determine the z position of primary vertex candidates. This detector consists of 8 octagonal modules. Each module is 31 cm long and consists of 8 wedges. The active area of the chamber extends from the outside of SVX detector to $r=21$ cm. A central high voltage grid divides each module into two 15.25 cm long drift regions. This length ensures that the maximum drifting time will be smaller than the time between bunch-bunch crossing, $3.5 \mu\text{s}$. The endcaps of each module is also divided into 8 wedges. Each wedges has 24 sense wires and 24 cathode pads. The arrival time of electrons detected by these sense wires provides the $r - z$ hit information of tracks. Primary vertices in each event are obtained by fitting the tracks in $r - z$ plane. The primary vertex z resolution is about 1 mm.

layer	radius (cm)	pitch (um)	number of channel
0	2.9899	60	256
1	4.2710	60	384
2	5.7022	60	512
3	7.8508	55	768

Table 2.1: Geometrical parameters of SVX

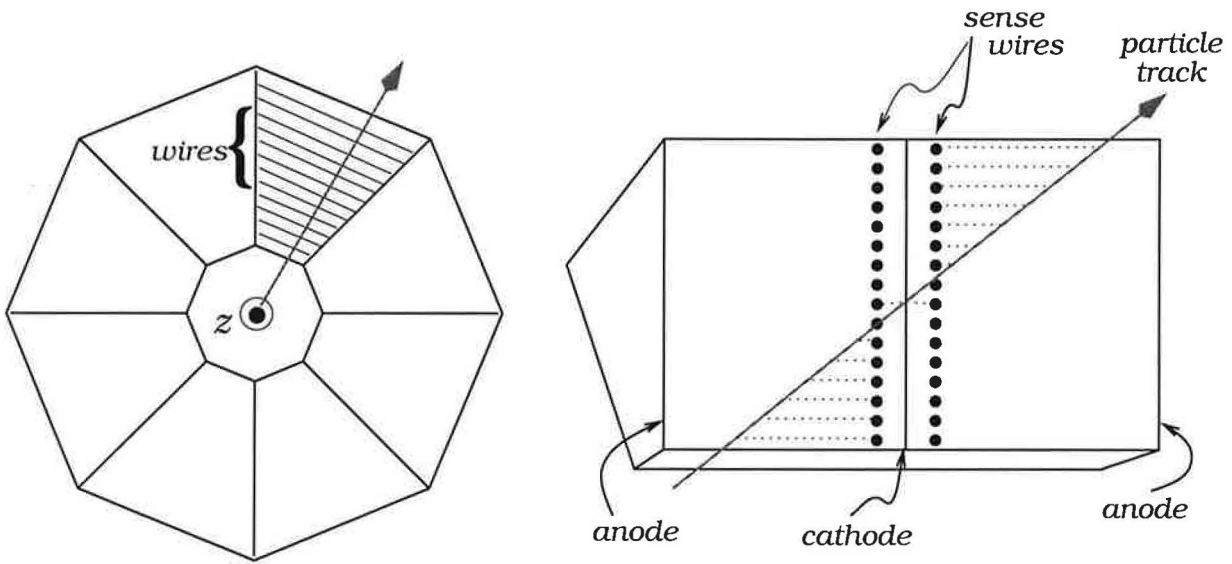


Figure 2.7: A cross section view of VTX module(left) and a side view of a wedge (right) .

CTC

CTC [44] is a cylindrical wire chamber, located outside the VTX detector, and covers the detector region of radius from 30 cm to 130 cm. Its length is 320 cm, covering η range from -1.1 to 1.1 . There are 84 layers of sense wires in CTC, grouped into 9 superlayers. Five of which are axial superlayers containing 12 sense wires each, the other four are stereo superlayers with 6 sense wires each. In axial superlayer the sense wires are in z direction. They can provide the hits in $r - \phi$ view. In stereo superlayers, the wires have an angle of $\pm 3^\circ$ with respect

to z direction. They can provide the hits in $r - z$ view. The wire spacing is 10 mm. The hit resolution is $200 \mu\text{m}$ and 0.6 cm in $r - \phi$ view and $r - z$ view, respectively. Within each superlayer, the sense wires in all layers form cell structures with a tilt angle of 45° with respect to the radial direction. Figure 2.8 shows one of the end plates of CTC, in which the structure of tilt cells is visible. Inside the cell a set of field-shaping wires can provide electric field at 1350 V/cm .

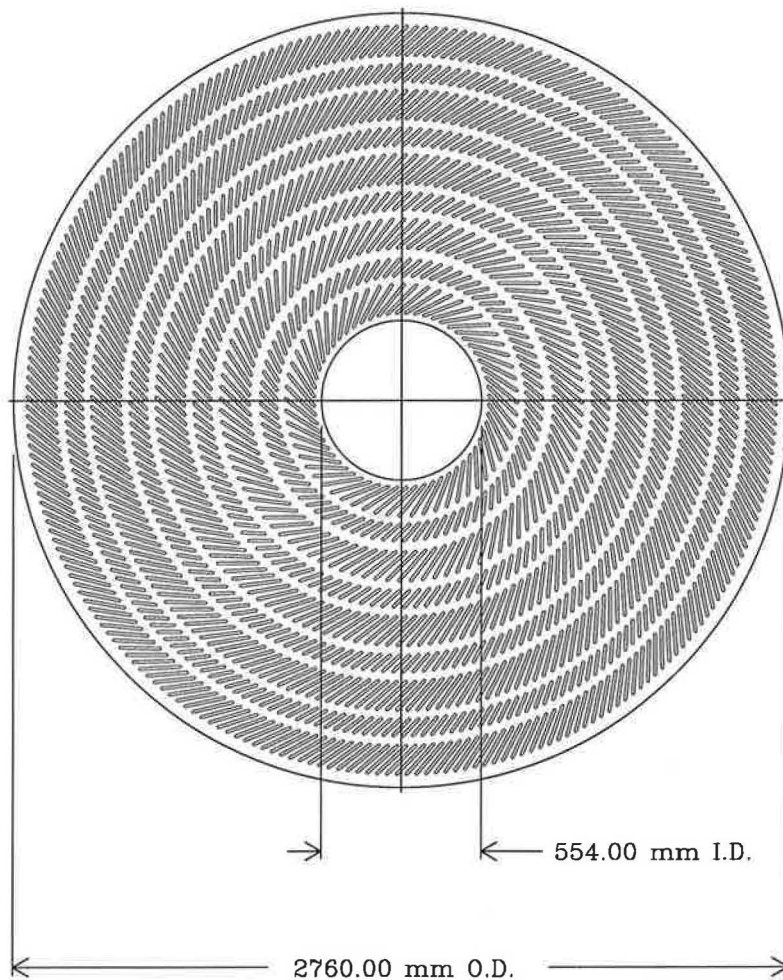


Figure 2.8: CTC end plate. The structure of cell and superlayer are shown.

The CTC chamber is filled with argon-ethane-alcohol gas mixture. When charged particles pass through the chamber, the gas molecules will be ionized. The ionization electrons will move toward the sense wires under the influence of the electric field. With the presence of electric field (1350 V/cm) and magnetic field (1.4 T), the electrons actually do not drift along the E-field. There is an angle between drifting direction and E-field, called Lorentz drifting angle. The 45° tilt angle for each cell is designed to compensate the effect of Lorentz drifting angle and ensure the ionization electrons can drift azimuthally. The hit positions are calculated based on the drift time of the ionization electrons. The maximum drift time for CTC in Run 1 is 800 ns, which is much less than the bunch crossing time of 3.5 μ s.

The momentum resolution of CTC is about

$$\frac{\delta P_T}{P_T} = 0.002 P_T. \quad (2.4)$$

The combined CTC-SVX fitting can provide a better resolution of

$$\frac{\delta P_T}{P_T} = \sqrt{0.0066^2 + (0.0009 P_T)^2}. \quad (2.5)$$

In each sense wire, the pulse heights resulted from the deposition of ionization electrons are recorded as well. The pulse heights are proportional to energy loss of the tracks. In offline analysis stage, the energy loss (dE/dX) information is used for the identification of charged particles.

2.2.2 Calorimeter System

Outside the tracking system and the solenoid is the calorimeter system. Hadrons, electrons and photons will deposit their energy in the calorimeter through different mechanisms. Hadrons

lose their energy through nuclear interactions. The characteristic length in hadron energy loss has a relation with the calorimeter material,

$$\lambda_0 \sim 35 \text{ g cm}^{-2} A^{1/3} \quad (2.6)$$

where λ_0 is the interaction length. Electrons and photons lose their energy through bremsstrahlung and pair production processes. The characteristic length is:

$$X_0 = \frac{716.4 \text{ g cm}^{-2} A}{Z(Z+1) \ln(287/\sqrt{Z})} \quad (2.7)$$

X_0 is the radiation length. The different energy loss mechanism can be used to distinguish between different particles. Two different types of calorimeter are used in CDF: the electromagnetic(EM) calorimeter with lead (Pb) as absorber to detect electrons and photons, and the hadronic(HA) calorimeter with iron as absorber to detect hadrons. Electrons and photons will be absorbed in electromagnetic calorimeter with only small leakage into hadronic calorimeter, while hadrons will penetrate deeper into the hadronic calorimeter. The energy sharing between EM and HA calorimeters is used in electron identification. The calorimeter systems, as shown in Table 2.2, cover a broad range in η from -4.2 to 4.2 with several components. In the central region ($|\eta| < 1.1$), there are central electromagnetic calorimeter (CEM) and central hadronic calorimeter (CHA). A wall hadronic calorimeter(WHA) is used to complete the η coverage of CHA. The plug calorimeters PEM, PHA, and forward calorimeters FEM, FHA cover different η ranges. In this analysis only CEM and CHA are used.

The central calorimeter is divided into two halves at $\theta = 90^\circ$. Each half is 2.5 m long and segmented into 24 wedges in azimuthal direction and 10 towers in η direction. The size of each

System	Tower size	η Range	Absorber	Medium	Depth	Energy Resolution
CEM	$15^\circ \times 0.1$	$ \eta < 1.1$	Lead	Scint.	$18 X_0$	$13.7\%/\sqrt{E_T} \oplus 2\%$
CHA	$15^\circ \times 0.1$	$ \eta < 0.9$	Iron	Scint.	$4.5 \lambda_0$	$50\%/\sqrt{E_T} \oplus 3\%$
WHA	$15^\circ \times 0.1$	$0.7 < \eta < 1.3$	Iron	Scint.	$4.5 \lambda_0$	$75\%/\sqrt{E} \oplus 4\%$
PEM	$5^\circ \times 0.1$	$1.1 < \eta < 2.4$	Lead	Gas	$18-21 X_0$	$22\%/\sqrt{E} \oplus 2\%$
PHA	$5^\circ \times 0.1$	$1.3 < \eta < 2.4$	Iron	Gas	$5.7 \lambda_0$	$106\%/\sqrt{E} \oplus 6\%$
FEM	$5^\circ \times 0.1$	$2.2 < \eta < 4.2$	Lead	Gas	$25 X_0$	$26\%/\sqrt{E} \oplus 2\%$
FHA	$5^\circ \times 0.1$	$2.4 < \eta < 4.2$	Iron	Gas	$7.7 \lambda_0$	$137\%/\sqrt{E} \oplus 3\%$

Table 2.2: CDF calorimeter systems.

tower is $0.1 \times 15^\circ$ in the $\eta - \phi$ space. These towers form a projective geometry, with the towers pointing to the interaction region. One of the wedge with the structure of 10 towers is shown in Figure 2.9. In the central region, the phase space of $\eta \times \phi = 2.2 \times 2\pi$, i.e., the range of η from -1.1 to 1.1 and ϕ from 0 to 2π , is covered by 480 calorimeter towers.

CEM & CES

CEM [45] is located at the front side of central calorimeter tower. There are 30 layers of 3.2 mm lead absorber sandwiched between 31 layers of 5 mm polystyrene scintillator in CEM. Total length of CEM is 34.5 cm, equivalent to 18 radiation length. When electrons or photons enter CEM, they develop electromagnetic showers. In order to measure the shower position and shower profile, a central electromagnetic strip chamber (CES) [46] is installed between 8th lead layer and 9th scintillator layer in CEM. This position corresponds to 5.9 radiation length. At this depth electromagnetic showers reach the maximum lateral profile. Figure 2.10 shows the schematic plot of CES. For each segment there are 64 wires running in z direction providing $r - \phi$ positions of showers and 128 strips perpendicular to z direction providing z positions. Each of the 69 strips at the end near $\theta = 90^\circ$ has a width of 1.67 cm, and the other 59 strips

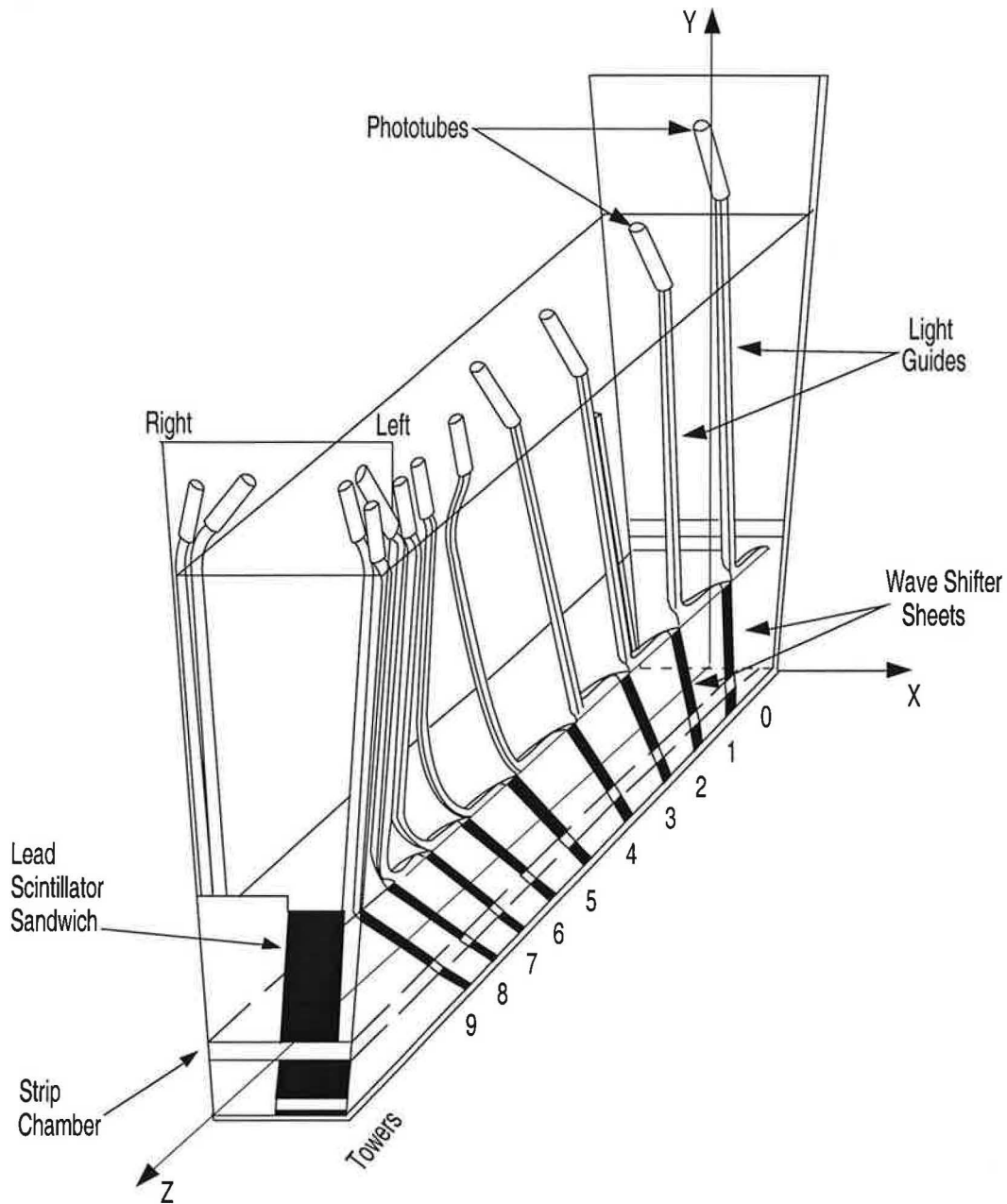


Figure 2.9: Central calorimeter wedge.

at the farther end have a width of 2.01 cm. The position resolution obtained from 50 GeV electron test beam data is 2 mm.

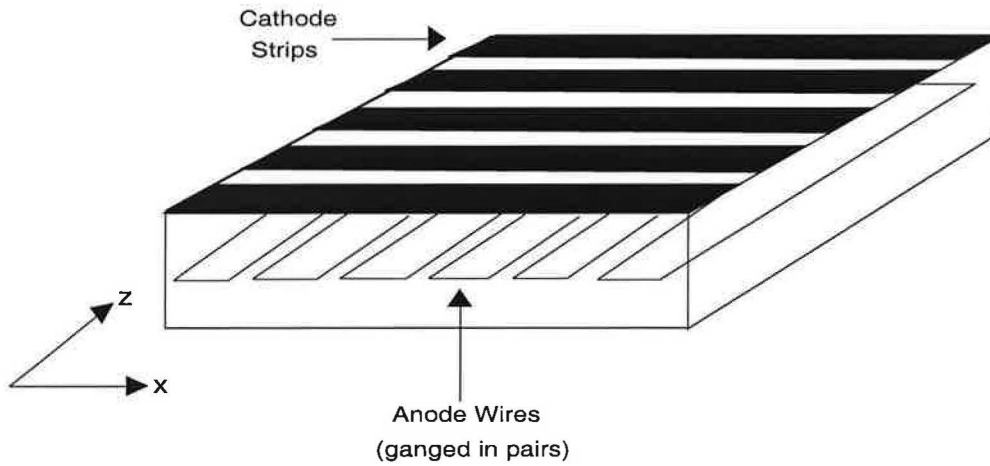


Figure 2.10: A schematic view of CES, showing the structure of strips and wires.

CHA

CHA [47] occupies most of the space in each tower, it contains 30 layers of plastic scintillators and steel plates. The total depth of CHA is about 4.5 interaction length.

2.2.3 Muon System

Since the muon mass is 200 times higher than electron mass, its bremsstrahlung radiation is about 40000 times weaker than electron. Therefore muon only deposits very small amount of energy in the calorimeter. In order to detect muons, some wire chambers are positioned outside the calorimeter system.

CMU

The central muon chamber (CMU) [48] is separated to two halves at $\theta = 90^\circ$, each half is segmented into 24 wedges. The wedge segmentation in ϕ direction is the same as the central calorimeter. Each wedge consists of 3 towers, covering 226 cm in z direction, as shown in Figure

2.11. Each tower contains 16 cells with arrangement shown in Figure 2.12 . The cross section of each cell is $6.35 \text{ cm} \times 2.68 \text{ cm}$. In the center of each cell lies a single stainless wire, and the drift time information recorded by this wire provides the $r - \phi$ position of muons while the charge division provides the $r - z$ information.

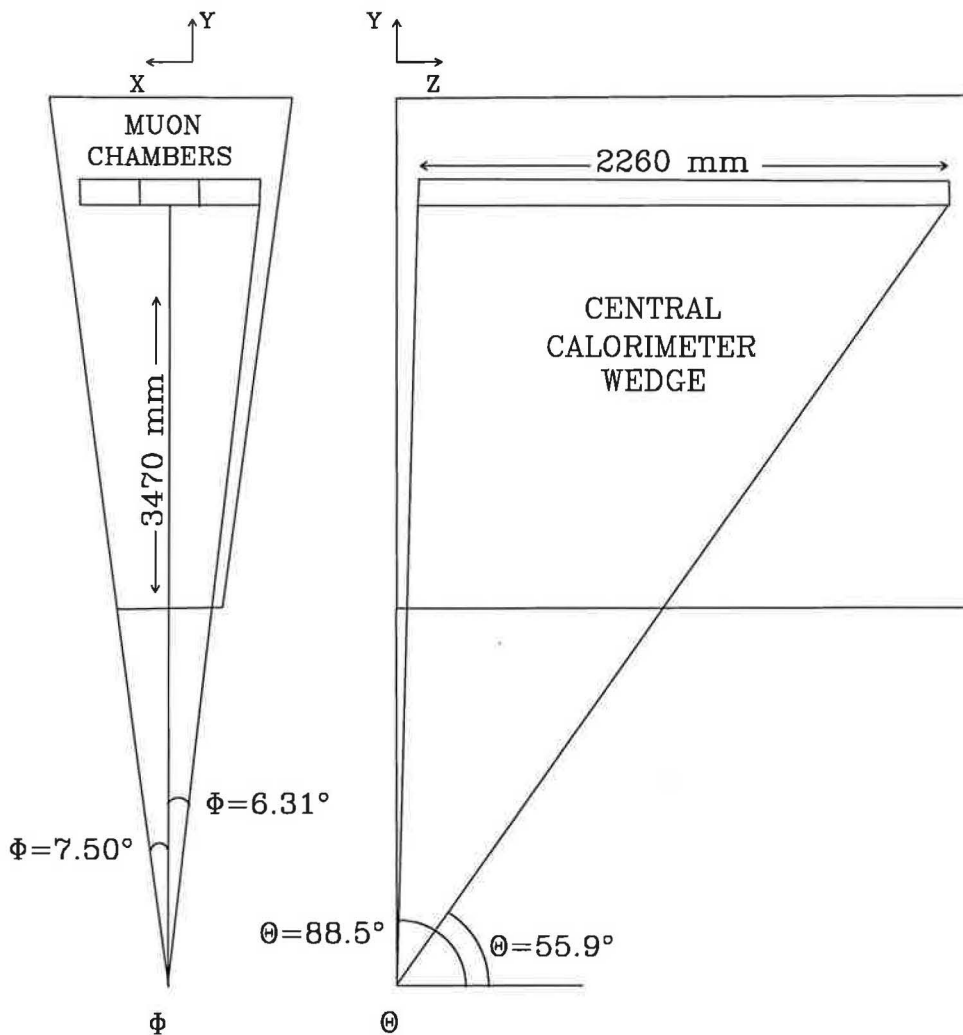


Figure 2.11: One wedge of central muon detector(CMU). Each wedge consists of 3 towers.

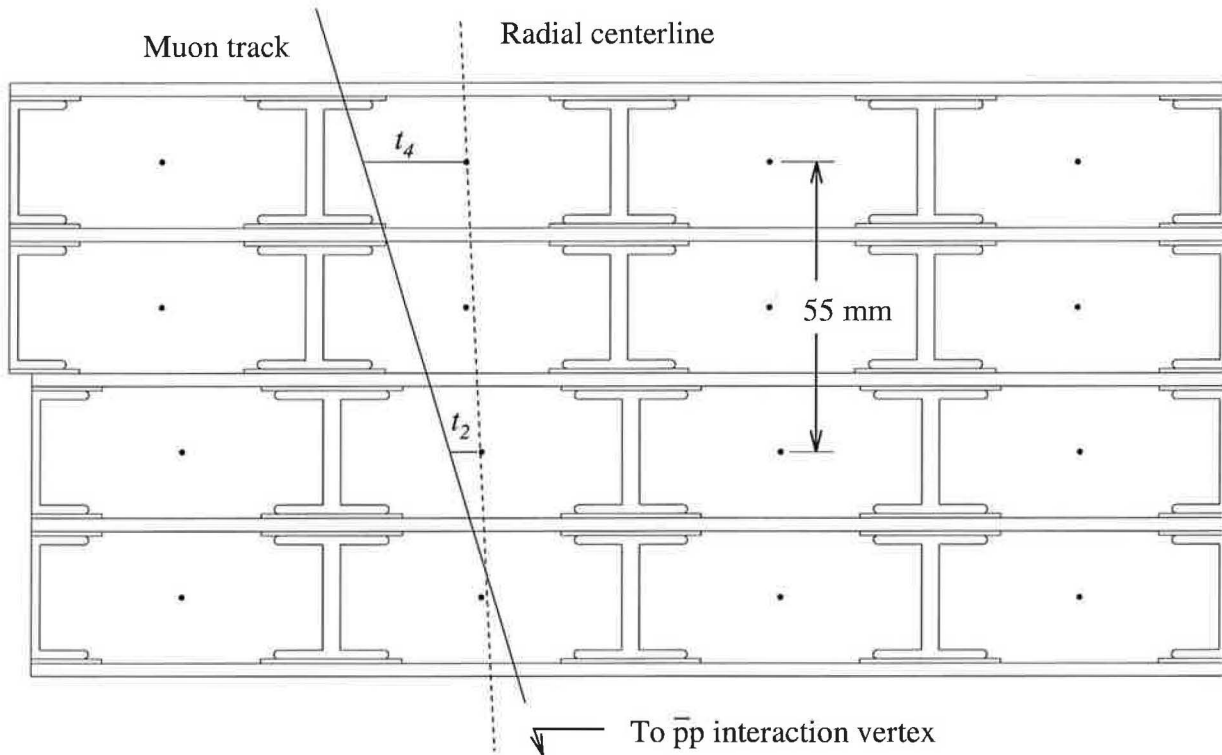


Figure 2.12: Cross section view of a CMU towers. The 4×4 arrangement of CMU cells is shown.

CMP

The central muon upgrade (CMP) chamber is located outside the magnetic field's return yoke. The muons arriving at CMP have to pass an additional steel material of 60 cm. It is equivalent to 8 interaction length, including the 4.5 interaction length in CHA. Requiring CMP stub for muon candidates can further reject the punch-through hadron background.

2.2.4 Triggering

The minimum-bias interaction cross section in $p\bar{p}$ collisions at $\sqrt{s} = 1.8$ TeV is about 50 mb ¹. With the typical Tevatron luminosity of about $10^{31} \text{ cm}^{-2}\text{s}^{-1}$, the event rate is about 300 kHz.

¹The total cross section including elastic scattering is $80.03 \pm 2.24 \text{ mb}$ [53].

The bandwidth of data to storage is limited to 5 Hz. It is difficult to collect every event for offline analysis and in fact it is not necessary. CDF used a four level trigger system to reduce the data size to a manageable level, while keeping the physically interesting events as much as possible.

Level 0 Trigger

Level 0 trigger is based on the Beam-Beam Counters(BBC) which consists of two planes of scintillator counters. BBC covers the range $3.2 < |\eta| < 5.9$ in both forward and backward directions. A coincidence of hits in both counters indicates a $p\bar{p}$ collision. This trigger can reject events from other sources like cosmic rays, and beam-gas interactions.

Level 1 Trigger

At level 1, the decision of whether or not to accept an event has to be done within $3.5 \mu\text{s}$, which is the time before the next bunch crossing occurs. Therefore, the decision has to be made based on simple measurements. The energy deposition in calorimeter and the presence of muon stub are the basis of this decision. The analog outputs of the photomultiplier tubes from two neighboring calorimeter towers are summed together. The inclusive electron trigger requires at least 8 GeV in a trigger tower (= 2 calorimeter towers). The muon trigger requires a stub with a minimum P_T . In muon system, a stub's P_T can be estimated from its angle with respect to the radial direction. Including other trigger sources, the event rate in level 1 is reduced to about 1 kHz.

Level 2 Trigger

At level 2, the available decision time is $20 \mu\text{s}$, and more sophisticated methods can be employed for further decision making. In Run 1, CDF used a hardware track processor, central fast tracker(CFT), to calculate track's P_T based on the hits pattern from the 5 axial superlayers in CTC. With the special geometry design of 45° tilt angle, a track entering CTC is ensured to have a near hit in axial superlayer. The hits recorded by CTC sense wires within 80 ns after beam crossing is called prompt hits, the hits recorded 500-650 ns later is called delayed hits. CFT used a hardware look-up table to recognize the pattern of prompt hits and delayed hits associated with a track in each axial superlayer to reconstruct particle trajectory. The P_T resolution of CFT is $\delta P_T/P_T \sim 0.035$.

In the calorimeter, a triggering tower with sufficient energy makes a *seed* tower. The electromagnetic energy in the seed tower and in the neighboring towers are added together to form an electromagnetic cluster. An electromagnetic cluster with $E_T > 5 \text{ GeV}$ is linked with a CFT track to form an electron candidate. The muon stub is also linked to a CFT track to form a muon candidate. Overall, the level 2 selection requirements reduce the event rate to 12 Hz.

Level 3 Trigger

In Run 1, level 3 trigger is a software system, event selection using 64 commercial computers. The events passing level 2 are processed with the almost identical software filter as offline analysis programs. The major CPU-consuming task is the reconstruction of 3-D tracks. The energy cluster and muon stub are linked to CTC tracks. At this final stage, the event rate is reduced to 5 Hz.

Chapter 3

Event Selection and Reconstruction

The $b\bar{b}$ production cross section in $p\bar{p}$ collision at $\sqrt{s} = 1.8$ TeV is about $50 \mu\text{b}$, which is quite large compared to 1 nb in e^+e^- collision at $\Upsilon(4S)$ and 6 nb at Z pole [50]. With a total integrated luminosity of 110 pb^{-1} , about 5.5×10^9 $b\bar{b}$ events were produced in Tevatron during Run 1. Compared with other experiments, the large number of $b\bar{b}$ events is an advantage for B physics study with the Tevatron collider. However, the total cross section is about 80 mb at Tevatron, about 3 orders of magnitude higher than the $b\bar{b}$ production cross section. To distinguish B events from the overwhelming background is a big challenge.

In CDF the B events are selected by detecting their associated J/ψ and semileptonic decays. $B \rightarrow J/\psi X$ events and B semileptonic decay events are collected using the dimuon trigger and the inclusive lepton trigger respectively. The J/ψ particles are very easy to be identified due to their strong invariant mass peak of $3.1 \text{ GeV}/c^2$. In the candidate events of $B \rightarrow J/\psi X$, all the charged daughter tracks in the B decay are detectable. The mass and lifetime measurements of B hadrons through the channels $B_u \rightarrow J/\psi K$, $B_d \rightarrow J/\psi K_s$, $B_s \rightarrow J/\psi \phi$, $\Lambda_b \rightarrow J/\psi \Lambda$ have been reported in CDF. Unlike the J/ψ decay mode, the B semileptonic decay is not fully reconstructed since the neutrino accompanying the lepton is not detectable. But the large branching ratio of B semileptonic decay ($\sim 10\%$ for all B hadrons for each e and μ decay)

makes this channel attractive. Since the single lepton sample is not as pure as J/ψ sample, it is necessary to apply tighter lepton identification cuts to improve the purity of lepton sample in the offline analysis stage. However, even in a high purity lepton sample, there is no guarantee that all of them are from B decays. The contributions from W and Z decays, charm decays and photon conversion to e^+e^- pairs are the possible background sources.

The other important product in the B semileptonic decay is the charm hadrons. At Tevatron energy, the B hadron usually is boosted by a $\beta\gamma$ factor of $2 \sim 4$, therefore in its semileptonic decay mode the charm hadron daughter usually appears in the vicinity of the lepton track. The combination of a charm meson and a proper charge correlation with a high $P_T(> 6 \text{ GeV}/c)$ lepton is the signal of a B semileptonic decay that we search for. In this analysis, we are looking for the decay sequence $\Lambda_b \rightarrow \Lambda_c^+ e^- \nu_e$, where $\Lambda_c \rightarrow \Lambda \pi^+ \pi^+ \pi^-$, and $\Lambda \rightarrow p \pi^-$ and its charge conjugate decay. We describe the track quality and the primary vertex requirements in section 3.1, and the electron identification cuts in section 3.2. The generation of Monte Carlo sample is described in section 3.3. The event reconstruction method consists of two major steps: to select $e\Lambda$ sample at the first and then to reconstruct the signal of $\Lambda_c^+ \rightarrow \Lambda \pi^+ \pi^+ \pi^-$. They are discussed in section 3.4 and 3.5 respectively. The backgrounds are discussed in section 3.6.

3.1 Event Reconstruction

During the on-line data taking stage, the events were recorded in the form of hits or pulse heights for various tracking chambers and in the form of energy clusters for various calorimeters. The recorded events are therefore called "raw data". Before physics results can be analyzed and extracted, these raw data have to be processed and turned into the fundamental physical objects like particle tracks, electron and muon candidates, jets and photons. Among the various steps

in the event reconstruction process, we will introduce the methods for track and primary vertex reconstruction in the following sections.

3.1.1 Track Reconstruction

In the track reconstruction procedure, the hits in each CTC layer are linked together to form helical curves with 5 tracking parameters. The first step is to search for track segments or stubs inside each axial superlayer. It takes at least 3 hits in a row to form an axial layer stub. These stubs are then linked together to form CTC tracks. Since the hit density is lower at the outer layer, the linking procedure started from the outer layer. The remaining hits in each axial and stereo superlayer within a road size ¹ of a CTC track will be added to that track, and the associated tracking parameters and the error covariance matrix are updated accordingly. A track with hits from axial and stereo superlayers is called a 3-D track. If only axial hits are found, it's a 2-D track. For a better track quality, in this analysis we select 3-D tracks only and require that the tracks should have at least 2 axial superlayers (out of 5) and at least 2 stereo superlayers (out of 4). We also require at least 5 hits (out of 12) fired for an axial superlayer and at least 2 hits (out of 6) fired for a stereo superlayer. To make sure that the reconstructed tracks travel through all the layers in CTC, we require the radius where the tracks exit the CTC volume to be larger than 130 cm, which is the radius of the outermost layer. Under the influence of the 1.4 T magnetic field, this requirement implies a P_T minimum cut at 0.25 GeV/c. Those tracks with $P_T < 0.25$ GeV/c will just loop around inside the CTC inner layers and won't provide any useful information. In CDF usually only the tracks with $P_T > 0.4$ GeV/c are used in analyses, because we have a better understanding of the tracks in this range.

The hit resolution in SVX detector is much better than CTC. But because there are only

¹The CTC hit resolution is about 200 μm . The road size is usually chosen to be a few times of this resolution.

4 layers of SVX microstrip detectors, it is not sufficient for a stand-alone tracking. Instead, the SVX hits are used based on the matching CTC tracks. Each CTC track is extrapolated to the surface of the outermost layer of SVX to search for the SVX hits within a road size of 4σ of the tracking resolution. When a hit candidate is added to the CTC track, the tracking parameters are updated. This updated fitting procedure is repeated for the remaining inner layers. In general, a SVX track should have at least 2 hits. In this analysis, in order to have a stable vertex quality, we require each track to have at least 3 SVX hits.

3.1.2 Primary Vertex and Beam Position

In Tevatron Run I, more than one $p\bar{p}$ collisions could occur in each bunch crossing. Only one of them is the event which activates the trigger system, the remaining events, usually known as pile-up events, are from minimum bias interaction. These pile-up events and the triggered event are recorded in the same event, and therefore contribute additional tracks and extra primary vertices. The list of primary vertices determined by the VTX detector is available in offline stage. Each primary vertex candidate is assigned a class number according to the number of associated VTX tracks. The one with more VTX tracks is classified with higher number. The highest class is 12.

The average beam position varies from run to run, but they remain stable within each run. In this analysis, the beam position is taken from the run average. The beams are also not exactly on the detector axis. For the primary vertex candidates provided by VTX, each of them has different position in transverse plane. In a B event, the primary vertex is selected as the one closest to the trigger lepton, trigger dimuon or the secondary vertex.

3.2 Electron Identification

3.2.1 Longitudinal and Transverse Shower Sharing

The calorimeter system in CDF covers the η range from -4.2 to 4.2. The electromagnetic shower generated by the electrons can be detected in CEM, PEM and FEM. But the tracking system only covers the central range ($|\eta| < 1.1$), therefore we select the central electrons only to have better tracking measurements.

In the central region, the electrons traverse CEM and deposit most of their energy, only a small fraction would leak into CHA. On the other hand, hadrons go deeper and deposit most of their energy in CHA, as we mentioned in section 2.2.2. We use the ratio of E_{CHA}/E_{CEM} to distinguish electrons from hadrons, where E_{CEM} and E_{CHA} are the electron candidate's energy deposition in CEM and CHA respectively. We require this ratio to be $E_{CHA}/E_{CEM} < 0.04$ for electrons. Figure 3.1 shows its distribution. In some instances there are more than one 3-D tracks associated with an electromagnetic energy cluster due to the presence of extra hadrons and leads to a higher E_{CHA}/E_{CEM} ratio. For such a case we require $E_{CHA}/E_{CEM} < 0.10$. The multiplicity of 3-D tracks is shown in Figure 3.2(a). An electron surrounded by hadrons would tend to have higher E_{CHA}/E_{CEM} ratio and is more likely to be rejected. Therefore this energy ratio cut also implies an isolation requirement.

The E_{CHA}/E_{CEM} cut takes advantage of different longitudinal shower profiles of electrons and hadrons. The behavior of transverse shower profile is also useful as well for electron identification. In general, hadronic showers have larger sizes and usually will span across several calorimeter towers. Because electromagnetic showers generated by electrons usually are only a few centimeters in diameter, most of the time they are contained in a single calorimeter tower. The energy sharing occurs when a electron enters the boundary of two adjacent towers

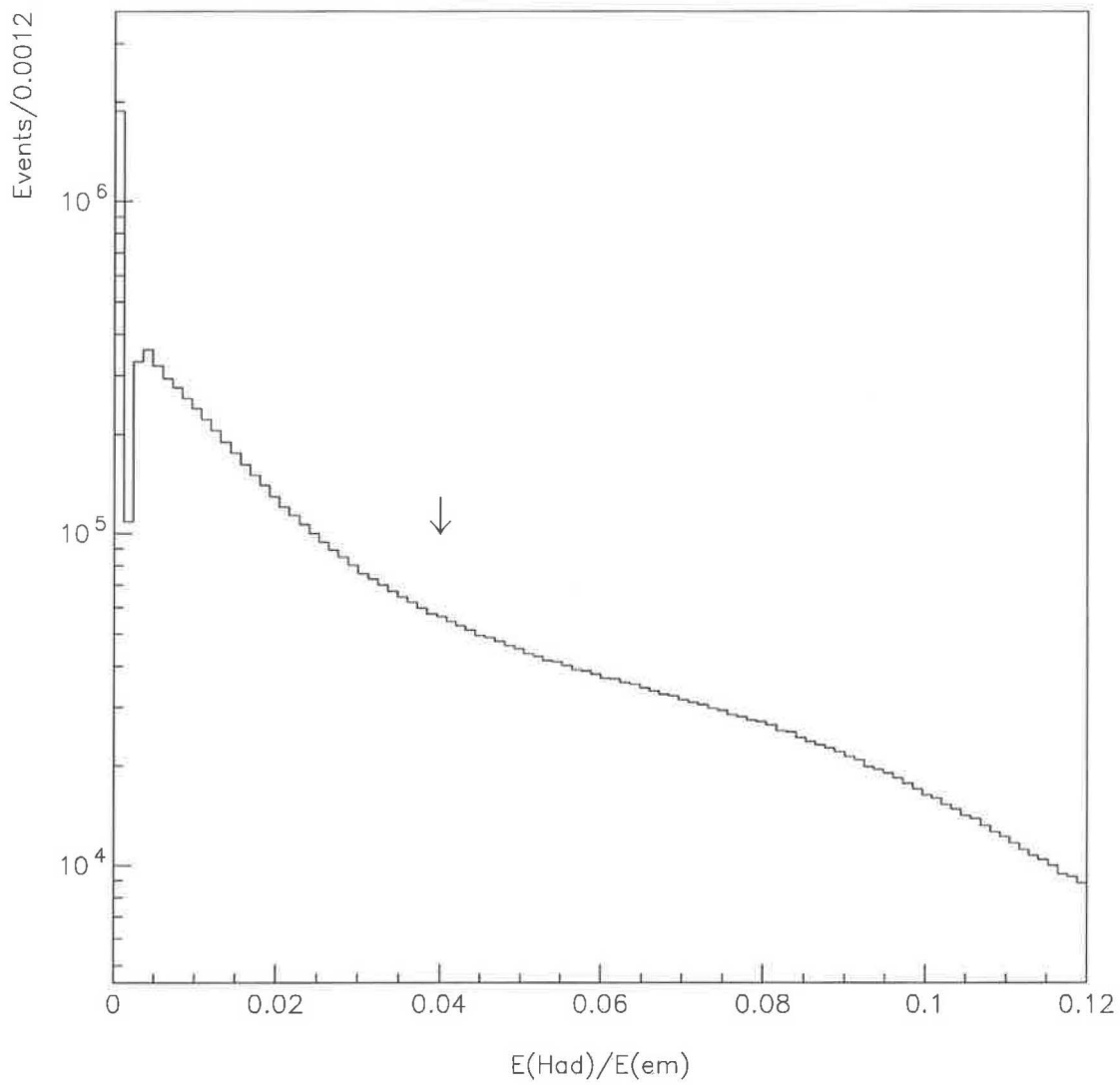


Figure 3.1: The ratio of energy deposition in CHA and CEM for Run 1 inclusive electron data. The spike near zero is contributed from those electrons which were absorbed completely in CEM.

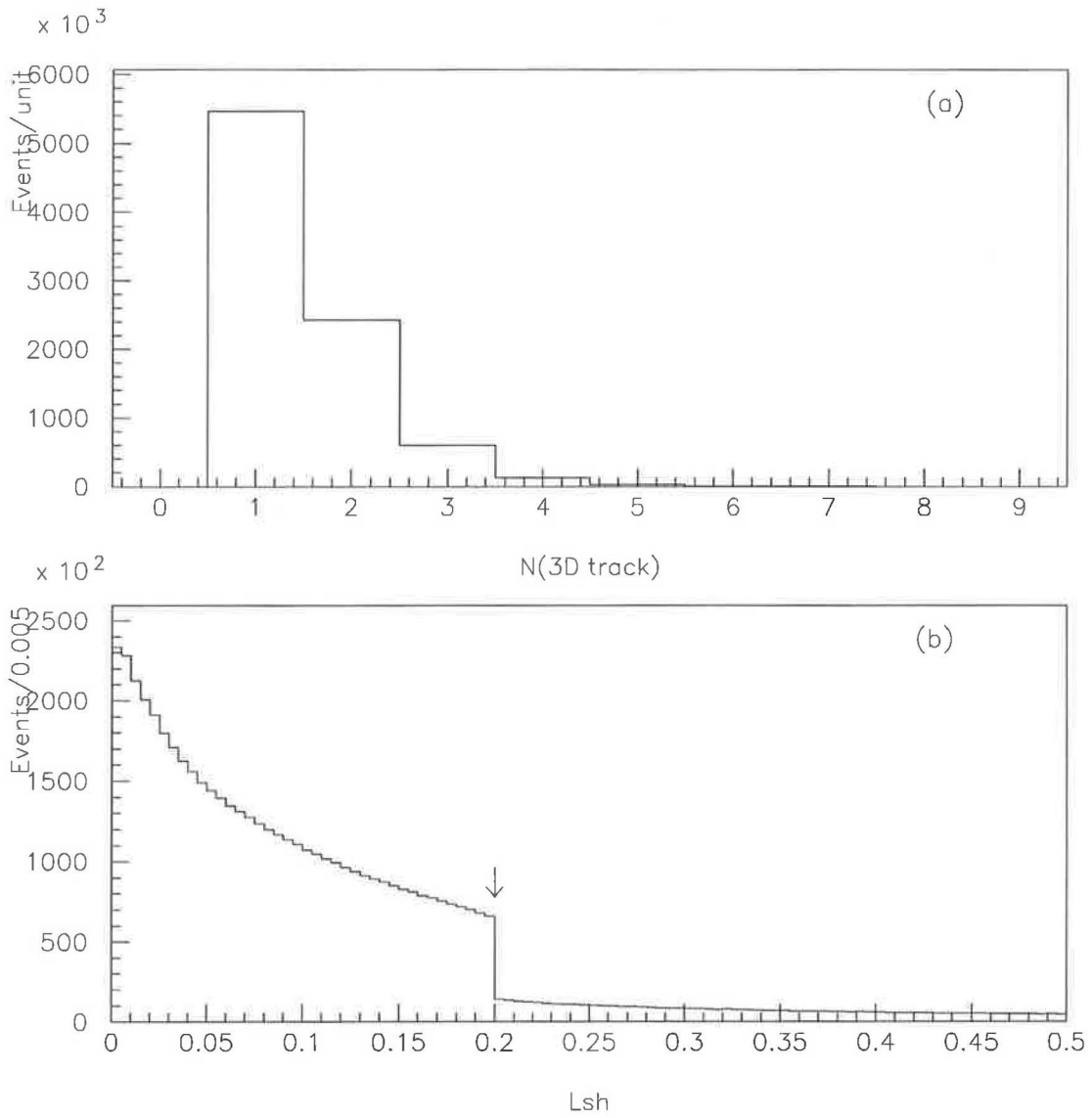


Figure 3.2: The multiplicity of 3-D tracks associated to electromagnetic cluster(a), and the lateral shower profile for three-tower case (b). The drop at 0.2 is due to the requirement of $L_{shr} < 0.2$ at level 3 electron trigger for two-tower cae.

in η direction. In CDF the energy sharing is examined in two-tower case and three-tower case. It is expressed as a χ^2 -like variable $L_{shr,n}$ defined as follows.

$$L_{shr,n} = 0.14 \sum_{k=1}^{n-1} \frac{M_k - P_k}{\sqrt{0.14^2 E_T + (\Delta P_k)^2}} \quad (3.1)$$

The summation is over the $n - 1$ adjacent towers, where n denotes the two-tower or three-tower case. M_k is the measured energy in tower k , P_k is the energy prediction based on the z measurement in CES, $0.14\sqrt{E_T}$ is the energy resolution of CEM, and ΔP_k is the estimated uncertainty of P_k . The electron trigger at level 3 requires $L_{shr,2} < 0.2$. In this analysis we further require $L_{shr,3} < 0.2$ according to the test beam result with 50 GeV/c electrons [54].

3.2.2 Shower Profile in $r - \phi$ View and z View

The transverse shower profile at the shower maximum is measured by the strips in z view and wires in $r - \phi$ view in CES chamber. The measured strip and wire pulse heights should be consistent with the test beam measurements. In both $r - \phi$ and z view, the goodness of the shower profile match is characterized by the χ^2 :

$$\chi^2 = \frac{1}{4} \sum_{i=1}^{11} \frac{(q_i^{obs} - q_i^{pred})^2}{\sigma_{qi}^2} \quad (3.2)$$

Where q_i^{obs} is the measured pulse height for each wire or strip, and σ_{qi} is the uncertainty. The q_i^{pred} is the predicted value determined from the test beam result. Level 3 trigger requires $\chi_{strip}^2 < 10$ in Run 1A and 1B, and requires $\chi_{wire}^2 < 15$ in Run 1A and $\chi_{wire}^2 < 10$ in Run 1B. We require $\chi_{wire}^2 < 10$ in this analysis. Their distributions are shown in Figure 3.3.

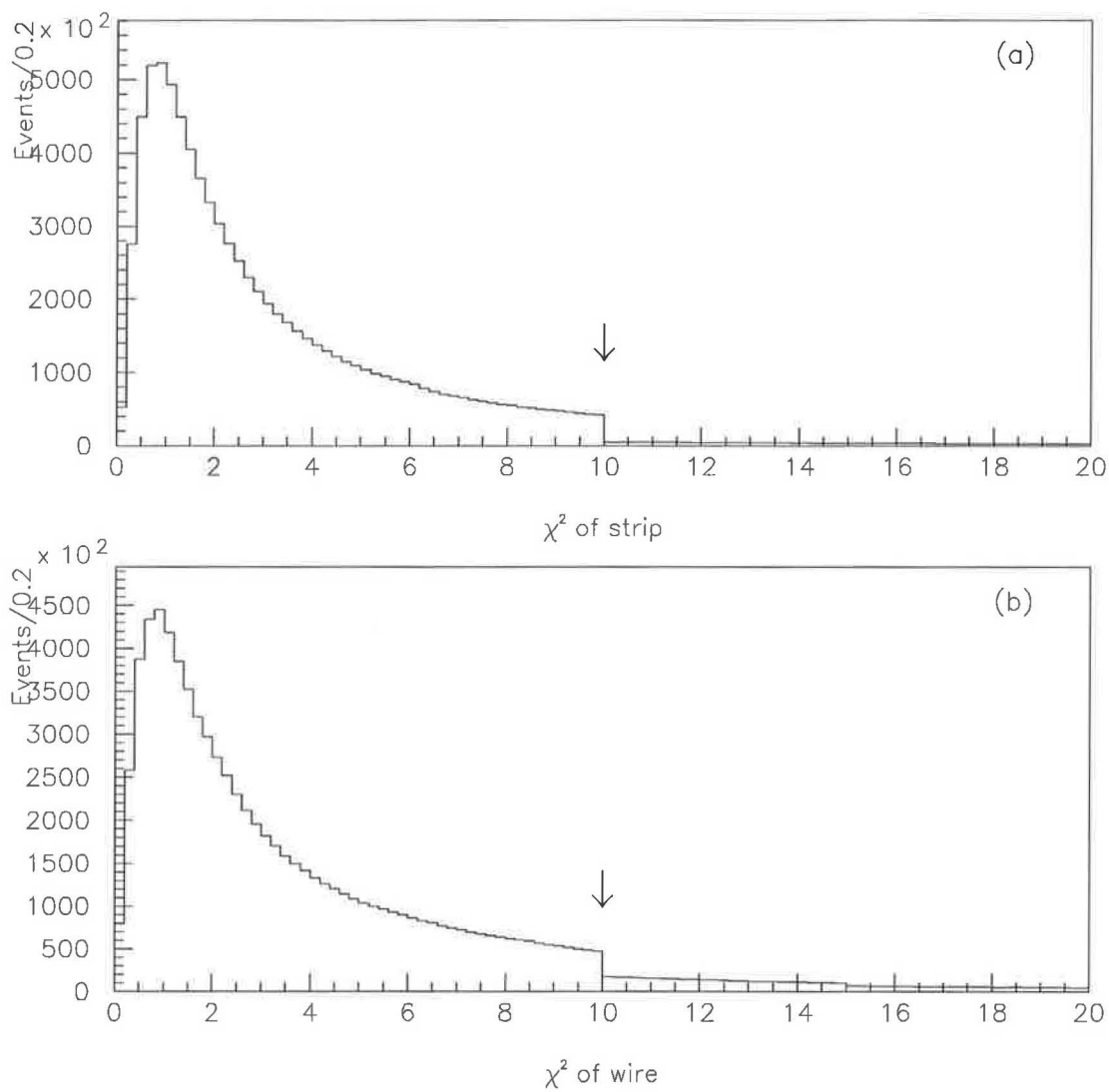


Figure 3.3: The χ^2 of transverse profile match with test beam results, for z view strips and $r - \phi$ view wires in CES. The drops at $\chi^2 = 10$ for plot (a) and (b) are the results of level 3 electron trigger requirements for Run 1 data.

3.2.3 Match between CTC Track and Energy Cluster

An electron can be identified as a track in CTC, an energy cluster in CEM, and strip and wire cluster in CES. All these position information have to be consistent. To check the consistency, the CTC track is extrapolated to the CES plane; and the x and z coordinates of the intersection points are denoted as X_{CTC} and Z_{CTC} . In the calorimeter tower containing the CEM cluster, the CES strip cluster with the largest deposited energy is selected as the best strip cluster to provide electron candidate's z position, denoted as Z_{strip} . The best wire cluster is defined as the cluster closest to X_{CTC} in $r - \phi$ plane, and used to provide the electron candidate's x position, denoted as X_{wire} . We require $|Z_{strip} - Z_{CTC}| < 3$ cm and $|X_{wire} - X_{CTC}| < 2$ cm. Figure 3.4 shows these distributions.

The momentum and energy of an electron candidate are measured independently by CTC tracking chamber and CEM calorimeter, respectively. They have to be consistent with each other. Since an electron must have at least 6 GeV/c in P_T to pass the trigger requirement, the electron mass is negligible. The electron's measured energy and momentum should be comparable. The distribution of this E/P ratio is shown in Figure 3.5. In this analysis we require $0.75 < E/P < 1.5$.

3.2.4 Non-B Electron Removal

An electron candidate passing all the above requirements is identified as a good quality electron. For B hadrons analysis we must select electrons from B decays. We will briefly describe how we remove the electrons from the non-B sources such as the photon conversion processes and the W, Z decays.

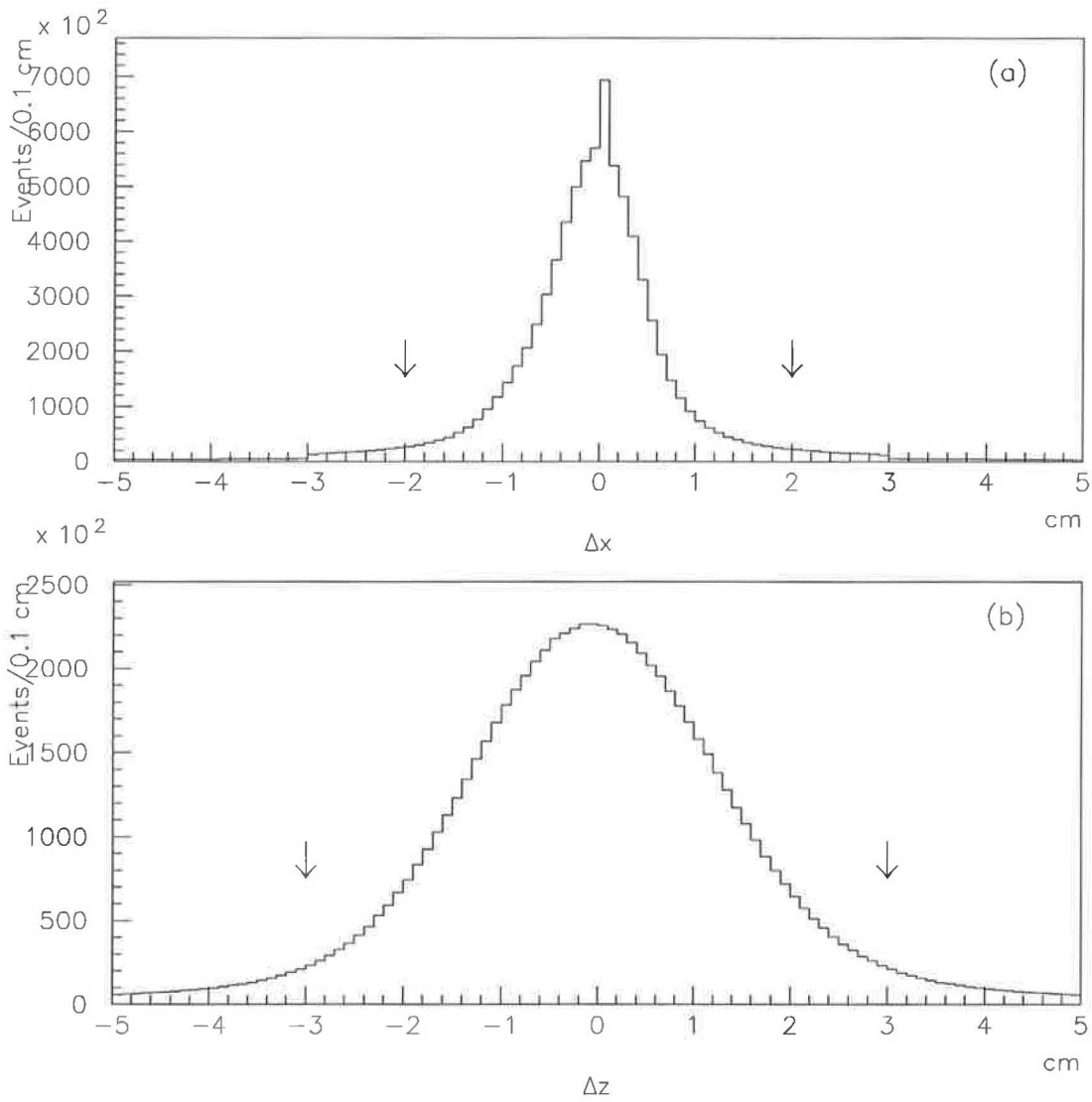


Figure 3.4: The x position difference between CTC track and CES wire cluster (a), and z position difference between CTC track and CES strip cluster (b) for Run 1 data.

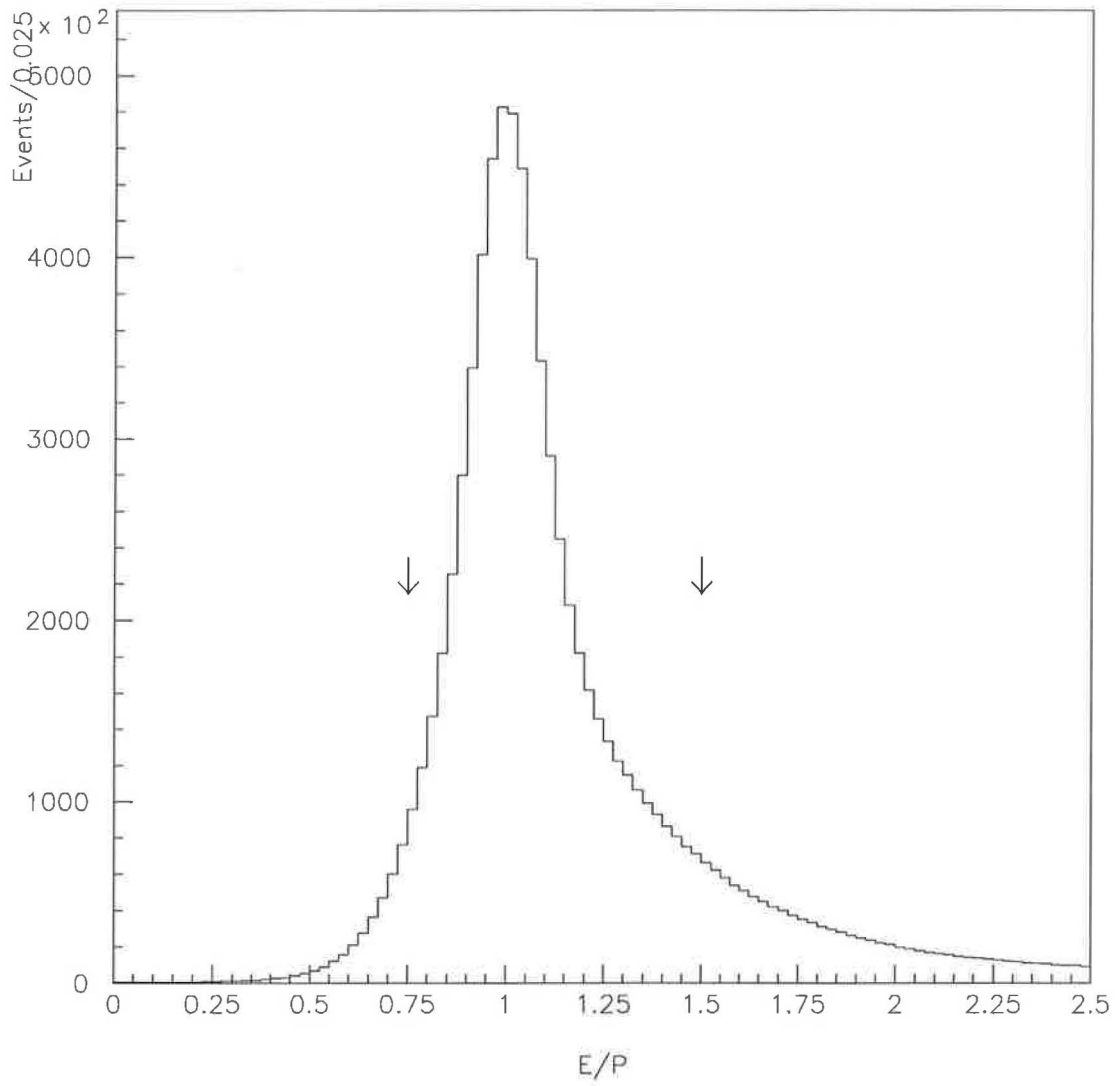


Figure 3.5: The ratio of energy deposited in CEM calorimeter and momentum measured by CTC tracking chamber for electron candidates in Run 1 data.

Photon Conversion Electron

An early study at CDF [55] showed that photon conversion electrons could comprise about 30 % of the good electron sample. Photon conversion produce e^+e^- pairs. To reject this background, we look for the events having a partner track associated with the good quality electron with opposite charge. Their opening angle, θ_c , should be small. We required $\Delta \cot \theta_c < 0.06$. Both the electron and its partner have a circular curve track on the transverse plane. The separation S at the closest points of these two circles is required to be smaller than 0.2 cm.

W, Z Decay Electron

The electrons coming from the decay of $Z \rightarrow e^+e^-$ can be identified through the invariant mass spectrum of e^+e^- pairs. Both electrons are expected to pass the electron ID cuts we have mentioned so far. However, in order to reject the Z background as much as possible, one of the electrons is applied with loose cuts in which a calorimeter energy cluster with more than 90% of electromagnetic (EM) energy is required. An electron candidate would be rejected if the invariant mass of the electron and a high EM fraction cluster is greater than $75 \text{ GeV}/c^2$.

The neutrino from the decay $W^- \rightarrow e^- \bar{\nu}_e$ is not detectable in the CDF detector, its energy is determined from the imbalance of the vector sum of transverse energy(E_T) over all the calorimeter towers. This imbalance is called missing transverse energy, and is defined by $\cancel{E}_T = | \vec{E}_{Ti} |$, where \vec{E}_{Ti} is a vector with the magnitude of transverse energy for calorimeter tower i and the direction from interaction point to calorimeter tower i . An event with electron E_T exceeding 25 GeV and \cancel{E}_T greater than 20 GeV in the opposite direction is identified as W event and is rejected.

Table 3.1 is the summary of the electron ID cuts.

electron cut	
N(3D track)	≥ 1
region	central
E_{CHA}/E_{CEM} (N(3D track) = 1)	< 0.04
E_{CHA}/E_{CEM} (N(3D track) > 1)	< 0.10
Transverse profile in CEM	< 0.2
χ^2 of strip profile	< 10
χ^2 of wire profile	< 10
$ \Delta x $ between CES and CTC	< 2.0 cm
$ \Delta z $ between CES and CTC	< 3.0 cm
P_T	> 6 GeV/c
E / P	> 0.75 , < 1.5
Photon conversion	$ S < 0.2$ cm
	$\Delta \cot \theta_c < 0.06$
Z removal	$M(e, \text{EM-cluster}) > 75$ GeV/c ²
W removal	$E_T(e) > 25$ GeV
	$\cancel{E}_T > 20$ GeV

Table 3.1: Summary of electron identification cuts.

3.3 Monte Carlo Generation

3.3.1 Generation of b Quarks and Λ_b Hadrons

In this analysis, we use BGENERATOR [56] to produce Λ_b Monte Carlo samples to model the signal. In BGENERATOR, only B hadrons events are produced; the underlying events and pile-up events are not taken into account. The b quarks are generated according to a next-to-leading-order calculation of $d^2\sigma/dy dP_t$ spectrum by Nason, Dawson and Ellis [26]. The MRSD0 parton distribution function [23] is used. The b quark mass is set to $4.75 \text{ GeV}/c^2$. The generated b quarks are then hadronized to Λ_b with the Peterson function of $\epsilon_b = 0.006$ [27]. The generating conditions for b quark are listed in Table 3.2. The spectrum of b quark P_T and electron P_T are shown in Figure 3.6.

$$\begin{array}{c} \hline \hline P_T(\text{b quark}) > 8 \text{ GeV}/c \\ |y(\text{b quark})| < 2.0 \\ M(\Lambda_b) = 5.641 \text{ GeV}/c^2 \\ \hline \hline \end{array}$$

Table 3.2: Generation conditions for Λ_b Monte Carlo sample in BGENERATOR.

3.3.2 Decay of the Λ_b Hadron

The decay of $\Lambda_b \rightarrow \Lambda_c^+ e^- \bar{\nu}_e$ and $\Lambda_c^+ \rightarrow \Lambda \pi^+ \pi^+ \pi^-$ are simulated in a separated package QQ developed by CLEO [58]. The advantage to use QQ is the up-to-date B decay branching ratios. The decay of the long-lived particle Λ is simulated in the detector simulation package.

3.3.3 Detector Simulation

The detector simulation is done by a CDF's package QFL' [59]. The output has the same format as real data for the consistency and convenience in analysis. CTC hits are not generated in

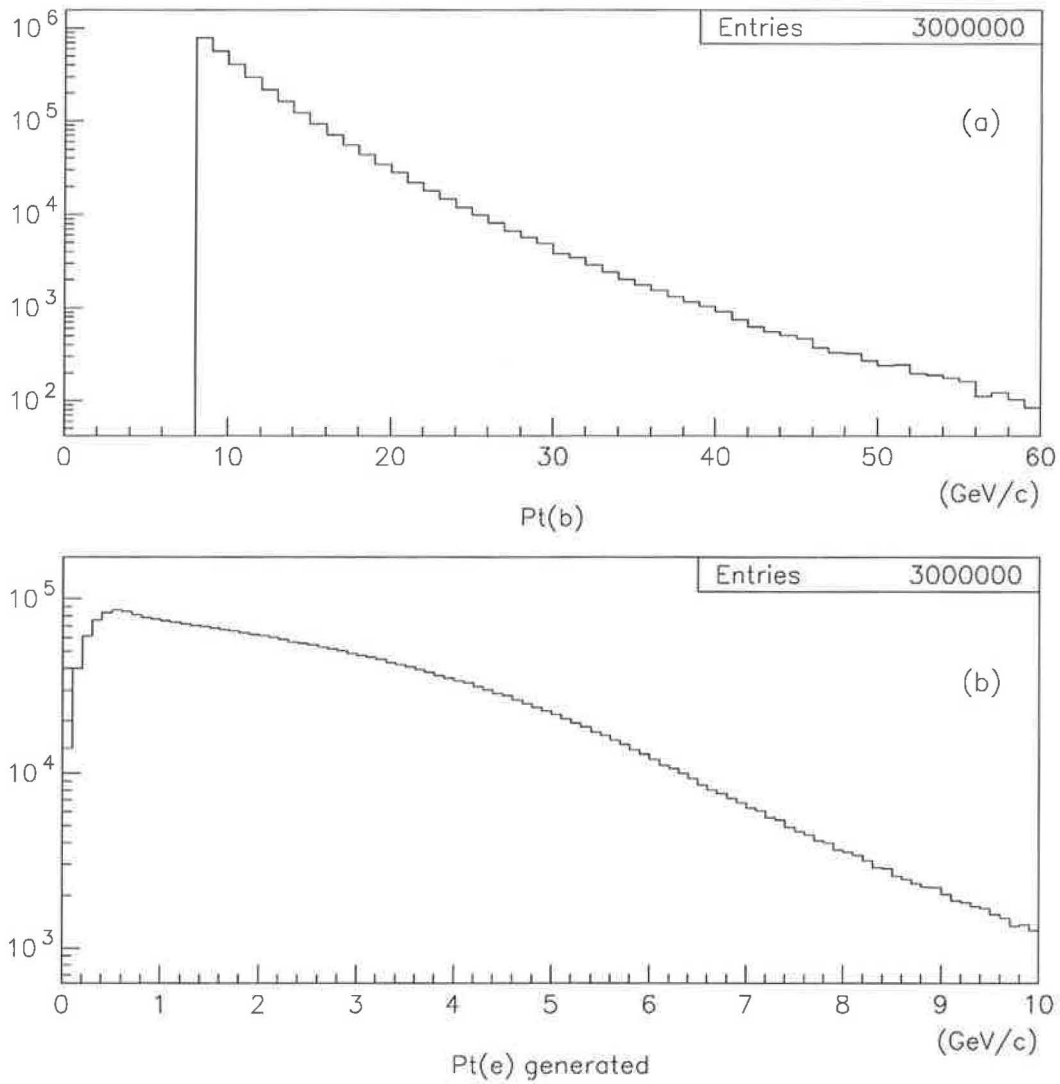


Figure 3.6: (a) P_T spectrum of b quark, and (b) P_T spectrum of the semileptonic electron from BGENERATOR.

$$\begin{array}{c} \hline \hline P_T(e) > 6.0 \text{ GeV}/c \\ |\eta(e)| < 1.1 \\ \hline \hline \text{level 2 trigger modeling} \end{array}$$

Table 3.3: Requirements for the Monte Carlo data reduction prior to detector simulation.

QFL'. The CTC tracks are obtained from a parameterization procedure based on the tracks generated from BGENERATOR and QQ according to the detector performances. Since we are interested in the behavior of secondary vertices, the SVX hits are generated and linked to form SVX tracks.

Although we set the b quark minimum P_T at 8 GeV/c, only a small fraction of electrons from B decay pass the trigger requirement. To save CPU time, prior to the detector simulation we reject the Monte Carlo events in which the electrons are too soft or out of the detector's acceptance based on the result from generator. The requirements are listed in Table 3.3.

In order to have a correct electron P_T spectrum in Monte Carlo data, the Level 2 electron trigger efficiency has to be taken into account. We used a simple function to parameterize this L2 efficiency, as shown in equation (3.3),

$$L2 = 0.927 \cdot \text{Freq}\left(\frac{P_T - 6.18}{4.20}\right) \cdot \text{Freq}\left(\frac{P_T - 7.48}{0.504}\right) \quad (3.3)$$

where $\text{Freq}(x)$ is an error function defined as

$$\text{Freq}(x) = \frac{1}{\sqrt{2\pi}} \int_{-\infty}^x e^{-\frac{1}{2}t^2} dt \quad (3.4)$$

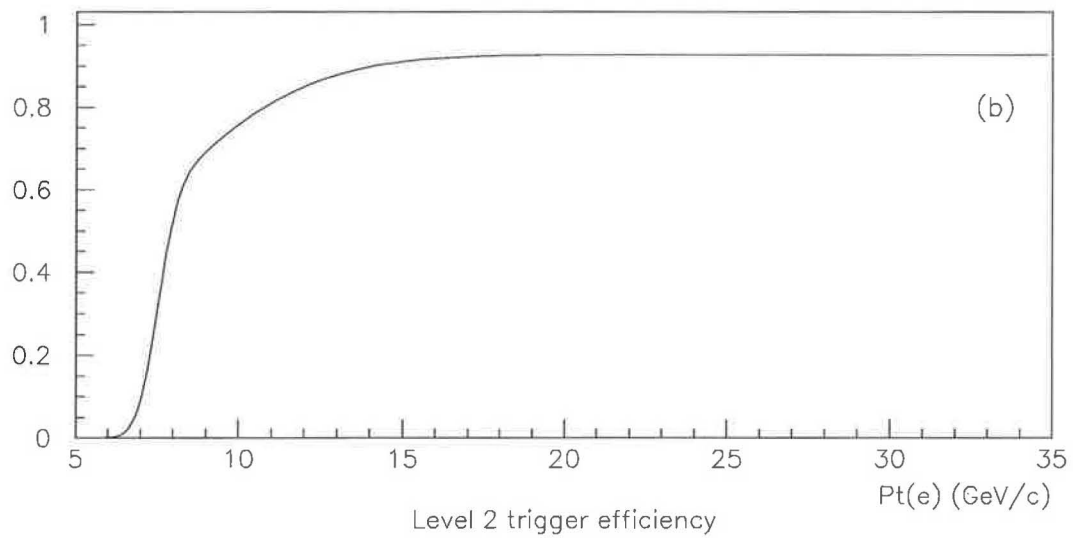
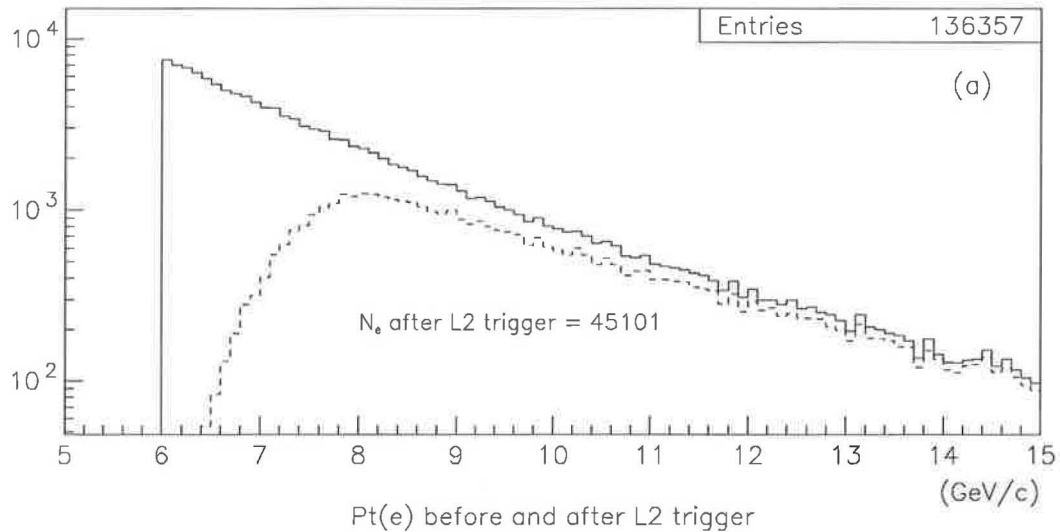


Figure 3.7: (a) Electron P_T spectrum before (solid line) and after (dash line) level 2 trigger simulation. The level 2 trigger efficiency is plotted in (b)

Figure 3.7 shows the electron P_T spectrum before and after this level 2 efficiency simulation. The function plot of the level 2 efficiency used in equation (3.3) is also shown in the same Figure for comparison.

3.4 $e\Lambda$ Sample Selection

In the decay $\Lambda_b \rightarrow \Lambda_c^+ e^- \bar{\nu}_e$ the charm baryon Λ_c is very close to the electron. We can define the distance between the electron and Λ_c in $\eta - \phi$ space as

$$\Delta R(\ell\Lambda_c) = \sqrt{(\eta(\ell) - \eta(\Lambda_c))^2 + (\phi(\ell) - \phi(\Lambda_c))^2} \quad (3.5)$$

ΔR is also known as the cone size. From the Monte Carlo sample we can see that most of the time the cone size $R(e\Lambda_c)$ is smaller than 1. The daughter tracks of Λ_c therefore are also contained within this cone. The Monte Carlo results of these cone sizes are shown in Figure 3.8.

To reconstruct the $\Lambda_c \rightarrow \Lambda 3\pi$ events, we first attempt to find the Λ around the electron. We look for two opposite charge tracks in the cone $\Delta R < 1$. The track with higher P_T is assigned as p candidate and the track with smaller P_T is assigned as π candidate. This condition is always true based on the kinematics of two body decay.

These two tracks are then required to form a vertex. The outermost layer of the SVX detector is at $R = 8$ cm. The long-lived Λ has a large probability to decay outside of the SVX detector volume and leave the decay vertex inside CTC. Our strategy is to use two CTC tracks to form a vertex at the beginning. If the vertex is inside $R = 5.6$ cm, then an attempt is made to find the associated SVX tracks and fit the vertex again. The radius of $R = 5.6$ cm is the

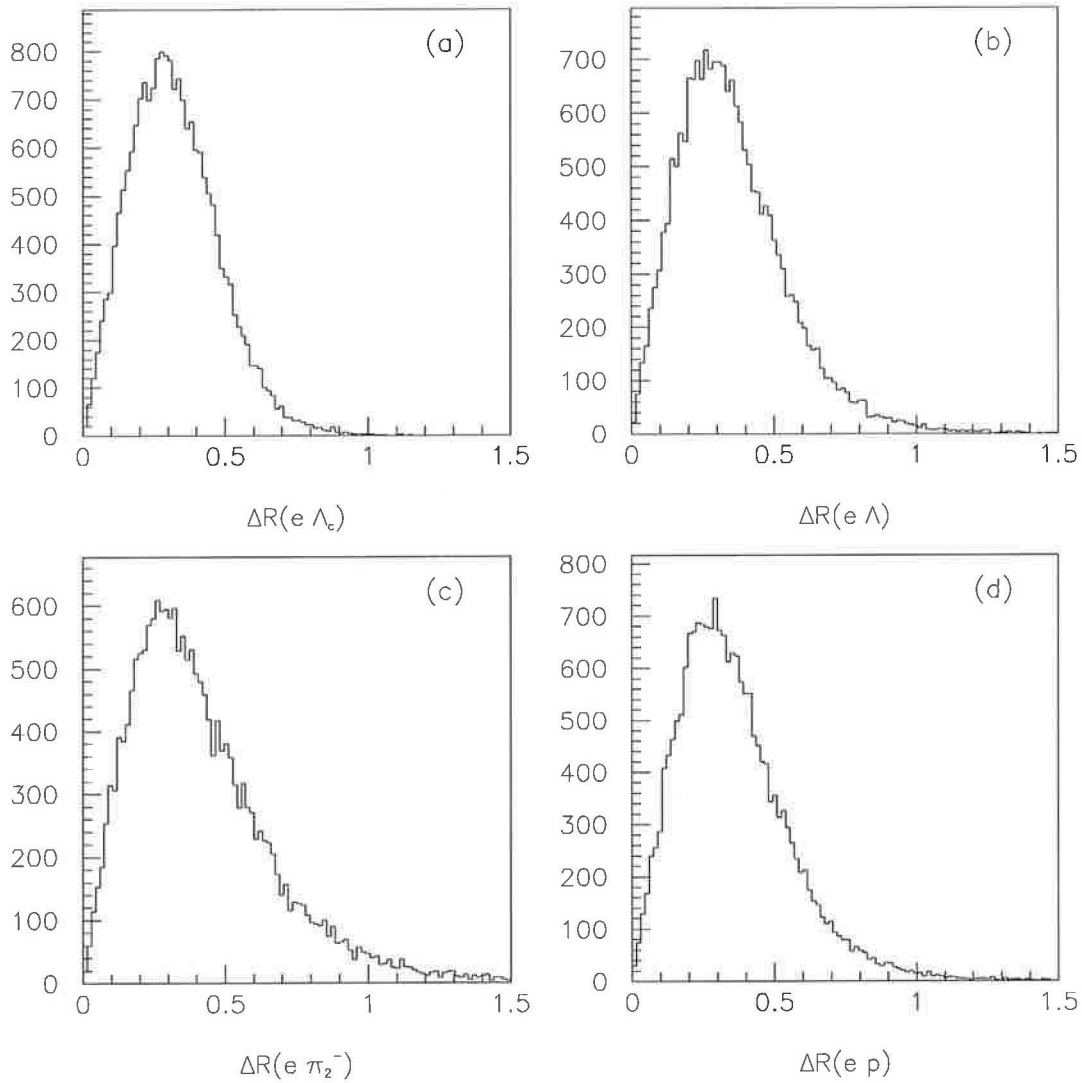


Figure 3.8: Cone size between daughter tracks of Λ and electron . (a) $\Delta R(e\Lambda_c)$, (b) $\Delta R(e\Lambda)$, (c) $\Delta R(e\pi_2^-)$ and (d) $\Delta R(ep)$, π_2 and p are daughter tracks of Λ .

place between the layer 1 and 2 (counting from 0 to 3) of the SVX detector. In this way we can ensure that once SVX tracks are used for the daughter particles of Λ , they each have at least 2 SVX hits. In the following we denote these two cases as Λ_{CTC} and Λ_{SVX} . We require the χ^2 probability of the vertex fitting to be larger than 1 %. This cut is commonly used in CDF for the two-track vertices.

A large fraction of the background is from the random combination of prompt tracks which come from the primary vertex. We cut on $L_{xy}(\Lambda) > 1\sigma$ to reject these background, where $L_{xy}(\Lambda)$ is the transverse projection of the distance between the Λ vertex and the primary vertex, and σ is its uncertainty. In $p\bar{p}$ collisions there are many sources of Λ production, but we are only interested in those coming from the Λ_b decay. The constraint on the invariant mass of the electron and Λ provides another cut. We require $M(e\Lambda) < 4.5 \text{ GeV}/c^2$. The comparison of $M(e\Lambda)$ between real data and Monte Carlo is in Figure 3.9. Table 3.4 is a summary of the cuts used to select Λ in the vicinity of electron. The Λ mass distribution for Run 1 data is shown in Figure 3.10. In the case of Λ_{CTC} , the Λ decay vertices are larger than 5.6 cm by definition. Therefore the background from prompt tracks combination is suppressed significantly. Clearly, the signal to background ratio of Λ_{CTC} is better than that of Λ_{SVX} , as shown in Figure 3.11. However, due to the improvement in hit resolutions, the Λ_{SVX} has a better mass resolution.

3.5 $\Lambda_c^+ \rightarrow \Lambda\pi^+\pi^+\pi^-$ Reconstruction

The signals of Λ_c are searched through the decay channel $\Lambda\pi^+\pi^+\pi^-$ and its charge conjugate from the $e\Lambda$ sample described in section 3.4. The 3 π tracks are selected within a cone size $\Delta R < 1$ around the electron. Each track is assigned the π mass. Among the 3 π tracks, we require two of them carry positive charge and one carries negative charge for the case of Λ , or

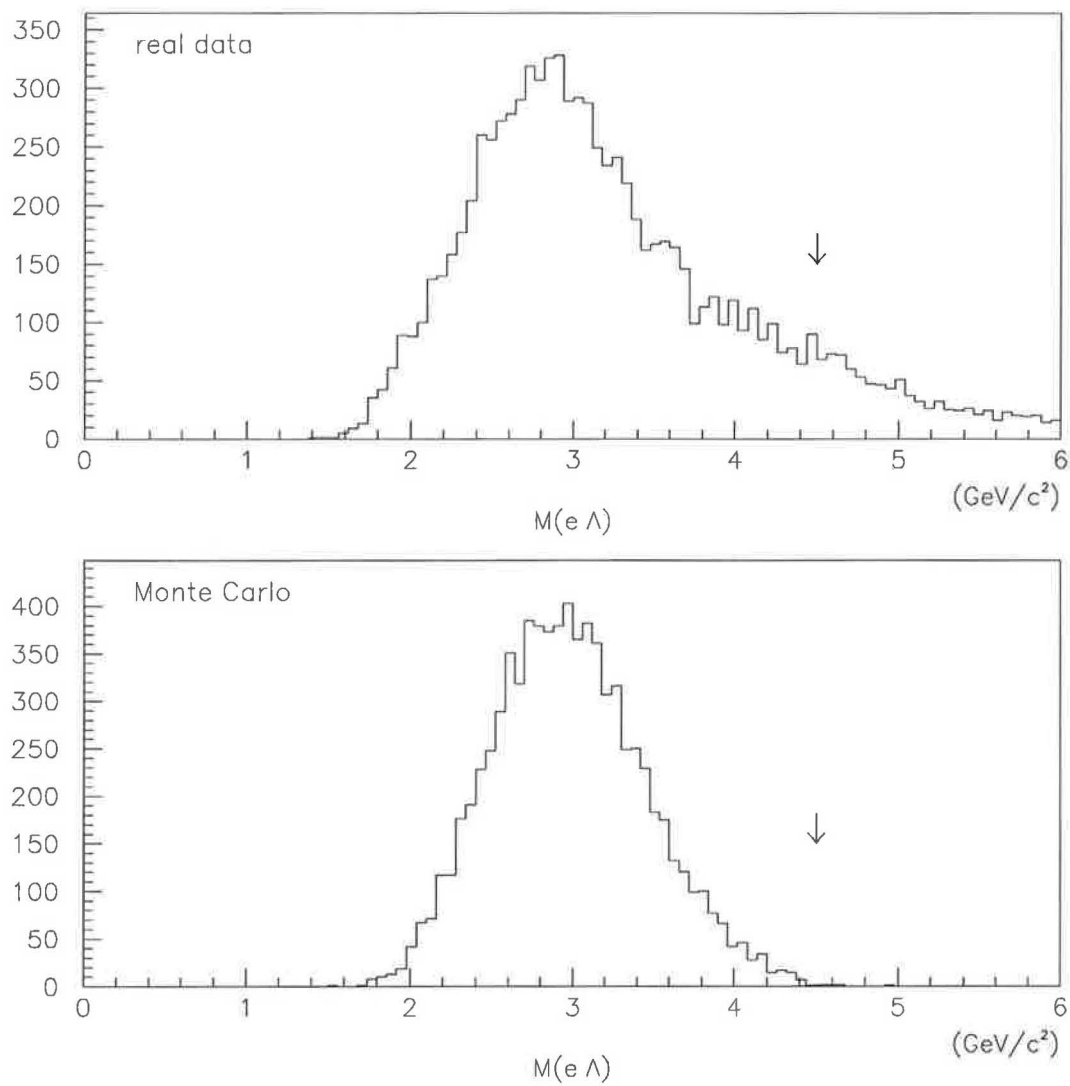


Figure 3.9: $M(e\Lambda)$ for real data(upper) and Monte Carlo(lower).

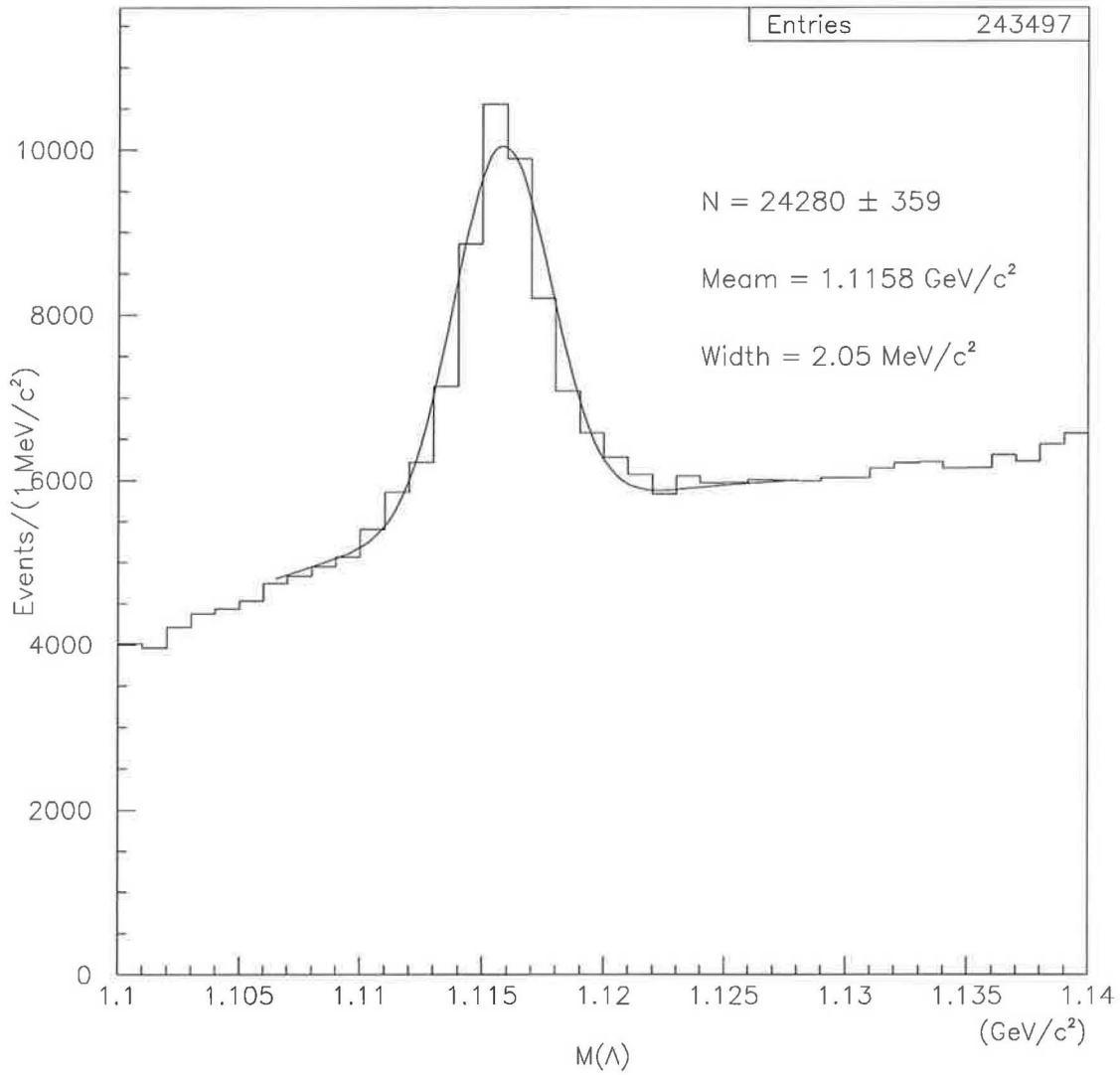


Figure 3.10: The distribution of Λ mass for the Λ candidates in the vicinity of electron for Run 1.

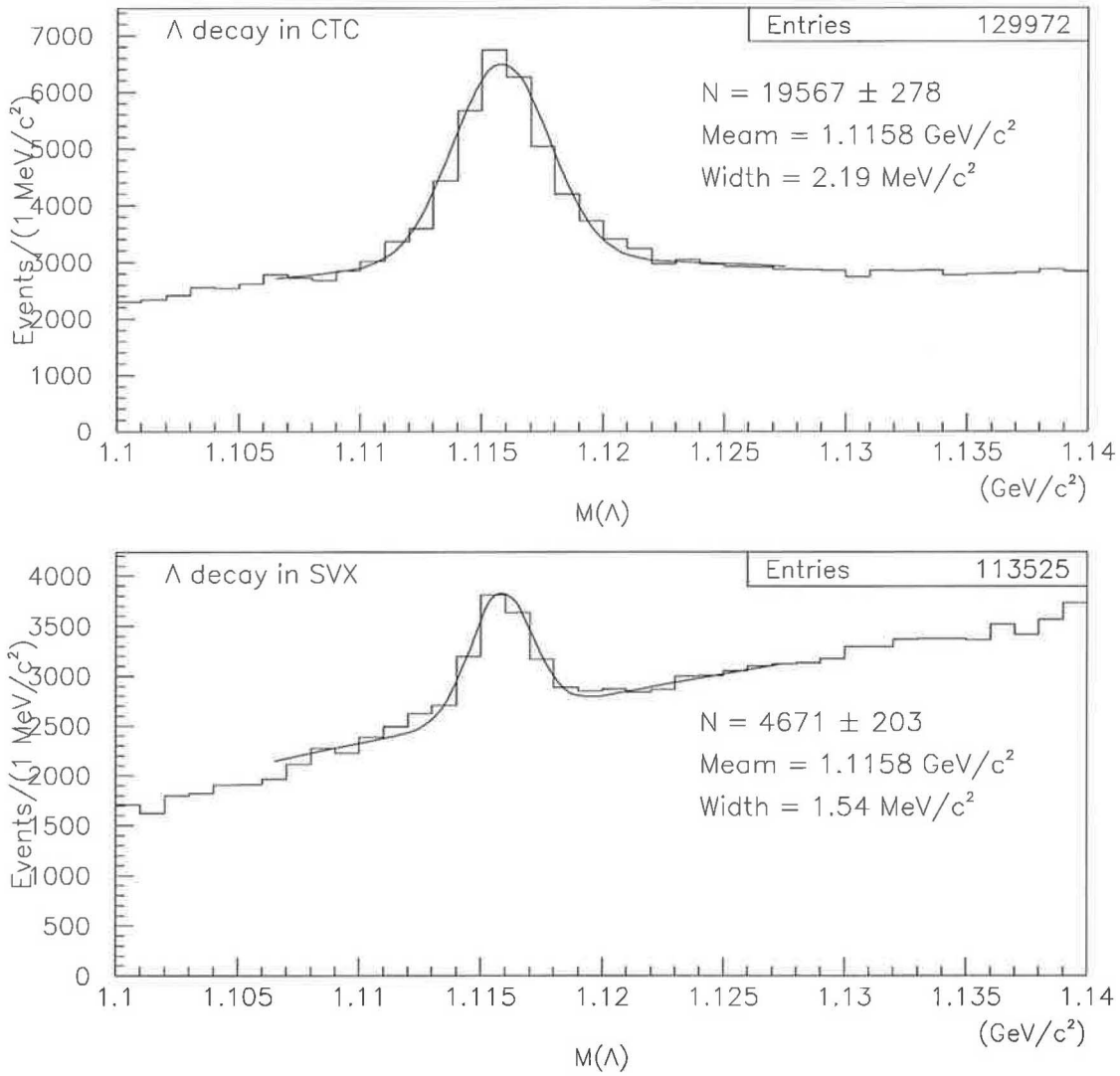


Figure 3.11: Λ mass for the cases of Λ_{CTC} and Λ_{SVX} .

$P_T(\pi)$	$> 0.3 \text{ GeV}/c$
$\Delta R(e\pi)$	< 1
$P_T(p)$	$> 0.4 \text{ GeV}/c$
$\Delta R(ep)$	< 1
$P_T(\Lambda)$	$> 1.5 \text{ GeV}/c$
$\Delta R(e\Lambda)$	< 1
Prob(χ^2) of Λ	$> 1\%$
$Lxy(\Lambda)$	$> 1 \sigma$
$M(\ell\Lambda)$	$< 4.5 \text{ GeV}/c^2$

Table 3.4: Selection requirement of Λ in the vicinity of electron.

the opposite for $\bar{\Lambda}$. Since Λ_c definitely decays inside the SVX detector, we require that all the 3 π tracks must be SVX tracks. The further cuts on kinematics, vertices and others are discussed in the following sections.

3.5.1 Pre-selection Cuts

In this decay channel there are 6 daughter tracks attached to 3 vertices: e^+ from Λ_b , $\pi^+ \pi^+ \pi^-$ from Λ_c , and $p \pi^-$ from Λ . We apply vertex constrained fitting on these 6 tracks and 3 vertices using CDF's internal secondary vertex fitting package CTVMFT [60]. We used a set of loose cuts, as shown in Table 3.5, to further reduce the data size. The resulting Λ_c mass is in Figure 3.12, where no signal can be seen.

3.5.2 Kinematics and Vertex Cuts

Since the mass resolution of Λ_{CTC} is larger than Λ_{SVX} , the final Λ mass selection windows is $5 \text{ MeV}/c^2$ for Λ_{CTC} and $4 \text{ MeV}/c^2$ for Λ_{SVX} . The $e\Lambda_c$ pair is from Λ_b decay, the natural upper limit of $M(e\Lambda_c)$ is the Λ_b mass, $5.6 \text{ GeV}/c^2$. The lower limit is cut at $3.5 \text{ GeV}/c^2$. The comparison between real data and Monte Carlo for the $P_T(e)$ and $M(e\Lambda_c)$ is in Figure 3.13.

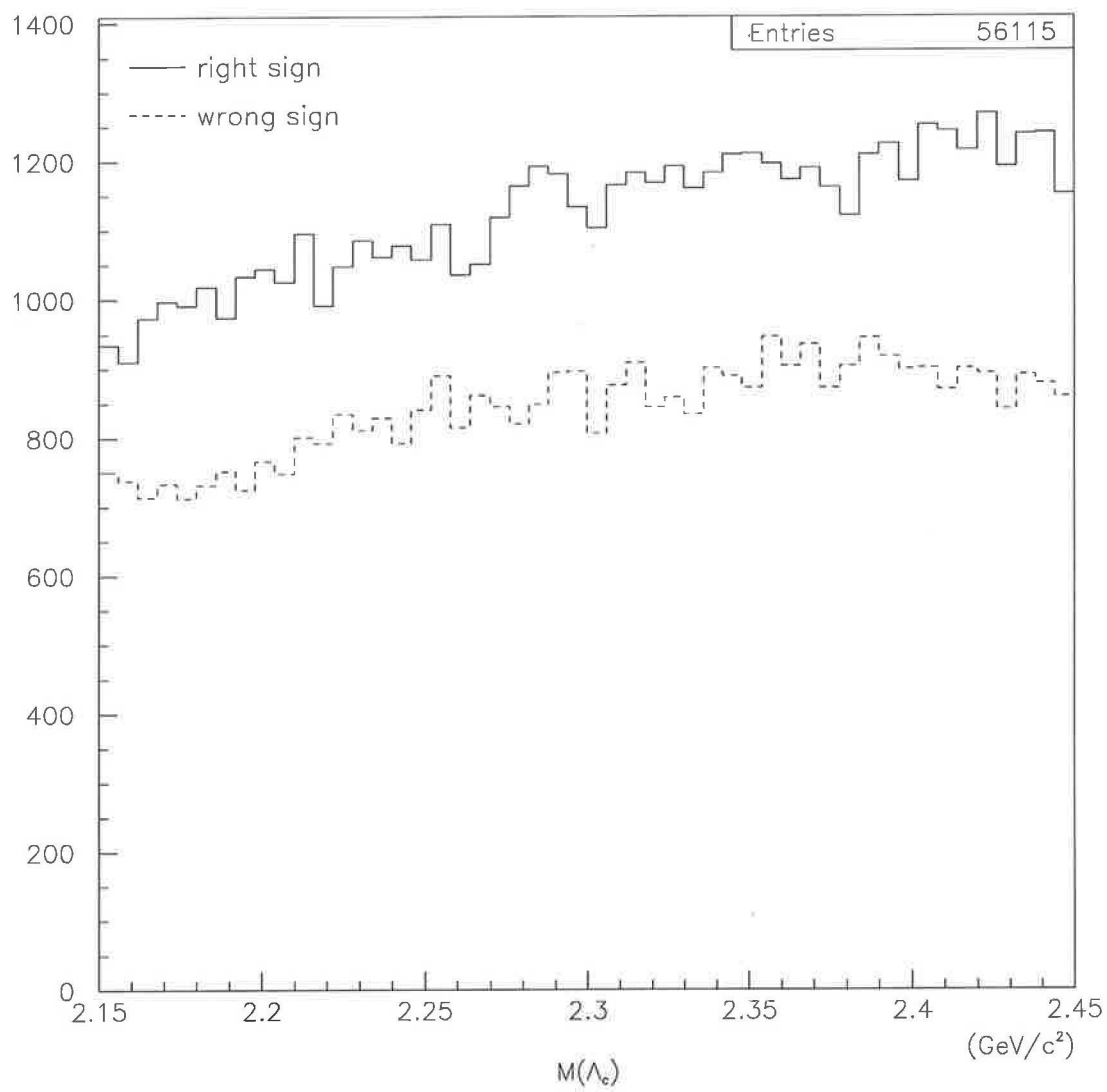


Figure 3.12: $M(\Lambda_c)$ in $\Lambda 3\pi$ channel with pre-selection cuts. No signal can be seen above the huge background.

$M(\Lambda)$	$< 1.128 \text{ GeV}/c^2$
$M(\Lambda)$	$> 1.104 \text{ GeV}/c^2$
$P_T(3\pi)$	$> 2.0 \text{ GeV}/c$
$\Delta R(e3\pi)$	< 0.8
$P_T(\Lambda_c)$	$> 4 \text{ GeV}/c$
$M(\Lambda_c)$	$> 2.15 \text{ GeV}/c^2$
$M(\Lambda_c)$	$< 2.45 \text{ GeV}/c^2$
$M(e\Lambda_c)$	$> 3.0 \text{ GeV}/c^2$
$M(e\Lambda_c)$	$< 5.6 \text{ GeV}/c^2$
$\Lambda_b - \Lambda_c - \Lambda$ vertices χ^2	< 100

Table 3.5: $\Lambda 3\pi$ pre-selection cuts.

We also apply the following 4 P_T cuts: $P_T(\Lambda) > 1.8 \text{ GeV}/c$, $P_T(3\pi) > 2.2 \text{ GeV}/c$, $P_T(\Lambda_c) > 4 \text{ GeV}/c$, and $P_T(e\Lambda_c) > 15 \text{ GeV}/c$. Their distributions are shown in Figure 3.14 and 3.15. The χ^2 in the fitting for 6 tracks and 3 vertices must be smaller than 45. The transverse decay length of Λ_c relative to the primary vertex, $L_{xy}(\Lambda_c)$, must be greater than 1σ . They are shown in Figure 3.16. To ensure good quality events for the lifetime measurement, the vertex uncertainty of Λ_b and Λ_c are required to be smaller than $500 \mu\text{m}$. Among the various kinematic and vertex cuts, the $L_{xy}(\Lambda_c)$ is the most important. The distribution of $L_{xy}(\Lambda_c)$ significance defined as the ratio of $L_{xy}(\Lambda_c)$ and its resolution, $L_{xy}(\Lambda_c)/\sigma$, is shown in Figure 3.17, where all the kinematic and vertex cuts are applied except the cut $L_{xy}(\Lambda_c)/\sigma > 1$. The long tail on the right hand side indicates that Λ_c might come from the secondary vertex which is obviously separated from the primary vertex. The Λ_c mass with the cut $L_{xy}(\Lambda_c)/\sigma > 1$ is also shown in the same plot. Figure 3.18 compares the Λ_c mass with and without the cut $L_{xy}(\Lambda_c)/\sigma > 1$. The huge background is reduced to a manageable level by this cut.

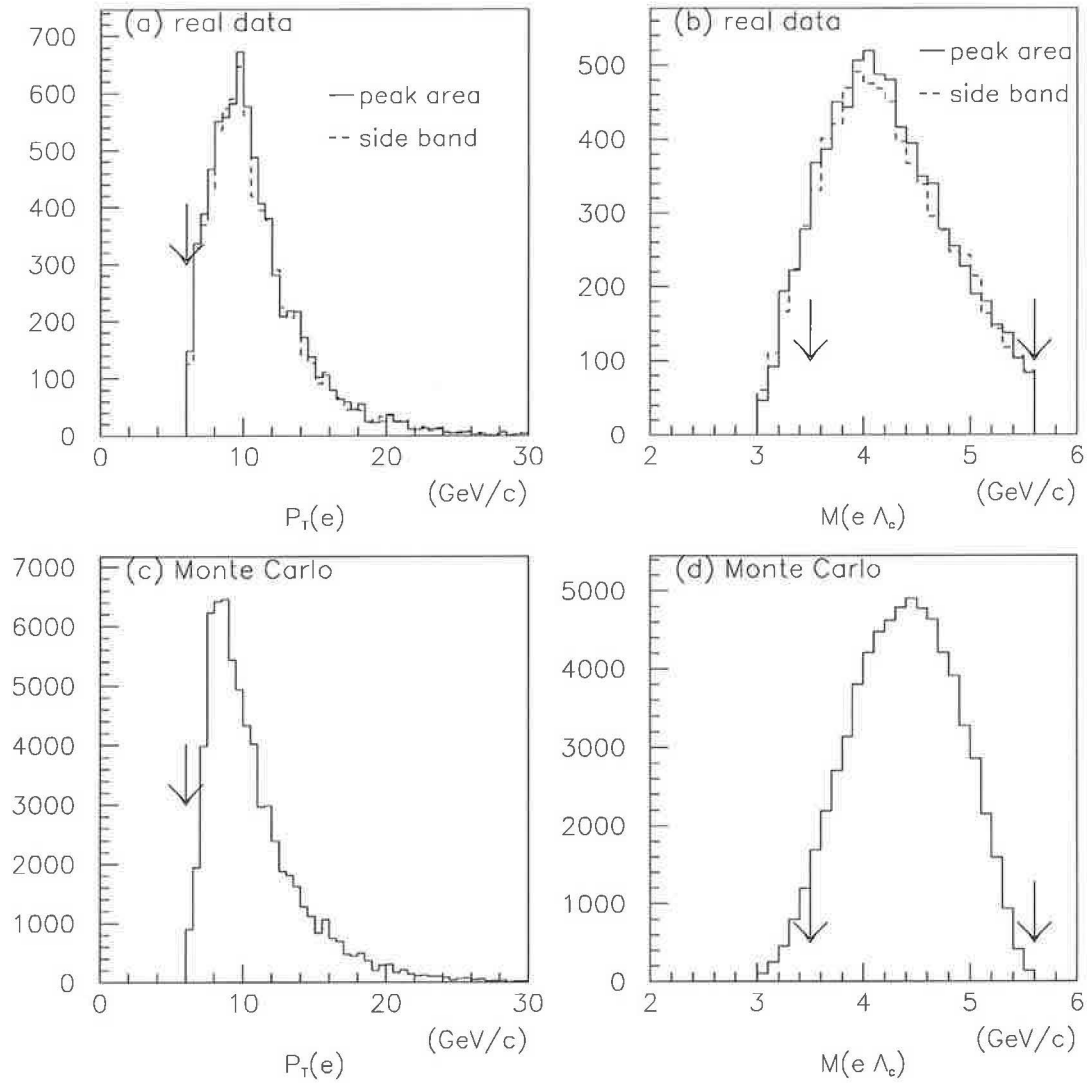


Figure 3.13: $P_T(e)$ and $M(e\Lambda_c)$ distributions with pre-selection cuts. (a) and (b) are for real data, (c) and (d) are for Monte Carlo. The downward arrows indicate the values for final cut.

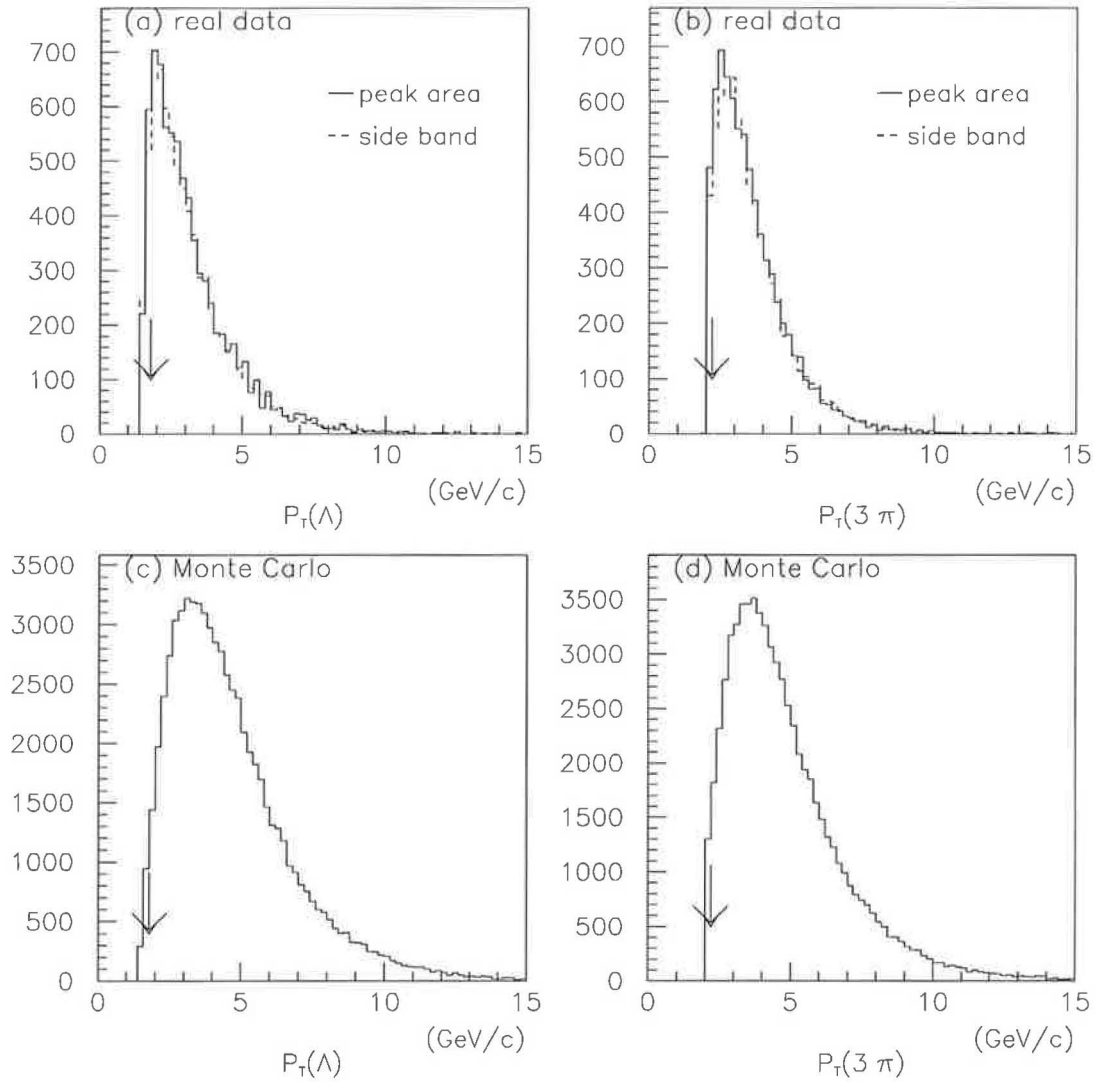


Figure 3.14: $P_T(\Lambda)$ and $P_T(3\pi)$ distributions with pre-selection cuts. (a) and (b) are for real data, (c) and (d) are for Monte Carlo. The downward arrows indicate the values for final cut.

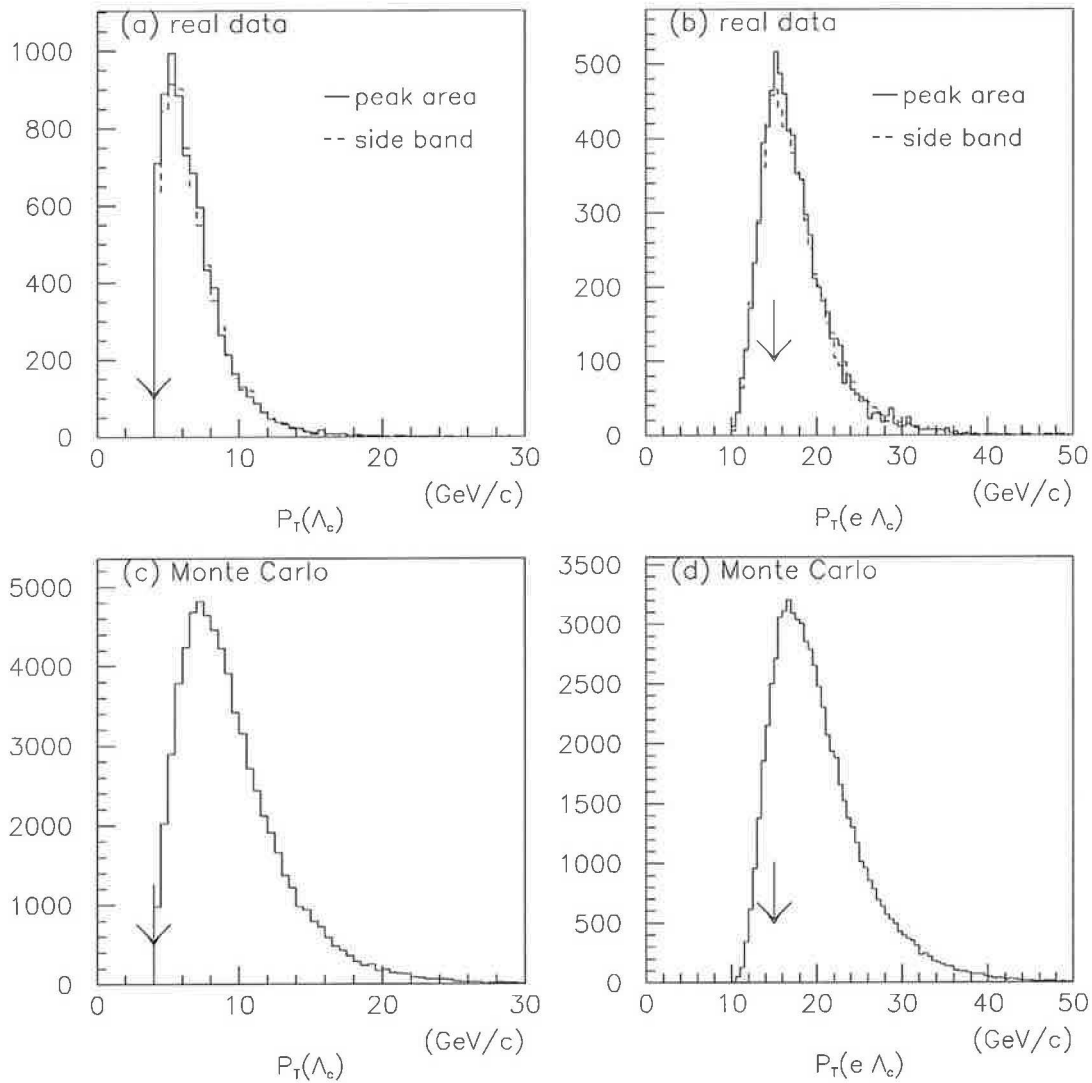


Figure 3.15: $P_T(\Lambda_c)$ and $P_T(e\Lambda_c)$ distributions with pre-selection cuts. (a) and (b) are for real data, (c) and (d) are for Monte Carlo. The downward arrows indicate the values for final cut.

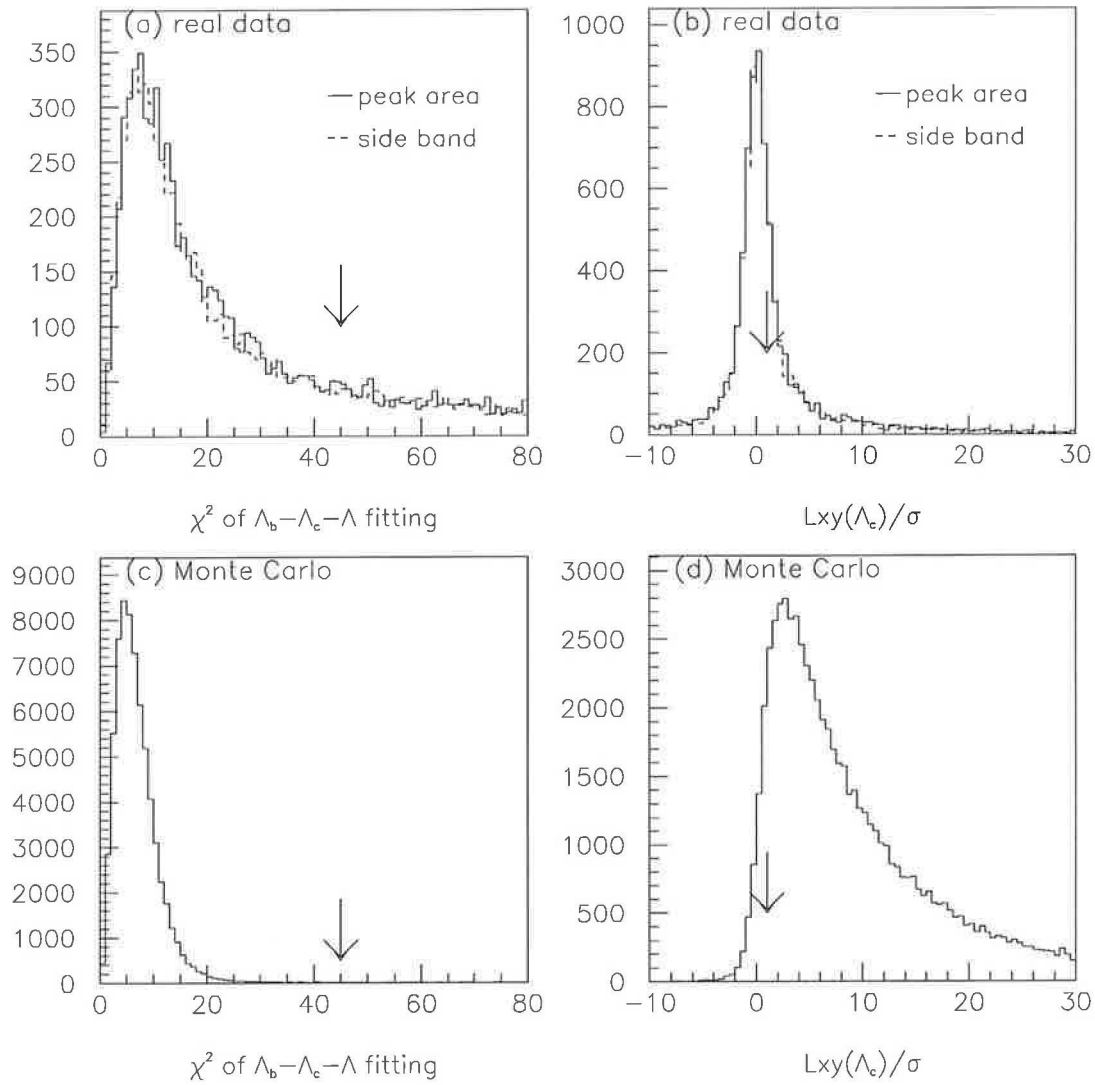


Figure 3.16: χ^2 of vertices fitting and $L_{xy}(\Lambda_c)$ significance distributions with pre-selection cuts. (a) and (b) are for real data, (c) and (d) are for Monte Carlo. The downward arrows indicate the values for final cut.

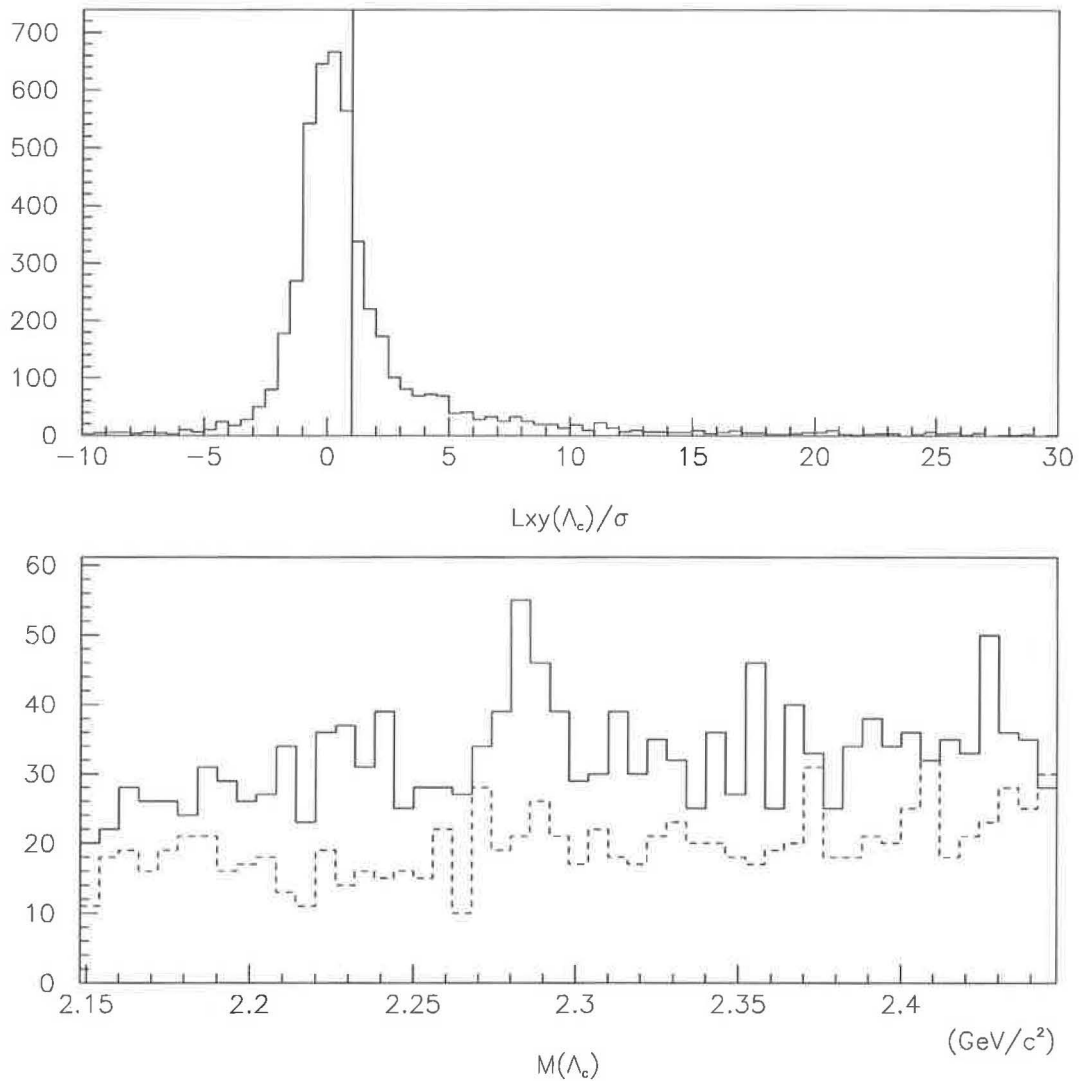


Figure 3.17: $L_{xy}(\Lambda_c)$ significance with all the other kinematic and vertex cuts(upper). After the cut $L_{xy}(\Lambda_c) > 1\sigma$ the signal become clear.

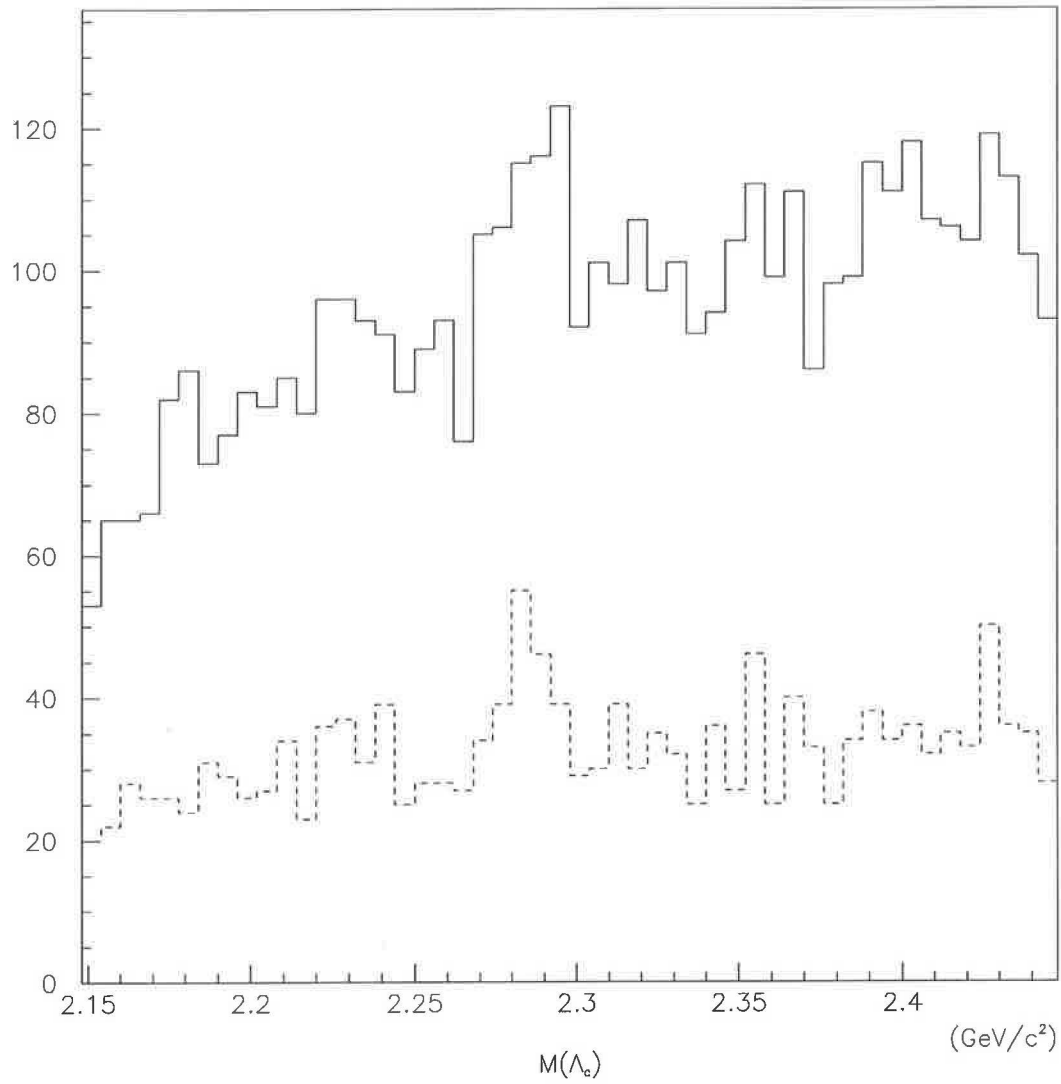


Figure 3.18: Solid(dash) line shows the result without(with) the cut $L_{xy}(\Lambda_c) > 1\sigma$. The signal is much better with this cut.

3.5.3 K_s^0 Reflection Removal and dE/dX

In the method of Λ selection, p mass is assigned to the track with higher P_T and π mass to the other track. In $p\bar{p}$ environment, K_s^0 production cross section is several times higher than Λ . With the wrong mass assignment, K_s^0 can be mis-identified as Λ . We call this as the K_s^0 reflection background. The detail is discussed in Appendix A. To see how many Λ 's are reflected from K_s^0 , we assign π mass to the p candidate and repeat the invariant mass calculation. Figure 3.19 shows the spectrum of K_s^0 reflection. Λ candidates are removed if they lie in the range of $0.4977 \pm 0.020 \text{ GeV}/c^2$ with the new mass assignments .

In CDF, the energy loss information(dE/dX) collected in CTC can be used to distinguish proton from other particle species. We define a variable *proton level*, or $\text{level}(p)$, based on the difference of energy loss per unit length between the measured value and the predicted value. The exact definition is in Appendix A. For a real proton the $\text{level}(p)$ is close to 1, while for other particles it's close to 0. Figure 3.20 shows the distributions of $\text{level}(p)$ and the Λ_c mass spectrum. In this plot we have applied the cut $\text{level}(p) > 0.2$. Appendix A contains more discussions about this cut.

3.5.4 Λ_c Signal Result

All the cuts we used in the Λ_c search are summarized in Table 3.6. The final candidate sample we used for Λ_b lifetime analysis can be seen in Figure 3.21. 57 ± 12 events are reconstructed. The Λ_c spectrum for wrong charge combination pairs, i.e., $e^+\Lambda_c^+$ and $e^-\Lambda_c^-$, is also shown. No signal is seen with wrong charge combination.

We compare various kinematics and lepton impact parameter distributions between data and Monte Carlo. In Figure 3.21 the peak area is defined as $2.285 \pm 0.020 \text{ GeV}/c^2$ while the

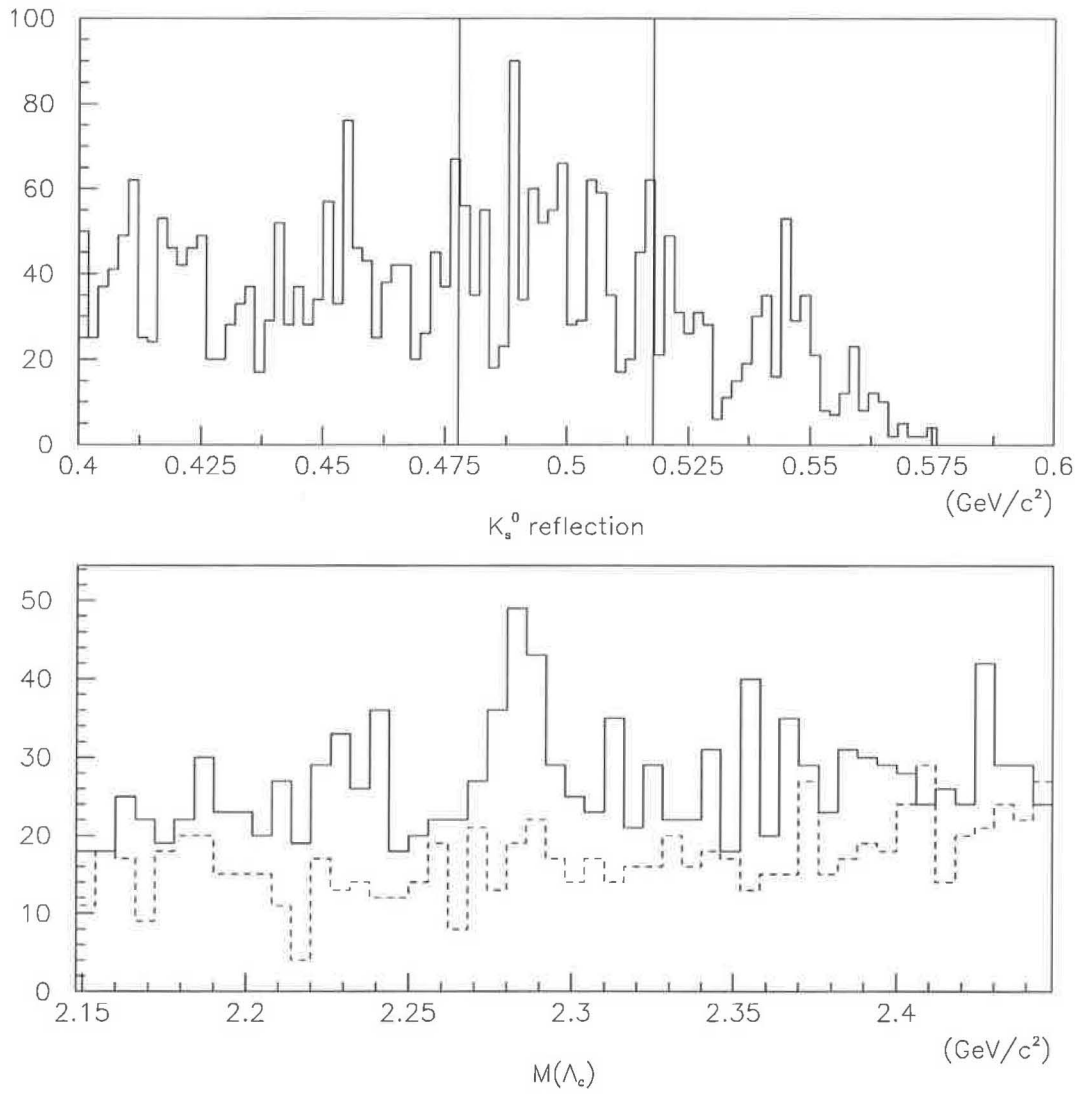


Figure 3.19: K_s^0 reflection spectrum with new mass assignment to Λ candidate (upper), and the Λ_c mass after K_s^0 reflection removal (lower).

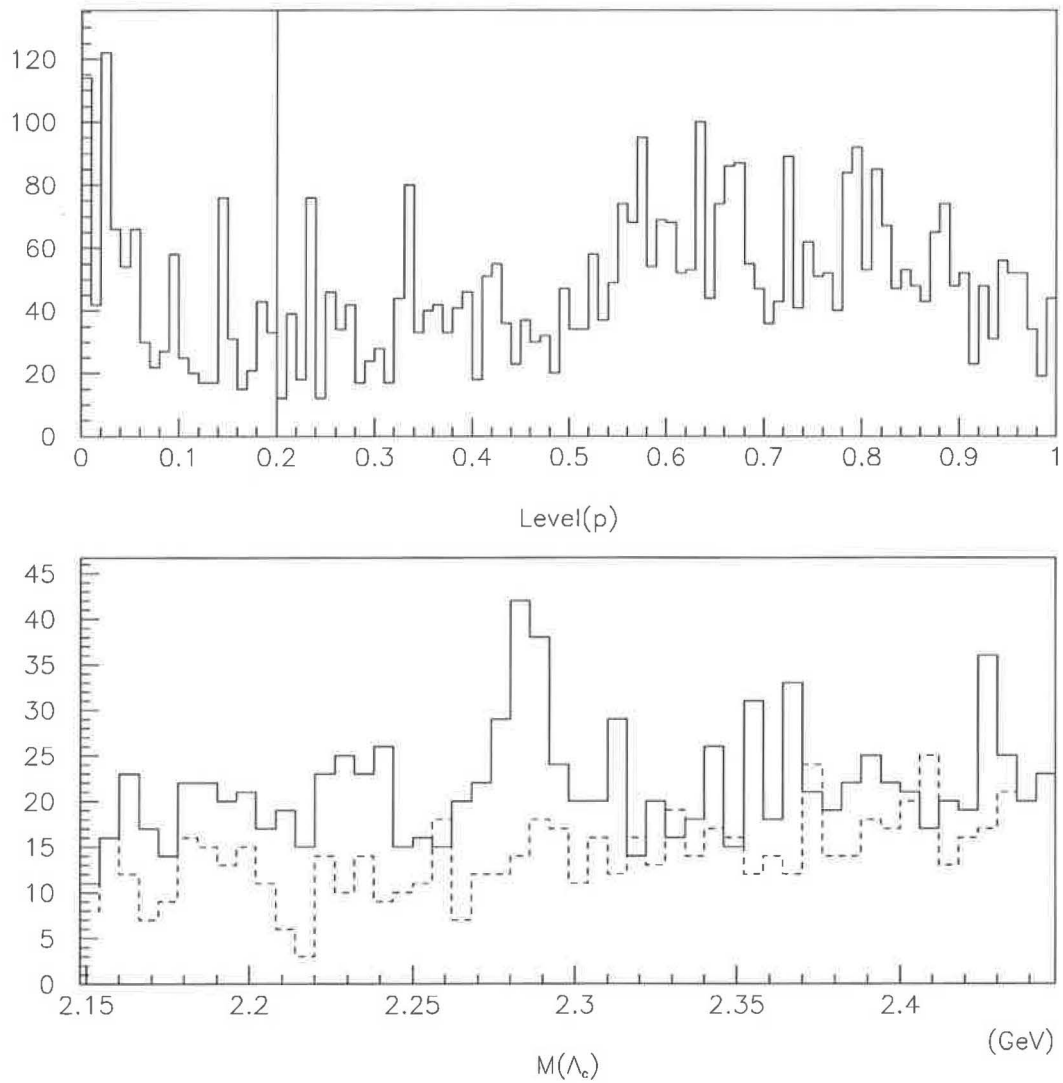


Figure 3.20: Level(p) distribution for Λ_c candidates (upper), and the Λ_c mass after the cut of level(p) > 0.2.

$ M(\Lambda_{CTC}) - 1.1157 $	$< 0.005 \text{ GeV}/c^2$
$ M(\Lambda_{SVX}) - 1.1157 $	$< 0.004 \text{ GeV}/c^2$
$P_T(\Lambda)$	$> 1.8 \text{ GeV}/c$
$\Delta R(e\Lambda)$	< 0.6
$P_T(3\pi)$	$> 2.2 \text{ GeV}/c$
$\Delta R(e3\pi)$	< 0.8
$P_T(\Lambda_c)$	$> 4 \text{ GeV}/c$
$\Delta R(e\Lambda_c)$	< 0.6
$P_T(e\Lambda_c)$	$> 15 \text{ GeV}/c$
$M(e\Lambda_c)$	$> 3.5 \text{ GeV}/c^2$
$M(e\Lambda_c)$	$< 5.6 \text{ GeV}/c^2$
Λ vertex $\text{Prob}(\chi^2)$	$> 1\%$
$Lxy(\Lambda)/\sigma$	> 2.0
$Lxy(\Lambda - \Lambda_c)/\sigma$	> 0
$\Lambda_b - \Lambda_c - \Lambda$ vertices χ^2	< 45
$Lxy(\Lambda_c)/\sigma$	> 1.0
σ of $Lxy(\Lambda_c)$	$< 0.05 \text{ cm}$
σ of $Lxy(\Lambda_b)$	$< 0.05 \text{ cm}$
K_s^0 removal	$ M(K_s^0) - 0.4977 < 0.020 \text{ GeV}/c^2$
$level(p)$	> 0.2

Table 3.6: Event selection cuts for $\Lambda_c \rightarrow \Lambda 3\pi$ signal search.

side-band areas are defined as $2.200 \pm 0.020 \text{ GeV}/c^2$ and $2.370 \pm 0.020 \text{ GeV}/c^2$. To compare with Monte Carlo, the distributions for the events in side-band areas are subtracted from the peak area. The distributions after this sideband subtraction procedure are shown in Figure 3.22 and 3.23.

3.6 Background

In this analysis, we are looking for the signal of electron Λ_c pairs with proper charge correlation. However, the electrons and Λ_c particles can come from many different sources in the $p\bar{p}$ collisions. Some of them had been studied at CDF [38, 62]. We briefly discuss them below. In addition, the K_s^0 reflection backgrounds from the charm hadron decays are unique in this analysis. We also describe them in this section.

The B hadrons background

The right sign combination of electron and Λ_c pairs coming from the single B hadron decays are shown below:

- $\Lambda_b \rightarrow \Lambda_c^+ D_s^- X, D_s^- \rightarrow e^- X'$
- $B \rightarrow \Lambda_c^+ D_s^- \bar{N} X, D_s^- \rightarrow e^- X'$

In this background, the electrons coming from the D_s have softer momentum. They are rejected by the invariant mass cut $M(e\Lambda_c) > 3.5 \text{ GeV}/c^2$ and the kinematics cut of $P_T(e\Lambda_c) > 15 \text{ GeV}/c^2$. The branching ratio of $D_s^- \rightarrow e^- X$ was measured to be $8_{-5}^{+6} \%$, which further suppresses this background.

CDF preliminary

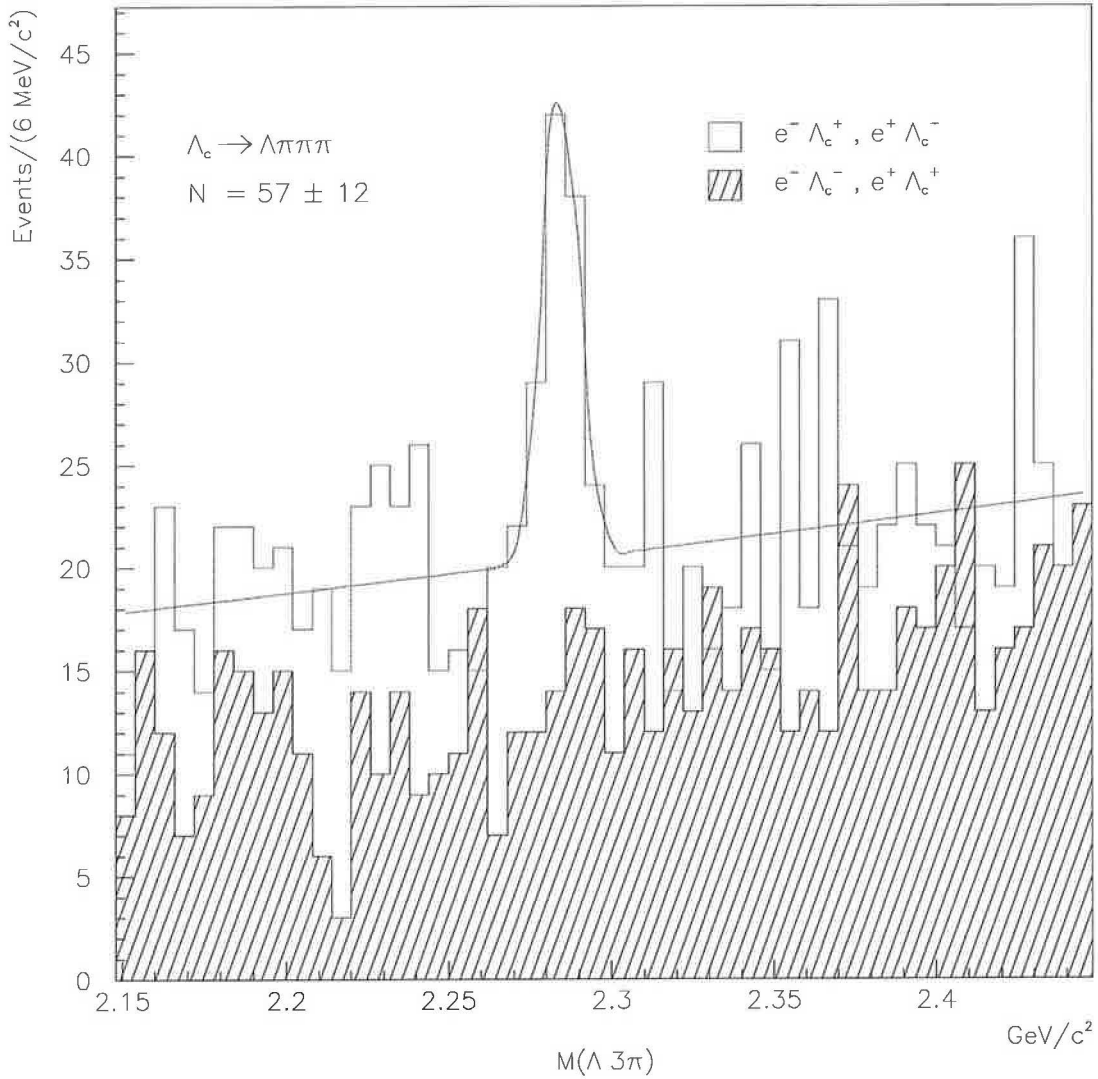


Figure 3.21: The $M(\Lambda 3\pi)$ distribution of the final $\Lambda_c \rightarrow \Lambda \pi \pi \pi$ candidates. The shaded area is for wrong sign combination.

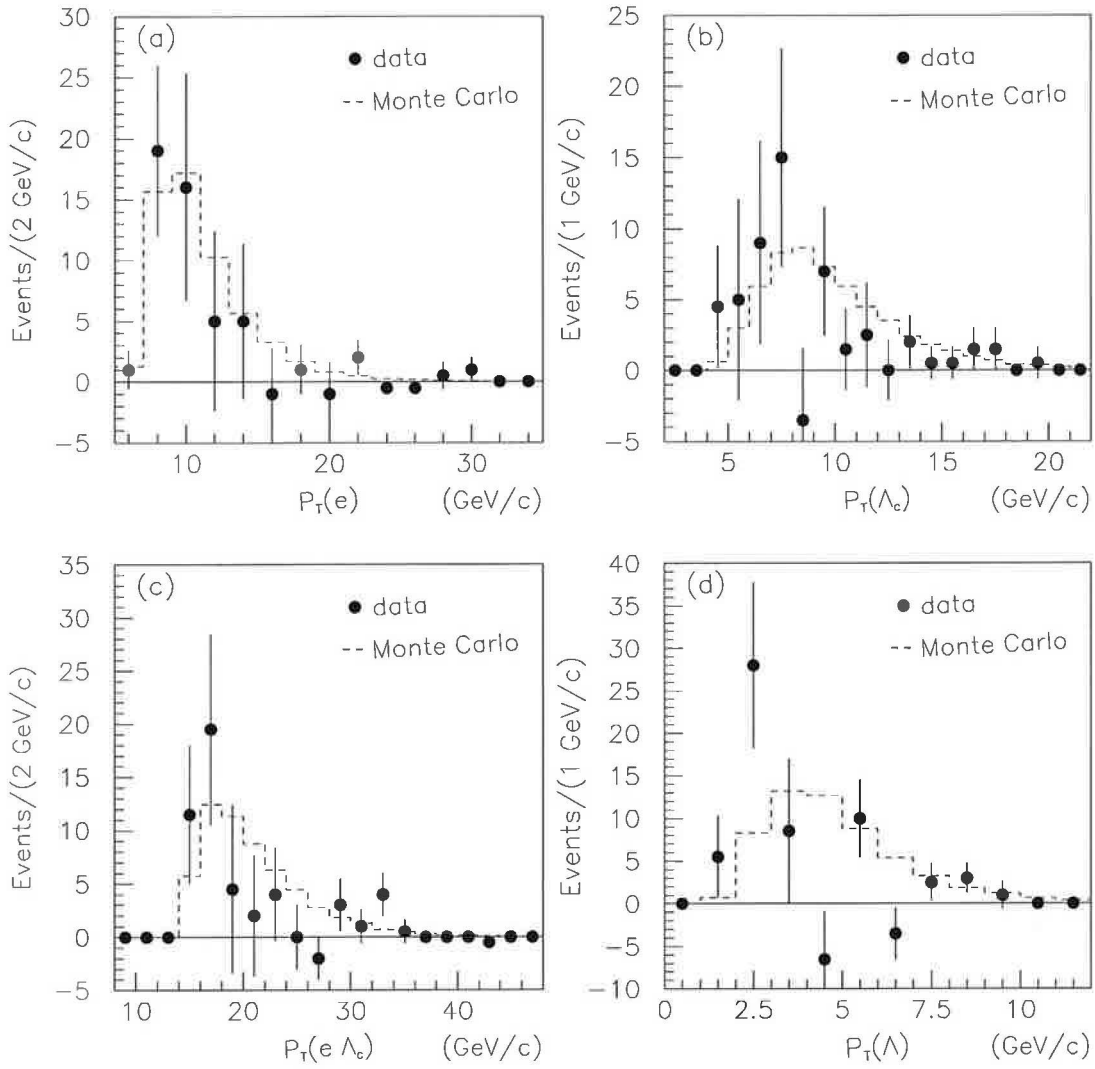


Figure 3.22: Data and Monte Carlo comparison for (a) $P_T(e)$, (b) $P_T(\Lambda_c)$, (c) $P_T(e\Lambda_c)$, and (d) $P_T(\Lambda)$, after side-band subtraction for the data.

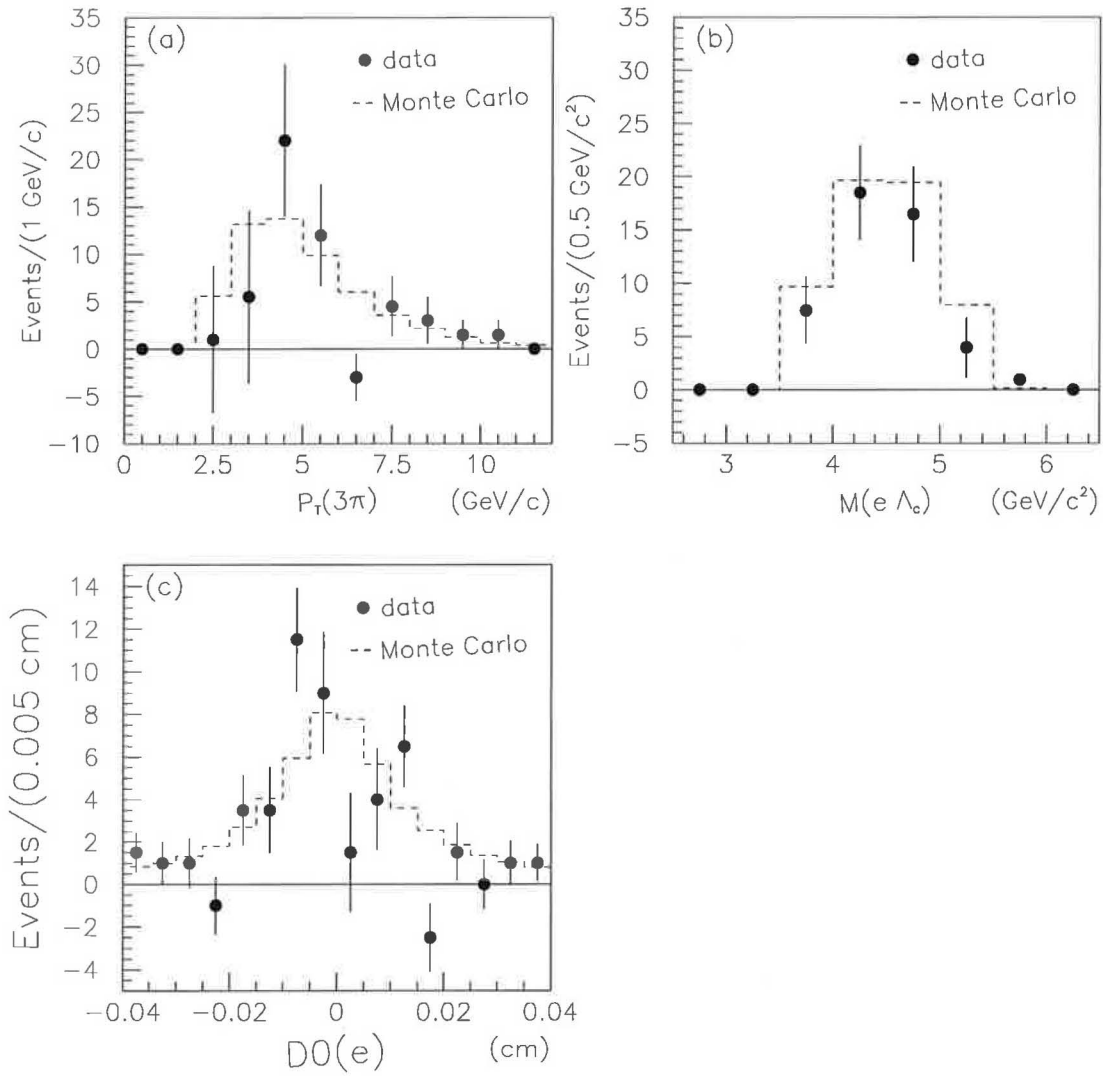


Figure 3.23: Data and Monte Carlo comparison for (a) $P_T(3\pi)$, (b) $M(e\Lambda_c)$, and (c) impact parameter of electron $D(e)$, after side-band subtraction for the data.

The heavy quark pairs background

The $b\bar{b}$ pair become a background source when an electron is produced from one of the b quark while a Λ_c particle is produced from the other b quark. The $b\bar{b}$ pairs produced from the quark-antiquark annihilation process are back-to-back pair in ϕ -coordinate; their invariant mass $M(e\Lambda_c)$ will be too large to pass the cut $M(e\Lambda_c) < 5.6$. For the case of gluon splitting process, the b and \bar{b} are very close to each other. The cut $M(e\Lambda_c) < 5.6$ might not be able to reject this background. However, the e and Λ_c pair from $b\bar{b}$ pair has wrong charge correlation. Since no mass peak is found for the wrong sign pairs, this background therefore is negligible.

The charm mesons background

Because the production rate of B^0 and B_s is about 5 times higher than Λ_b ². The semileptonic decays of $B^0 \rightarrow D^+e^-\bar{\nu}_e$ and $B_s \rightarrow D_s e^-\bar{\nu}_e$ will become the background sources when the charm meson daughters decay to K_s^0 plus 3 tracks, and the K_s^0 particles are misidentified as Λ , as shown in Table 3.7.

$D^+ \rightarrow \bar{K}^0 \pi^+ \pi^+ \pi^-$	$7.0 \pm 0.9 \%$
$D^+ \rightarrow K^0 \pi^+ \pi^+ K^-$	$1.0 \pm 0.6 \%$
$D_s \rightarrow \bar{K}^0 K^+ \pi^+ \pi^-$	$< 2.8 \%$
$D_s \rightarrow K^0 \pi^+ \pi^+ K^-$	$4.3 \pm 1.5 \%$

Table 3.7: The examples of charm mesons decays with the K_s^0 plus 3 tracks.

These backgrounds are supposed to be rejected by the K_s^0 removal cut: $|M(K_s^0) - 0.4977| < 0.02 \text{ GeV}/c^2$. The uncertainty of $M(K_s^0)$ from the data is about $0.0055 \text{ GeV}/c^2$; the K_s^0 within $\pm 3.6 \sigma$ are rejected.

²The production fractions for the major b hadrons are $39.7_{-2.2}^{+1.8}\%$ for B^+ , $39.7_{-2.2}^{+1.8}\%$ for B^0 , $10.5_{-1.7}^{+1.8}\%$ for B_s , and $10.1_{-3.1}^{+3.9}\%$ for Λ_b .

The combinatorial background

The Λ candidates plus the random combinations of three tracks contribute a certain fraction to the fake Λ_c background. Since there is no physics source responsible for this background, the fake Λ_c has not charge correlation with the lepton.

The electrons background

The photon conversion electrons could survive if one of the electron track in the e^+e^- pair is not detected. This is a true electron background. However, the residual conversion electrons are not supposed to have any charge correlation with the Λ_c . This background should contribute equally in the right sign and wrong sign combination, and in the wrong sign pair we do not see any signal.

There are also some fake electron backgrounds. For example, the charged hadrons depositing most of their energy in EM calorimeters or coming along with photons could be identified as electrons. Since these fake electron candidates do not have charge correlation with Λ_c . We can monitor this background from the wrong sign combination.

In summary, we reject the background using the kinematics properties of the $\Lambda_c^+e^-$ system, and monitor the remaining background from the wrong sign $\Lambda_c e$ pairs. In the lifetime measurement, the background contributions are modeled based on a properly selected background sample and are subtracted from the data.

Chapter 4

Lifetime Fitting

In this chapter, we discuss the method to reconstruct Λ_b vertex and describe the procedures to extract Λ_b lifetime from the $\ell\Lambda_c$ signal we obtained in section 3.5. In the decay channel of $\Lambda_b \rightarrow e^- \bar{\nu}_e \Lambda_c^+ \rightarrow e^- \bar{\nu}_e \Lambda \pi^+ \pi^+ \pi^-$, 3 decay vertices, including the secondary vertex (Λ_b), tertiary vertex (Λ_c), and fourth vertex (Λ) are involved besides the primary vertex. Although these 3 vertices can be simultaneously reconstructed using CDF's vertex-constrained fitting package [60], the vertex uncertainty estimation becomes more complicated when more vertices are involved. For example, it is straightforward to calculate the Λ vertex uncertainty which only depends on the tracking parameter uncertainties of its two daughter particles, p and π . This two-track vertex is well understood at CDF. On the other hand, the Λ_b vertex uncertainty depends on the vertex uncertainties of Λ_c and Λ , as well as the tracking parameter uncertainties of lepton track, 3π tracks and p, π tracks. It requires more efforts to verify the reliability of Λ_b vertex uncertainty estimation in such a case. Fortunately, the 3 π tracks in the decay $\Lambda_c \rightarrow \Lambda 3\pi$ all have SVX information which can be used to determine a clear Λ_c vertex. Incorporating the lepton track, we can reconstruct the Λ_b vertex as well. This method is described in section 4.1. We deal with the lifetime fitting procedures in section 4.2. The discussion of the systematic error for this lifetime fitting procedures is presented in section 4.3.

4.1 Λ_b Vertex and Decay Length

The topology of the daughter tracks and vertices in the $\Lambda 3\pi$ channel is shown in Figure 4.1. Λ_b is produced at the primary vertex (PV) and decays at the secondary vertex (X_B, Y_B) . The lepton(ℓ) in the semileptonic decay has azimuthal angle Φ_E . The closest point to the primary vertex for the lepton track on the transverse plane is (X_E, Y_E) , where Φ_E is evaluated. The distance between (X_E, Y_E) and the primary vertex is denoted as d_E , which is also called the transverse impact parameter of the lepton track. The neutrino (ν) from the Λ_b semileptonic decay is not detectable in CDF detector. The dash line means that there is no track associated with ν . Λ_c is produced at (X_B, Y_B) and decays at the tertiary vertex (X_D, Y_D) . The azimuthal angle of Λ_c is denoted as Φ_D . The proper decay lengths of Λ_b and Λ_c are about $400 \mu\text{m}$ and $60 \mu\text{m}$ respectively. Considering the boost factor of about 3, the typical distance between (X_D, Y_D) and the primary vertex is smaller than 1.5 mm. This characteristics ensures that all the 3 π tracks will travel through the SVX detector and have SVX tracking information. This enable us to determine Λ_c vertex without the information from Λ . The long-lived neutral particle Λ is produced at the tertiary vertex (X_D, Y_D) . It leaves no tracking information and is able to travel tens of centi-meters. If its decay length is larger than 5.6 cm ¹ then only CTC tracking information is available for its two daughter tracks p and π . The CTC tracking has poorer resolution ($\sigma_{hit} \sim 200 \mu\text{m}$) compared with SVX tracking ($\sigma_{hit} \sim 15 \mu\text{m}$). In our current method, Λ serves as an event tagging and does not have effects in Λ_b vertex determination.

The Λ_c vertex can be obtained from the 3 π tracks using CDF's vertex-constrained fitting package CTVMFT [60]. $P_T(\Lambda_c)$ can be calculated from $P_T(\Lambda)$ and $P_T(3\pi)$. To determine Λ_b vertex (X_B, Y_B) we can draw a straight line from (X_D, Y_D) , pointing backward along $P_T(\Lambda_c)$

¹see section 3.4

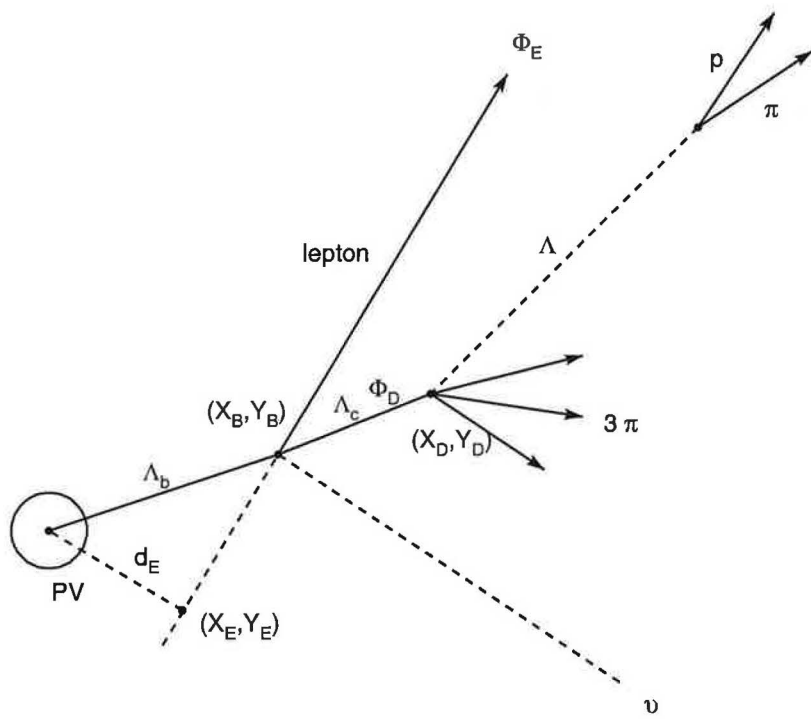


Figure 4.1: Schematic view of the decay $\Lambda_b \rightarrow e^- \bar{\nu}_e \Lambda_c^+ \rightarrow e^- \bar{\nu}_e \Lambda \pi^+ \pi^- \pi^-$, in which the transverse decay length L_{xy} for Λ_b lifetime fitting is defined as the distance between (X_B, Y_B) and the primary vertex(PV).

and making an intersection with the lepton track. The intersection point then is the Λ_b vertex. The lepton and the Λ_c are both charged particles. The projection of their trajectories on the transverse plane are circular curves in CDF coordinate system. The curvature is proportional to the inverse of track P_T , so the radii of these circular curves are proportional to the track P_T . With the requirements of $P_T(\ell) > 6 \text{ GeV}/c$ and $P_T(\Lambda_c) > 4 \text{ GeV}/c$, the radii corresponding to the transverse trajectories of lepton and Λ_c are 1418 cm and 946 cm respectively. Since the decay length of Λ_c with Lorentz boost is about $3 \times 60 \mu\text{m} \sim 180 \mu\text{m}$, it's about 4 order of magnitude smaller than the radii of lepton and Λ_c trajectories, the tracks of the lepton and Λ_c can be approximated by straightlines. The position of the secondary vertex can be expressed as:

$$\begin{aligned}
X_B &= \frac{Y_E - Y_D + X_D \tan \Phi_D - X_E \tan \Phi_E}{\tan \Phi_D - \tan \Phi_E} \\
Y_B &= \frac{X_E - X_D + Y_D \cot \Phi_D - Y_E \cot \Phi_E}{\cot \Phi_D - \cot \Phi_E}
\end{aligned} \tag{4.1}$$

Uncertainties associated with the lepton track and the Λ_c vertex will propagate to the Λ_b vertex's uncertainty. There are several factors involved in this error propagation, as listed below.

- uncertainty of the tertiary vertex : σ_{X_D} and σ_{Y_D}
- uncertainty of the tertiary vertex's direction : σ_{Φ_D}
- uncertainty of the lepton transverse impact parameter : σ_{d_E}
- uncertainty of the lepton azimuthal direction : σ_{ϕ_E}

- uncertainty of the lepton curvature : σ_{C_E}

Since a straightline is a good approximation for the lepton track, σ_{C_E} can be neglected. The decay length of Λ_c is around a few hundred μm , σ_{Φ_D} only contributes a tiny portion to the Λ_b vertex uncertainty. In the following context, we only consider σ_{X_D} , σ_{Y_D} , σ_{d_E} and σ_{Φ_E} in the error propagation. The error matrix of the lepton + Λ_c system can be expressed as in equation (4.2) .

$$M_{\ell\Lambda_c} = \begin{pmatrix} \sigma_{X_D}^2 & \sigma_{X_D, Y_D} & 0 & 0 \\ \sigma_{Y_D, X_D} & \sigma_{Y_D}^2 & 0 & 0 \\ 0 & 0 & \sigma_{d_E}^2 & 0 \\ 0 & 0 & 0 & \sigma_{\Phi_E}^2 \end{pmatrix} \quad (4.2)$$

The transformation matrix Λ_{TM} is obtained from taking the derivative of equation (4.1) with respect to X_D , Y_D , d_E and Φ_E .

$$\begin{aligned} \Lambda_{TM} &= \begin{pmatrix} \frac{\partial X_B}{\partial X_D} & \frac{\partial X_B}{\partial Y_D} & \frac{\partial X_B}{\partial d_E} & \frac{\partial X_B}{\partial \Phi_E} \\ \frac{\partial Y_B}{\partial X_D} & \frac{\partial Y_B}{\partial Y_D} & \frac{\partial Y_B}{\partial d_E} & \frac{\partial Y_B}{\partial \Phi_E} \end{pmatrix} \\ &= \frac{1}{\sin(\Phi_D - \Phi_E)} \begin{pmatrix} \sin \Phi_D \cos \Phi_E & -\cos \Phi_D \cos \Phi_E & \cos \Phi_D & S \cos \Phi_D \\ \sin \Phi_D \sin \Phi_E & -\cos \Phi_D \sin \Phi_E & \sin \Phi_D & S \sin \Phi_D \end{pmatrix} \end{aligned} \quad (4.3)$$

Where S is the distance between (X_E, Y_E) and (X_B, Y_B) . The error propagation from the error matrix $M_{\ell\Lambda_c}$ for the $\ell + \Lambda_c$ system to the error matrix M_{Λ_b} for the Λ_b vertex is expressed as:

$$M_{\Lambda_b} = \begin{pmatrix} \sigma_{X_B, X_B} & \sigma_{X_B, Y_B} \\ \sigma_{Y_B, X_B} & \sigma_{Y_B, Y_B} \end{pmatrix} = \Lambda_{TM} \times M_{\ell\Lambda_c} \times \Lambda_{TM}^T \quad (4.4)$$

where Λ_{TM}^T is the transport matrix of Λ_{TM} .

The complete expression of Λ_b vertex (X_B, Y_B) and its associated error matrix M_{Λ_b} are non-linear equations. In a formal vertex-constrained fitting procedure they are obtained through iterative calculations. In our simplified method described in this section, however, they are estimated analytically using approximations. The Λ_c vertex and its error matrix of course still depend on the vertex-constrained fitting procedure method. But it is a three-track vertex, we have better understanding of it. In order to verify this method, we examine the pull distributions of the X and Y positions of Λ_c and Λ_b vertices, i.e., $V_X(\Lambda_c), V_Y(\Lambda_c), V_X(\Lambda_b)$, and $V_Y(\Lambda_b)$ in a Monte Carlo sample, as shown in Figure 4.2. The pull quantity, using $V_X(\Lambda_b)$ as example, is defined as,

$$\text{pull of } V_X(\Lambda_b) = \frac{V_X^{REC}(\Lambda_b) - V_X^{MC}(\Lambda_b)}{\sigma(V_X(\Lambda_b))} \quad (4.5)$$

where $V_X^{REC}(\Lambda_b)$ and $\sigma(V_X(\Lambda_b))$ are the X position of Λ_b vertex and its uncertainty from our calculation, and $V_X^{MC}(\Lambda_b)$ is the true X position of Λ_b vertex in the Monte Carlo sample. For a correctively estimated variable, its pull distribution is expected to be a Gaussian function with mean value consistent with 0, and the width consistent with 1. Figure 4.2 shows that our method of estimating uncertainties is satisfactory.

4.2 Proper Decay Length and Fitting Procedure

The decay length of Λ_b is the distance between secondary vertex (X_B, Y_B) and primary vertex (X_{PV}, Y_{PV}) . Since the Z component of the tracking and vertex information are not well measured in CDF, here we only consider the projection of decay length on the transverse plane and denote it as $L_{xy}(\Lambda_b)$. The primary vertex position comes from either the primary vertex

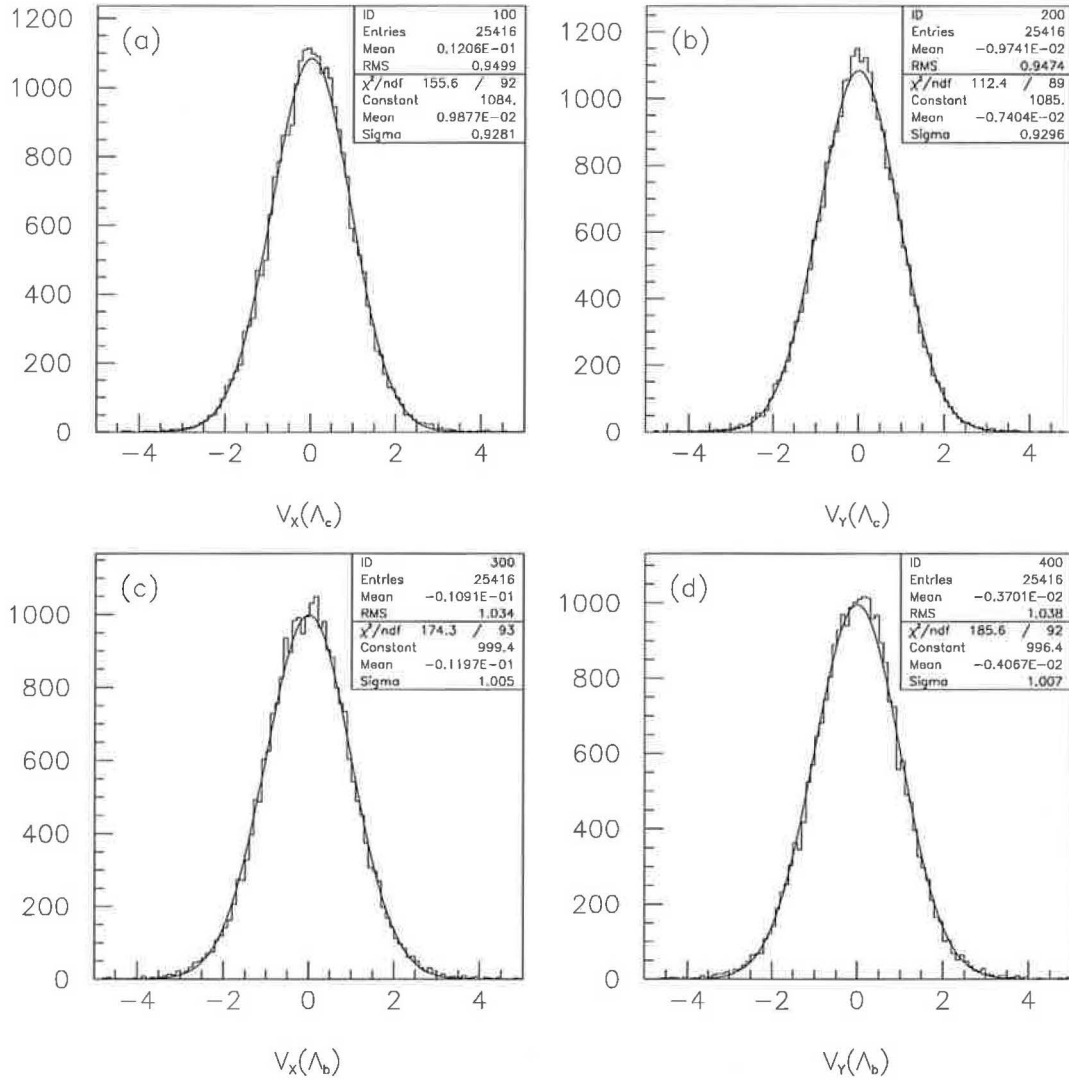


Figure 4.2: Pull distribution test for (a) $V_X(\Lambda_c)$, (b) $V_Y(\Lambda_c)$, (c) $V_X(\Lambda_b)$, and (d) $V_Y(\Lambda_b)$. All the distributions are Gaussian function with mean value at 0 and width(Sigma) of about 1.

reconstruction in an event-by-event basis or the beam position on a run-by-run average. In $p\bar{p}$ collisions, the $b\bar{b}$ are produced as pairs. We detect one of the b quarks through its fragmentation into Λ_b and decay into $\Lambda_c \ell \nu$, while the other b quark will also fragment to a B hadron associated with a displaced secondary vertex. To reconstruct the primary vertex event-by-event we need to use many tracks associated to this event, including the tracks from the underlying event, from the b fragmentation process and B hadron decay. In this case, the secondary vertex from the other b quark will cause a bias in determining the transverse position of the primary vertex. For this reason, we select the run-by-run average beam position to provide the primary vertex position in this analysis.

Prior to the lifetime extraction, the decay length of Λ_b , or $L_{xy}(\Lambda_b)$, has to be transformed into the proper decay length by dividing Lorentz booster factor $\beta\gamma$, as in the following equation,

$$X = \frac{L_{3D}(\Lambda_b)}{\beta\gamma} = \frac{L_{3D}(\Lambda_b) \cdot M(\Lambda_b)}{P(\Lambda_b)} = \frac{L_{xy}(\Lambda_b) \cdot M(\Lambda_b)}{P_T(\Lambda_b)} \quad (4.6)$$

where the proper decay length is denoted as X , and $\beta\gamma = \frac{P(\Lambda_b)}{M(\Lambda_b)}$ is the Lorentz boost factor. $L_{3D}(\Lambda_b)$ is the 3D decay length of Λ_b . X can be expressed in term of 3D quantities $L_{3D}(\Lambda_b)$, $P(\Lambda_b)$, as well as 2D quantities $L_{xy}(\Lambda_b)$, $P_T(\Lambda_b)$. However, since the neutrino in the Λ_b semileptonic decay is not detectable, the 2D quantity $P_T(\Lambda_b)$ is not available. In this situation, the best approximated information we can use is $P_T(\ell\Lambda_c)$. For the correction of this approximation in the lifetime fitting procedure, we define the ratio of $P_T(\ell\Lambda_c)$ to $P_T(\Lambda_b)$ as the *K factor*,

$$K = \frac{P_T(\ell\Lambda_c)}{P_T(\Lambda_b)} \quad (4.7)$$

and we also define a new quantity: pseudo proper decay length X' ,

$$X' = \frac{L_{xy}(\Lambda_b) \cdot M(\Lambda_b)}{P_T(\ell\Lambda_c)} = \frac{X}{K} \quad (4.8)$$

For each event, the decay length $L_{xy}(\Lambda_b)$ is transformed into the pseudo proper decay length X' . We extract the lifetime from the distribution of X' . In the fitting procedure we have to consider the resolution of X' as well, which is transformed from the resolution of $L_{xy}(\Lambda_b)$ in the same way. Since we can not obtain the K factor from real data, in this analysis the K factor distributions are from Monte Carlo simulation. We refer to this distribution as $H(K)$, which is shown in Figure 4.3.

To extract lifetime information from the X' distribution, we have to derive its distribution function in advance. We start the derivation by considering the distribution of the Λ_b proper decay length ($X = KX'$) for pure signal sample, which should be an exponential function with a time constant $c\tau_{\Lambda_b}$, where $c\tau_{\Lambda_b}$ is the lifetime we want to fit from data. Since the measurement of decay vertex is not perfect, what we measured actually is a Gaussian-like smeared result of X' with resolution σ , denoted as x . The lifetime exponential function have to be convoluted with a Gaussian function to account for the smearing effects. The width of this Gaussian function is taken as the resolution of the measured quantity x . In principle the smearing effect is different from event to event. Although we have verified the calculation of Λ_b vertex uncertainty using the pull distribution test for a Monte Carlo sample at the end of section 4.1, in real data there could exist more factors, like the imperfect tracking chamber alignment, which will also contribute to the Λ_b vertex uncertainty. In order to accommodate those extra factors, we put a multiplicative factor s in front of σ , and call it the scale factor. Finally, we have to take into account the K factor correction. Since the K factor distribution $H(K)$ has no obvious relation to the Gaussian smearing effect, we just simply convolute the function with $H(K)$.

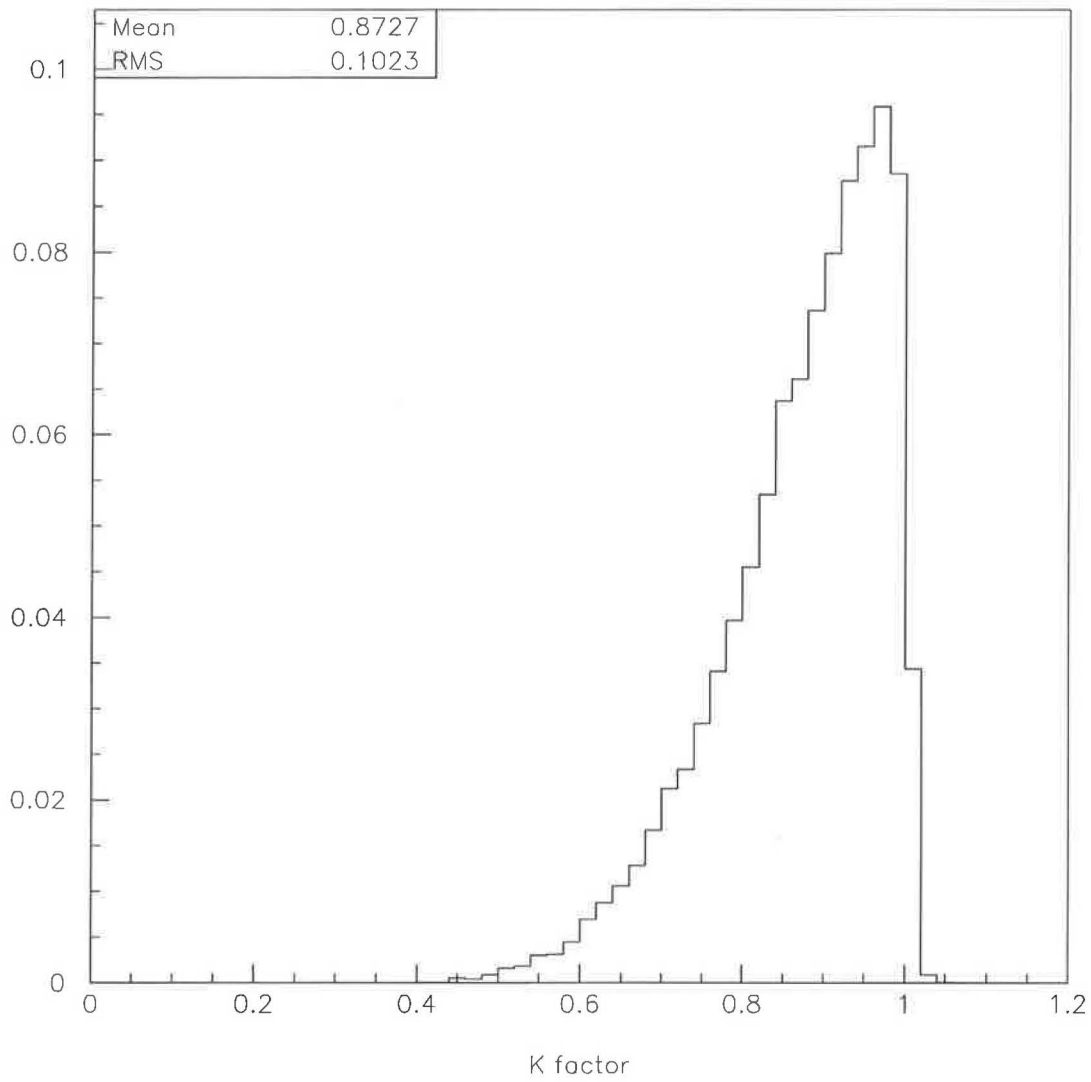


Figure 4.3: K factor distribution from Monte Carlo sample.

The whole function we discussed so far is for pure signal sample only, therefore we call it the signal function F_s , which is shown in equation (4.9),

$$\begin{aligned}
F_s &= \frac{K}{c\tau_{\Lambda_b}} \exp\left(-\frac{KX'}{c\tau_{\Lambda_b}}\right) \otimes G(X' - x, s\sigma) \otimes H(K) \\
&= \sum_K \int dX' \frac{K}{c\tau_{\Lambda_b}} \exp\left(-\frac{KX'}{c\tau_{\Lambda_b}}\right) \cdot \frac{1}{\sqrt{2\pi}s\sigma} \exp\left(-\frac{1}{2}\left(\frac{X' - x}{s\sigma}\right)^2\right) \cdot H(K) \quad (4.9)
\end{aligned}$$

The signal function F_s is supposed to describe the distribution of the measured quantity x for a pure signal sample. However, in real data the distribution is more complex. Although in the invariant mass spectrum of $M(\Lambda 3\pi)$ we can see a peak of signal at Λ_c mass above the background, as shown in Figure 3.21, we cannot distinguish the signal events from the background events among those events underneath the peak area. These peak area events are the mixture of signal events and background events. We need the knowledge of the background function F_b prior to extracting lifetime using the signal function F_s . The events in the side-band of invariant mass $M(\Lambda 3\pi)$ provide a good sample for the modeling of background function F_b . Different components of the F_b are described as follows.

- **The prompt background:** The tracks coming from the primary vertex are called the prompt tracks. A Λ particle coming from the primary vertex combined with 3 prompt tracks is an example of this prompt background. For an event from the prompt background, the vertex we measured in fact is consistent with the primary vertex within the vertex measurement resolution. This background is a zero-lifetime component and can be described by a Gaussian function, as shown in the first item in equation (4.10).

- **The combinatorial background:** The $p\bar{p}$ collision is a high track-multiplicity environment. On average there are about 40 tracks in each events. There is a certain probability that the vertex we detect in fact is just a random combination of tracks, and no physics source is responsible for it. The events from this background are a result of mistake in vertex reconstruction. They will equally populate in the positive and negative side in x . They are described by the second and third terms in equation (4.10).
- **The heavy flavor background:** The high P_T leptons ($P_T > 6 \text{ GeV}/c$) with tighter ID cuts are mostly contributed from B decay, and among them B mesons dominate overwhelmingly. These B mesons also have secondary vertices and can contribute to the background via wrong assignment of track masses. This background component is described by the forth term in equation (4.10).

The complete background function F_b is a summation of the above components with proper fractions as shown below:

$$\begin{aligned}
F_b &= (1 - f_+ - 2f_-) \cdot G(x, s\sigma) && \text{(first item)} \\
&+ \frac{f_-}{\lambda_-} \exp\left(\frac{X'}{\lambda_-}\right) \cdot G(X' - x, s\sigma) && \text{(second item)} \\
&+ \frac{f_-}{\lambda_-} \exp\left(-\frac{X'}{\lambda_-}\right) \cdot G(X' - x, s\sigma) && \text{(third item)} \\
&+ \frac{f_+}{\lambda_+} \exp\left(-\frac{X'}{\lambda_+}\right) \cdot G(X' - x, s\sigma) && \text{(forth item)}
\end{aligned} \tag{4.10}$$

The 4 parameters in the background function F_b are defined as follows,

- λ_- : decay constant for both negative slope exponential function and its reflection in positive x .

- f_- : fraction of negative slope exponential function
- λ_+ : decay constant for positive slope exponential function
- f_+ : fraction of positive slope exponential function

The total function to describe the distribution of the measured quantity x for the events in the peak area is a linear combination of F_s and F_b , i.e.,

$$F = (1 - f_b)F_s + f_bF_b \quad (4.11)$$

where f_b is the background fraction for the events in the peak area, determined from the fitting for the invariant mass spectrum of $M(\Lambda 3\pi)$.

The total function F have six parameters, namely, $c\tau_{\Lambda_b}$, s , λ_- , f_- , λ_+ , and f_+ . For a specific set of parameters, the function F gives the probability for an event to have the measured pseudo proper decay length x and its resolution σ . To extract the best parameters from the data, we first calculate the probability of each event according to the measured x and σ , then we take the product of the probability for each event in peak area, as shown in equation (4.12),

$$L = \prod_{i=1}^{N_s} F(x_i, \sigma_i) \quad (4.12)$$

where N_s is the number of event in peak area, L is called the likelihood function. The fitting procedure in essence is to maximize L . This fitting method is known as Maximum Likelihood method. From the point view of computational algorithm, to take the summation of a quantity associated with the events is more accurate and reliable than taking the product. Therefore,

rather than maximizing L , we minimize the negative log-likelihood function $-\ln L$ in the fitting procedure, where

$$-\ln L = -\sum_{i=1}^{N_s} \ln F. \quad (4.13)$$

So far everything is ready to extract a best set of fitting parameters, except that the background function parameters λ_- , f_- , λ_+ , and f_+ will have to be extracted from the peak area events. The variation of these parameters could have significant effects on the lifetime fitting parameter, $c\tau(\Lambda_b)$. In order to stabilize the lifetime fitting, we need extra constraints on the background function parameters. As we mentioned before, the side-band area events are good modeling sample for the background events in the peak area. Because they have the similar kinematical and topological (like vertex, L_{xy} ...) properties. Therefore we introduce an extra component of negative log-likelihood function based on the F_b and the side-band area events, as shown in equation(4.14)

$$-\ln L = -\sum_{i=1}^{N_s} \ln F - \sum_{i=1}^{N_b} \ln F_b \quad (4.14)$$

where N_b is the number of events in side-band areas. With the extra component of negative log-likelihood function, the background function parameters λ_- , f_- , λ_+ , f_+ are constrained by the side-band area events. The lifetime fitting result will be closer to the true property of the signal events in the peak area.

We use a fitting package MINUIT [63] developed by CERN to accomplish this fitting task.

In the fitting, at the beginning we provide a set of initial values for each fitting parameter. The fitting program will calculate the function $-\ln F$ for each event in the peak area and the function $-\ln F_b$ for each event in the side-band area, and take the sum for all of them. By varying each fitting parameter to minimize the function value, the fitting program will eventually converge on the best fitted parameters. The fitting results are shown in Table 4.1.

$c\tau$ (μm)	407_{-154}^{+116}
s	1.67 ± 0.14
f_-	0.08 ± 0.02
λ_- (μm)	511 ± 156
f_+	0.45 ± 0.05
λ_+ (μm)	461 ± 81

Table 4.1: Fitting parameters.

The fitted lifetime of Λ_b is 407_{-154}^{+116} μm in this analysis. The fitted background function for the side-band area events is shown in Figure 4.4. The fitted function for the peak area events is shown in Figure 4.5, where the signal function is shown in shaded area. In Figure 4.6, we also show the negative log-likelihood as a function of fitted $c\tau_{\Lambda_b}$.

4.3 Systematic Error

In the lifetime analysis, we don't want the fitted lifetime result to have significant dependence on the event selection cuts, the lifetime fitting procedure, the background sample selection and the K factor distribution. In this section we will check the systematic uncertainties from these sources.

First we apply identical method to extract Λ_b lifetime from several high statistics Monte Carlo samples with input lifetime of 360 μm , 380 μm , 400 μm , 420 μm , and 440 μm . The fitted

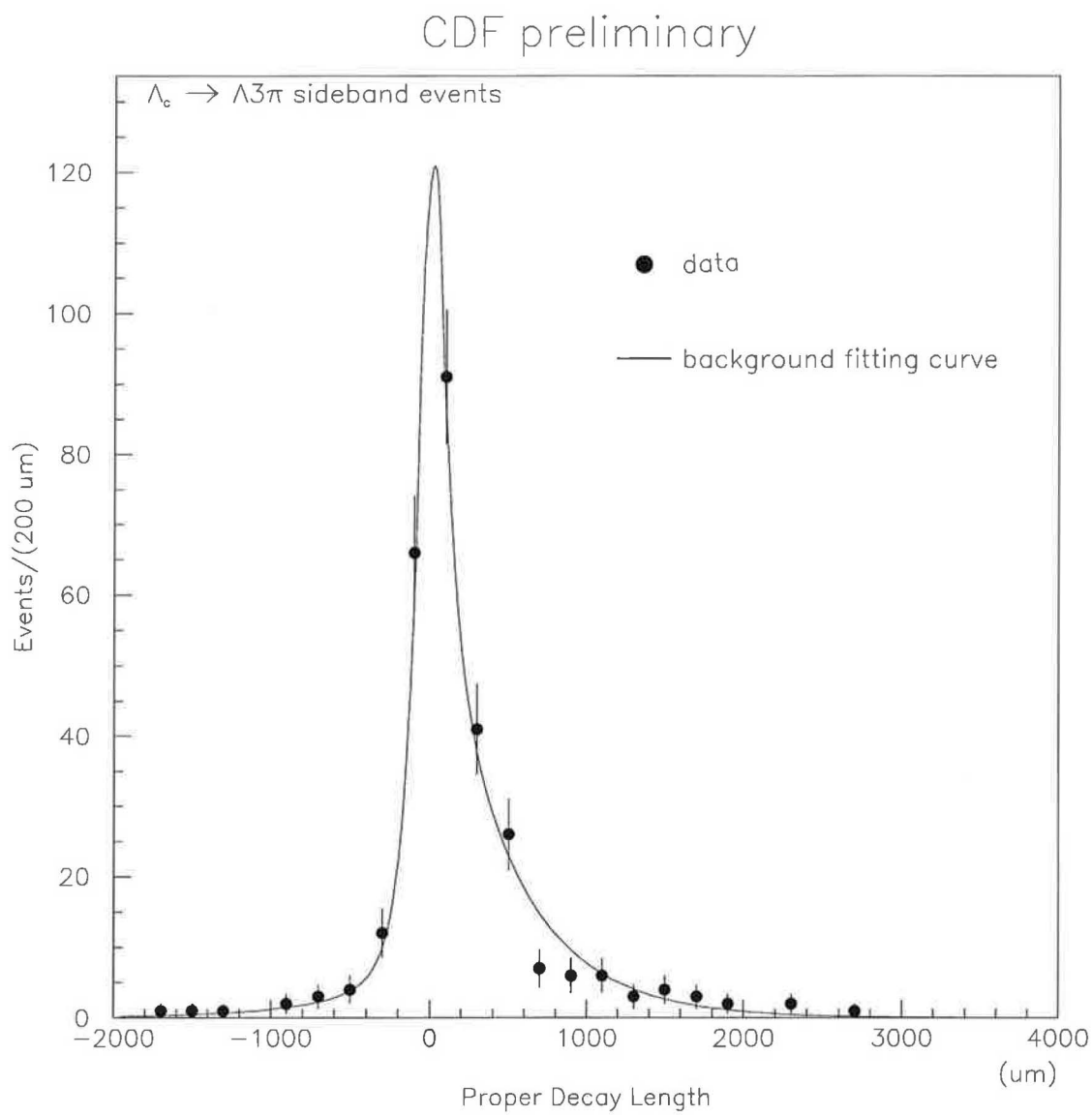


Figure 4.4: Pseudo proper decay length of Λ_b for side-band area events.

CDF preliminary

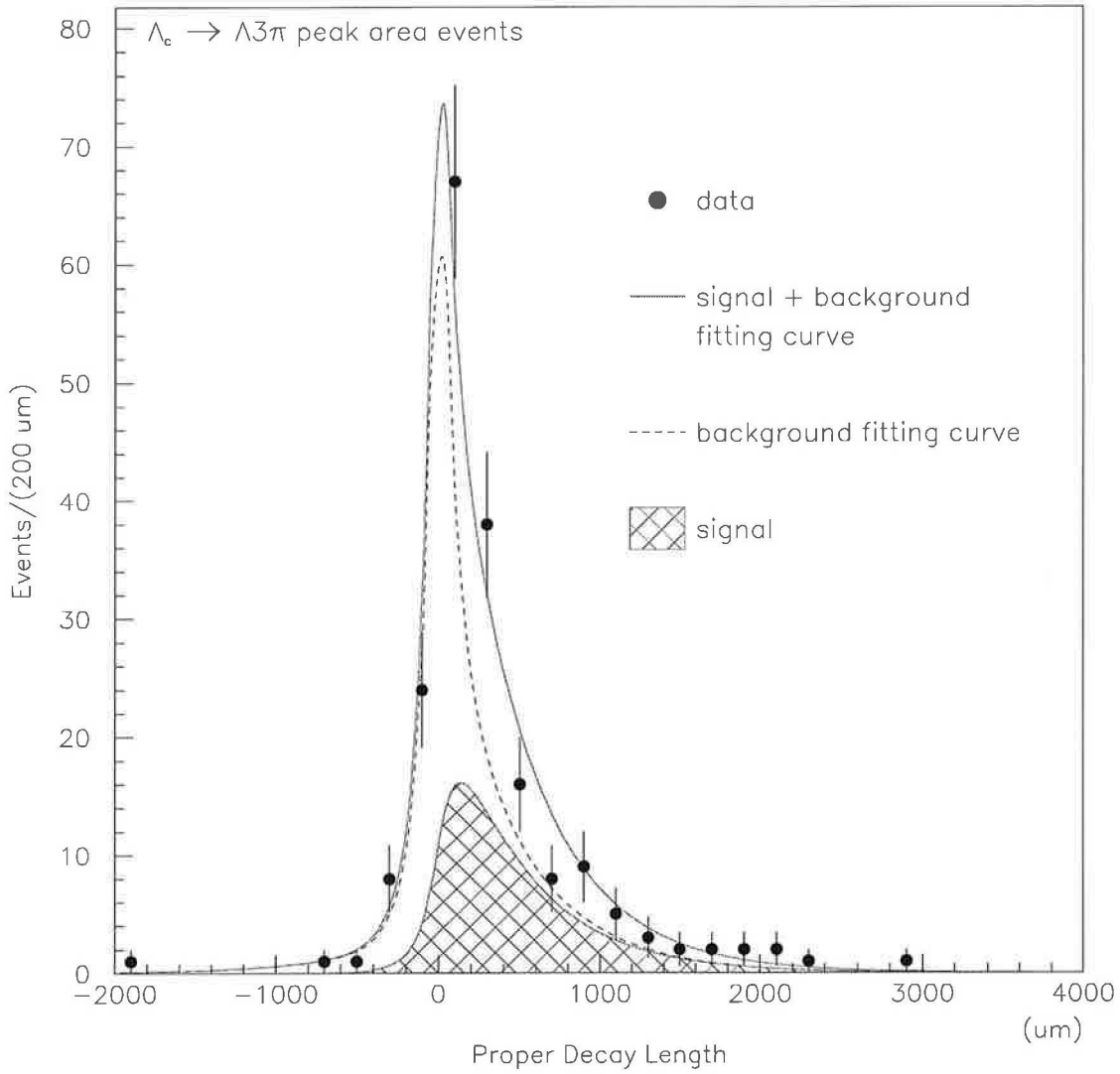


Figure 4.5: Pseudo proper decay length of Λ_b for peak area events.

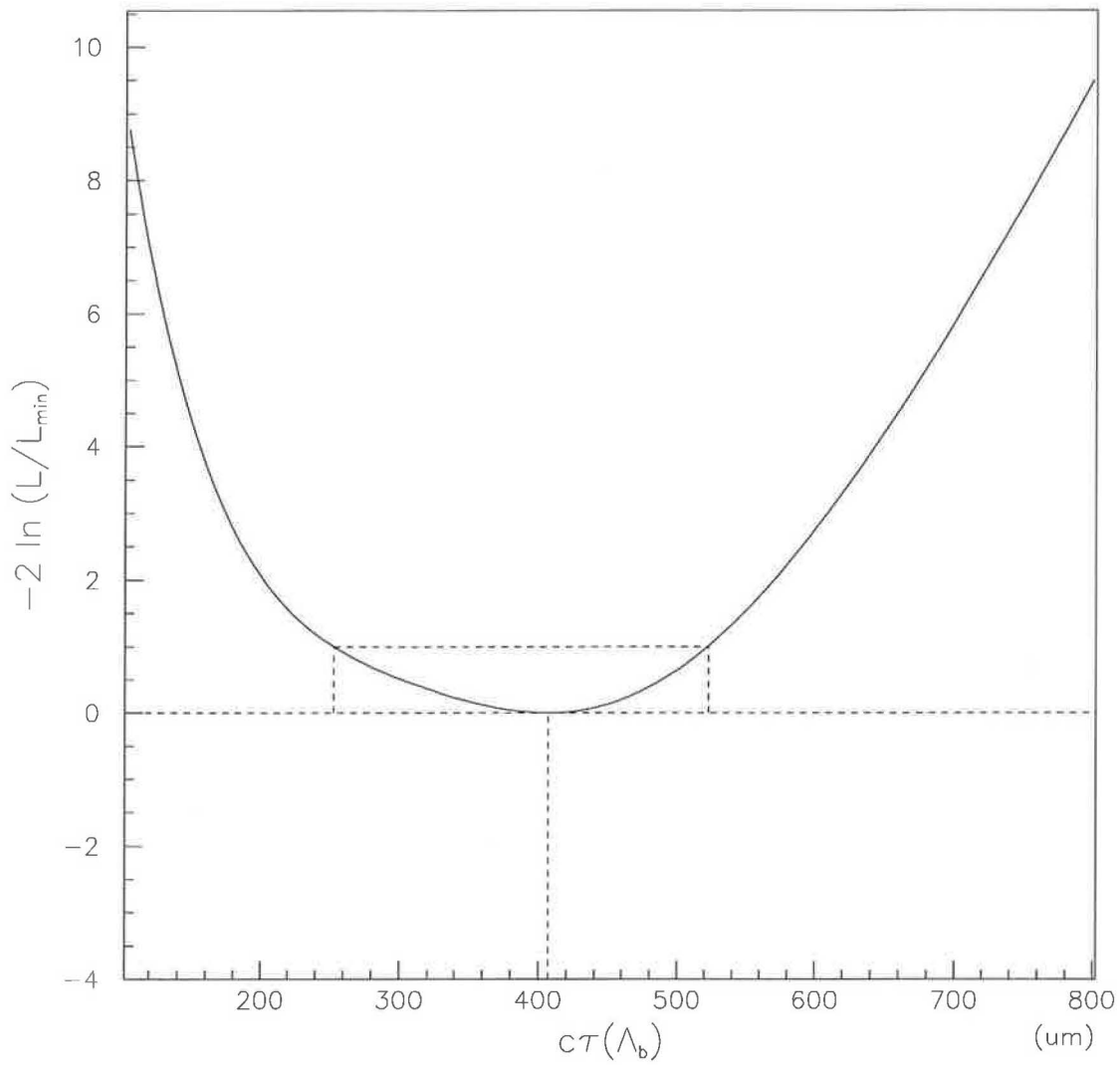


Figure 4.6: The change in $-2 \ln L$ from its minimum as a function of $c\tau_{\Lambda_b}$.

results have a shift of $15 \mu\text{m}$, as shown in Figure 4.7. This shift is attributed to the effect of event selection cuts. The cut $L_{xy}(\Lambda_c)/\sigma > 1$, among several other cuts, is the major reason of this shift. By changing this cut to $L_{xy}(\Lambda_c)/\sigma > 0$, we have seen a shift of $6 \mu\text{m}$.

The fitting procedure used in section 4.2 is called the one-step fitting, in which all the parameters are fitted simultaneously. Here we use a two-step fitting to estimate the uncertainty induced from the fitting procedure. In the first step, we use side-band area events to extract the background function parameters and fix them. In the second step, we use the total function F to fit the peak area events, leaving only the $c\tau(\Lambda_b)$ as free parameter. The result from this two-step fitting is $396 \pm 91 \mu\text{m}$. We quote $11 \mu\text{m}$ as the systematic error from the fitting procedure.

Ideally there is no need to restrict the range of the measured quantity x in a fitting ². However, the background events have a certain probability to populate at the long tail of $c\tau^*$ in both positive and negative directions. We try two restricted ranges, $-0.2 < c\tau^* < 0.4 \text{ cm}$ and $-0.6 < c\tau^* < 1.2 \text{ cm}$. We expect that only the combinatorial background will be affected. The fitting parameters for different $c\tau^*$ restricted ranges and different fitting procedures are shown in 4.2. Figure 4.8 and Figure 4.9 show the curves of fitting function. Clearly only the shape of the long positive and negative tails are changed. In this analysis we select the restricted range of $-0.2 < c\tau^* < 0.4 \text{ cm}$.

The background fraction f_b is obtained from the mass fitting of the invariant mass of $M(\Lambda 3\pi)$. We vary it by one standard deviation and re-fit the lifetime. The result is changed by ${}_{-25}^{+21} \mu\text{m}$. We quote it as the systematic error for the background normalization. We also change the scale factor s from 1 to 2, which changes the fitting result by ${}_{-20}^{+2} \mu\text{m}$. The side-band area events we use as background sample are in the range of $2.200 \pm 0.020 \text{ GeV}/c^2$ and $2.370 \pm$

²For a brief meaning in the following discussion, we denote x as $c\tau^*$ from now on.

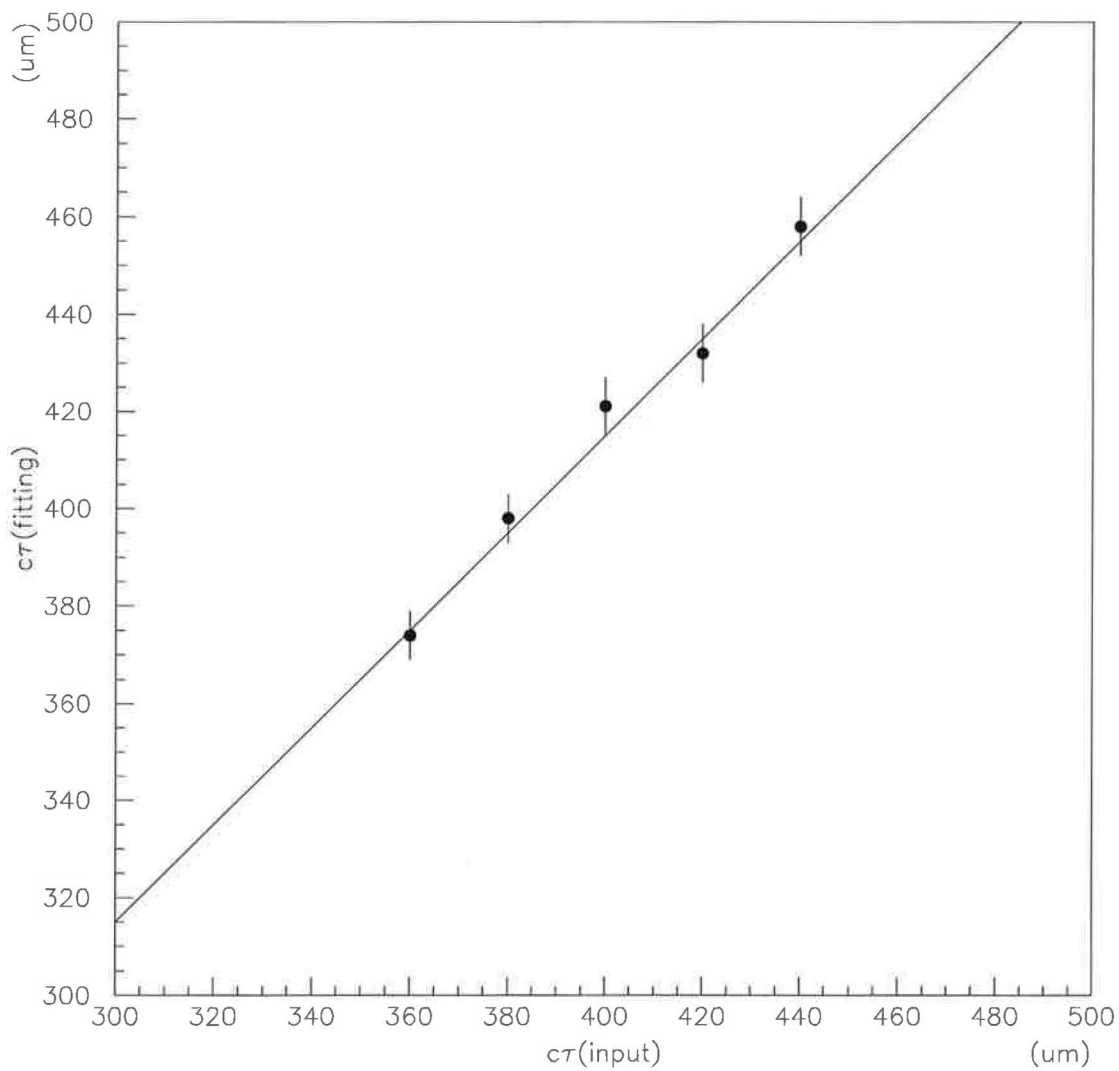


Figure 4.7: The comparison between input $c\tau$ and fitted $c\tau$ for 5 high statistics Monte Carlo samples. There is a shift of $15 \mu\text{m}$ in the lifetime fitting result. It's attributed to the systematic error for event selection cuts.

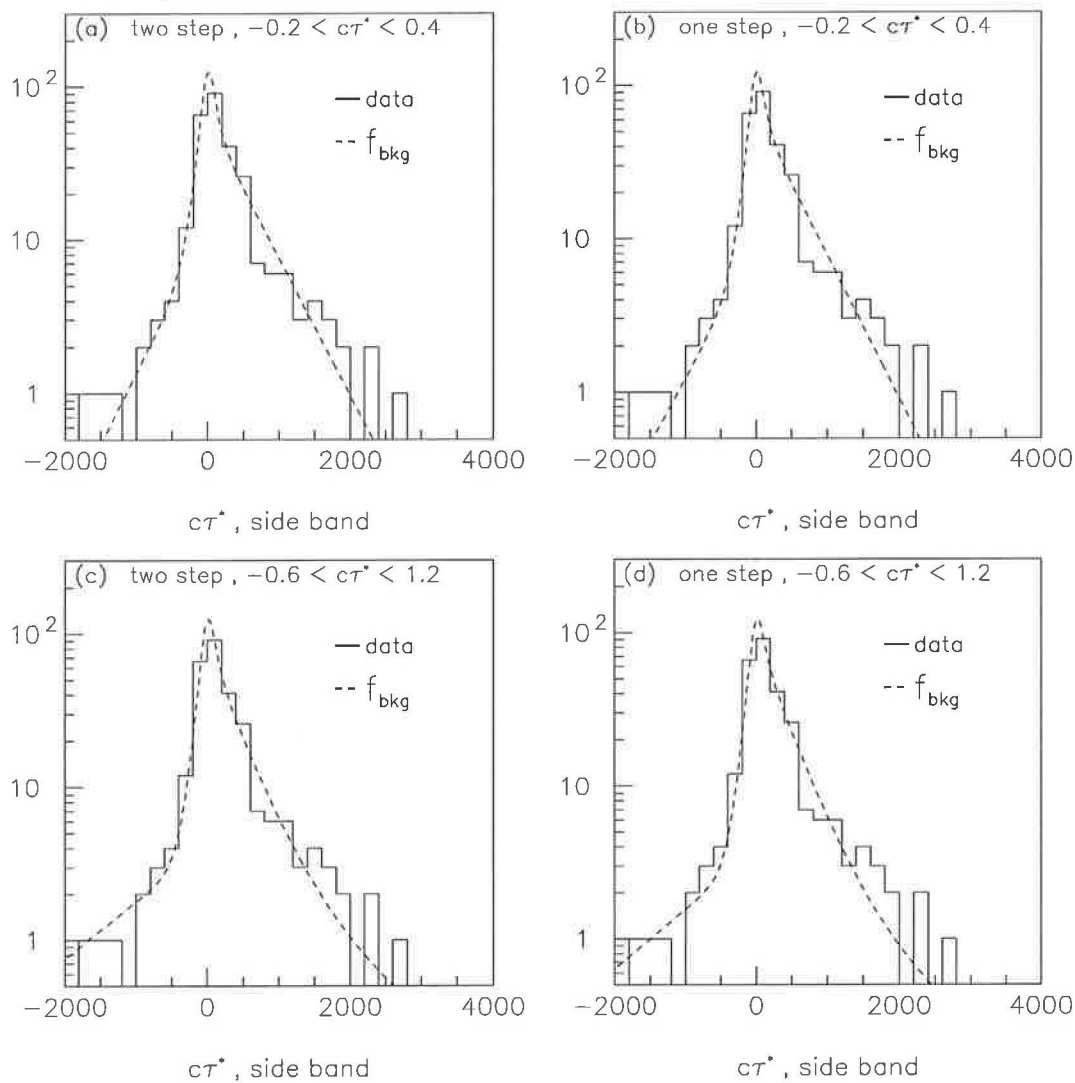


Figure 4.8: Background function(F_b) fitting for side-band area events with two different fitting procedure and two different restricted ranges of $c\tau^*$.

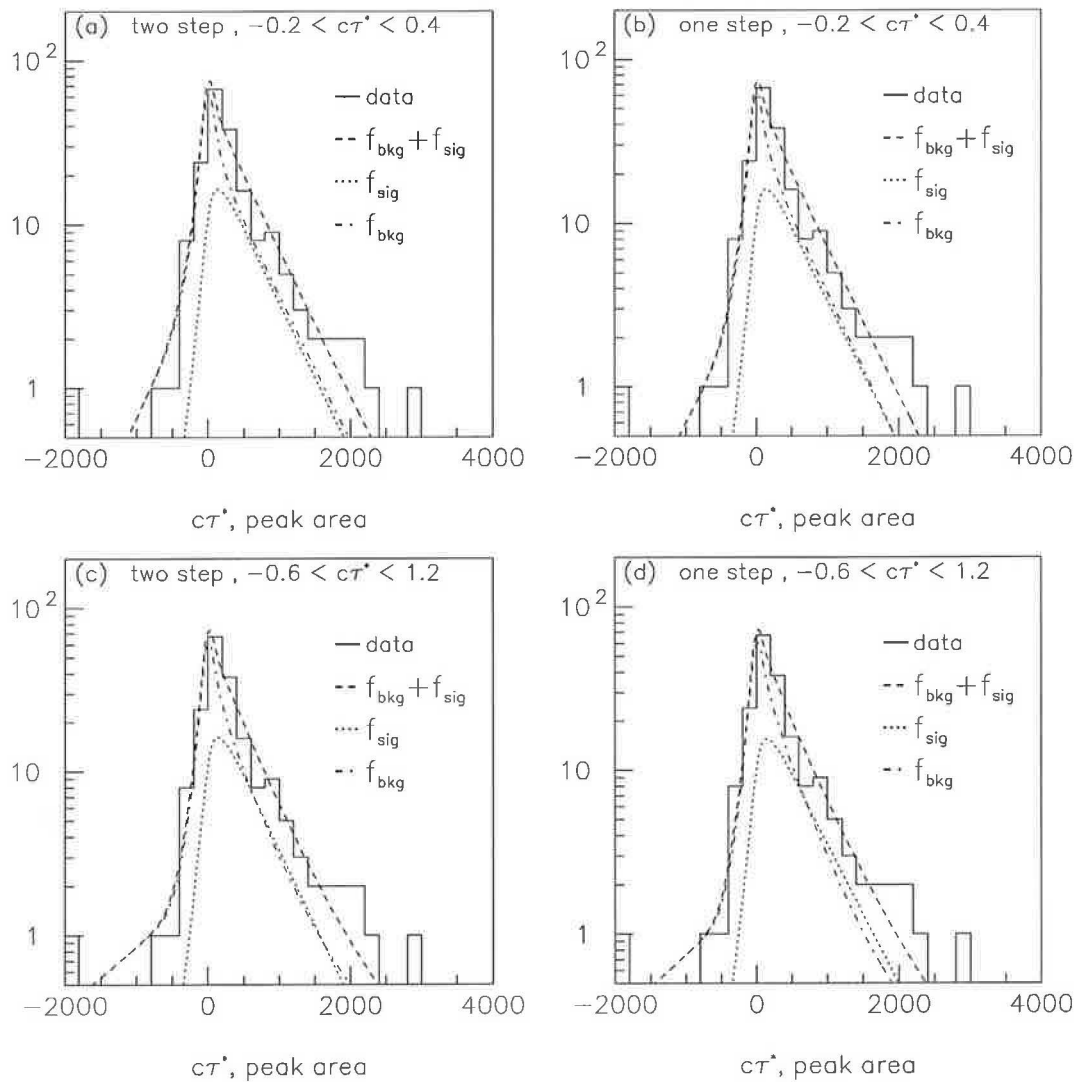


Figure 4.9: Total function(F) fitting for peak area events with two different fitting procedure and two different restricted ranges of $c\tau^*$.

fitting procedure	two steps		one steps	
$c\tau$ range(cm)	-0.2 ~ 0.4	-0.6 ~ 1.2	-0.2 ~ 0.4	-0.6 ~ 1.2
$c\tau$	396 ± 91	395 ± 88	407 ± 124	423 ± 104
s	1.69 ± 0.16	1.74 ± 0.16	1.67 ± 0.14	1.73 ± 0.13
f_-	0.09 ± 0.03	0.08 ± 0.02	0.08 ± 0.02	0.07 ± 0.02
λ_-	469 ± 145	1162 ± 210	511 ± 156	1120 ± 185
f_+	0.40 ± 0.05	0.42 ± 0.05	0.45 ± 0.05	0.47 ± 0.05
λ_+	489 ± 73	364 ± 69	461 ± 81	349 ± 67

Table 4.2: Fitting parameters for two different fitting procedure and two different restricted range of $c\tau^*$.

0.020 GeV/c² on the $M(\Lambda 3\pi)$ spectrum. To select a different background sample, we change the range to 2.230 ± 0.020 GeV/c² and 2.340 ± 0.020 GeV/c². The resulting lifetime variation is $^{+49}_{-51}$ μm .

The K factor distribution is obtained from Monte Carlo sample. This is the only place where the lifetime fitting result has a dependence on the Monte Carlo sample. We produce several Monte Carlo samples with different conditions to estimate the systematic bias. We change the input lifetime for each Monte Carlo sample from 360 μm to 460 μm , and find that the uncertainty is ± 1 μm . The Peterson fragmentation function parameter ϵ_b was measured to be $0.006 \pm 0.001 \pm 0.002$ [28] for B mesons in e^+e^- collision. For the B baryon Λ_b this value could be different. We change it from 0.002 to 0.05, the variation for the fitted lifetime is $^{+4}_{-1}$ μm . The uncertainty from the parton distribution function (PDF) is also tested, although the effect is supposed to be small because that the K factor is a ratio between two kinematical variables: $P_T(\ell\Lambda_c)$ and $P_T(\Lambda_b)$. We use two different sets of PDF: MRSD0 and MRSD- [23, 24]. The result is changed by ± 1 μm .

The summary of systematic errors are listed in Table 4.3. Adding these errors in quadrature,

Sources	$\Delta c\tau_{\Lambda_b}$ (μm)
event selection cuts	+15
lifetime fitting procedure	± 11
background normalization(f_b)	$^{+21}_{-25}$
scale factor(s)	$^{+2}_{-20}$
background sample selection	$^{+49}_{-51}$
K factor with different input $c\tau$	± 1
K factor with different ϵ_b	$^{+4}_{-1}$
K factor with different PDF	± 1
Total	$^{+57}_{-60}$

Table 4.3: Summary of systematic errors.

the total systematic error is $^{+57}_{-60} \mu\text{m}$.

Chapter 5

Conclusion and Future Prospects

The heavy quark effective theory (HQET) provides a systematic method to exploit the properties of B hadrons. It gives good predictions for the B hadron spectroscopy and the B meson lifetimes. The discrepancy of Λ_b lifetime between the predicted value and the measured value is a challenge to the concept of quark-hadron duality which is the foundation of HQET. This " Λ_b lifetime puzzle " is a crucial issue for the understanding of heavy hadron structure. It needs more measurements to address this problem.

In this thesis we attempt to measure the Λ_b lifetime using the decay channel $\Lambda_b \rightarrow \Lambda_c^+ e^- \bar{\nu}$, where $\Lambda_c^+ \rightarrow \Lambda \pi^+ \pi^+ \pi^-$. We have observed 57 ± 12 events from the inclusive electron data collected at CDF Run 1. The corresponding integrated luminosity is about 110 pb^{-1} . The lifetime of Λ_b is measured to be:

$$c\tau_{\Lambda_b} = 407_{-154}^{+116}(\text{stat.})_{-60}^{+57}(\text{syst.}) \mu\text{m}$$

or

$$\tau_{\Lambda_b} = 1.36_{-0.51}^{+0.39}(\text{stat.})_{-0.20}^{+0.19}(\text{syst.}) \text{ ps}$$

The uncertainty of this measurement is still dominated by the statistics. In the previous

CDF Λ_b lifetime measurement from the channel $\Lambda_c^+ \rightarrow p K^- \pi^+$, 197 ± 25 signal events were used in lifetime fitting, and the statistical uncertainty is $45 \mu\text{m}$. For the Run 1 data, we hope to get more signal events from the channel $\Lambda_c^+ \rightarrow p K_s^0$ as well as from the inclusive muon sample. The total number of signal events, including the results in the $p K^- \pi^+$ channel and in this thesis, is expected to be about 400, and the statistical uncertainty can be reduced to $31 \mu\text{m}$.

In Run 2, the total integrated luminosity is expected to be 2 fb^{-1} , which is 20 times higher than Run 1. The coverage of silicon detector will be increased by a factor of 2. In total, there will be at least 40 times of signal events at Run 2. In addition, several important detector upgrades can also improve the B events identification significantly, including the ISL (Intermediate Silicon Layer) which extends the silicon layer to $R=28 \text{ cm}$ and enable the stand-alone tracking, the Layer00 which is silicon sensors mounted on the surface of beam pipe and can improve the impact parameter resolution, and the TOF (Time Of Flight) detector which provides the particle ID for the $K-\pi$ separation. All these new features in Run 2 are helpful to increase the efficiency of B events reconstruction.

Furthermore, with the high statistics data in Run 2, the Λ_b fully reconstructed channel $\Lambda_b \rightarrow J/\psi \Lambda$ will also play an important role in Λ_b lifetime measurement.

Appendix A

Purification of the Λ Sample

In the Λ reconstruction, two tracks with opposite charges are selected and the track with higher P_T is assigned with p mass. Without an effective proton identification method, the proton candidate being selected could be other particle species. Most of the time, the wrong proton candidate is π . In a sample of Λ candidates, if we assign π mass to the p candidates, a peak at K_s^0 mass will appear. This is called the K_s^0 reflection background. Figure A.1 shows both the Λ and its K_s^0 reflection spectrum for a Λ sample.

At CDF the energy loss information collected by CTC can be used for particle identification [64]. The energy loss per unit length, or dE/dX , is a function of $\beta\gamma$ which is equal to P/M , where P and M are momentum and mass of a particle. A particle can be identified through the measurement of its dE/dX and P . The energy deposition for each hit in CTC is related to the area of the ionization pulse, which is converted to a TDC output width, and is counted in unit of ns. The outer 54 wires are used to give a 80% truncated mean of energy loss, denoted as QCTC, for each track. The number of measurements used in calculating the average, denoted as NCTC, is also available in offline stage. The plot of QCTC as function of momentum P for the 5 particle species: e , μ , π , K and p is shown in Figure A.2. The predicted curves depends on the performance of the gas in CTC, they varies from Run 1A to Run 1B. The curves shown

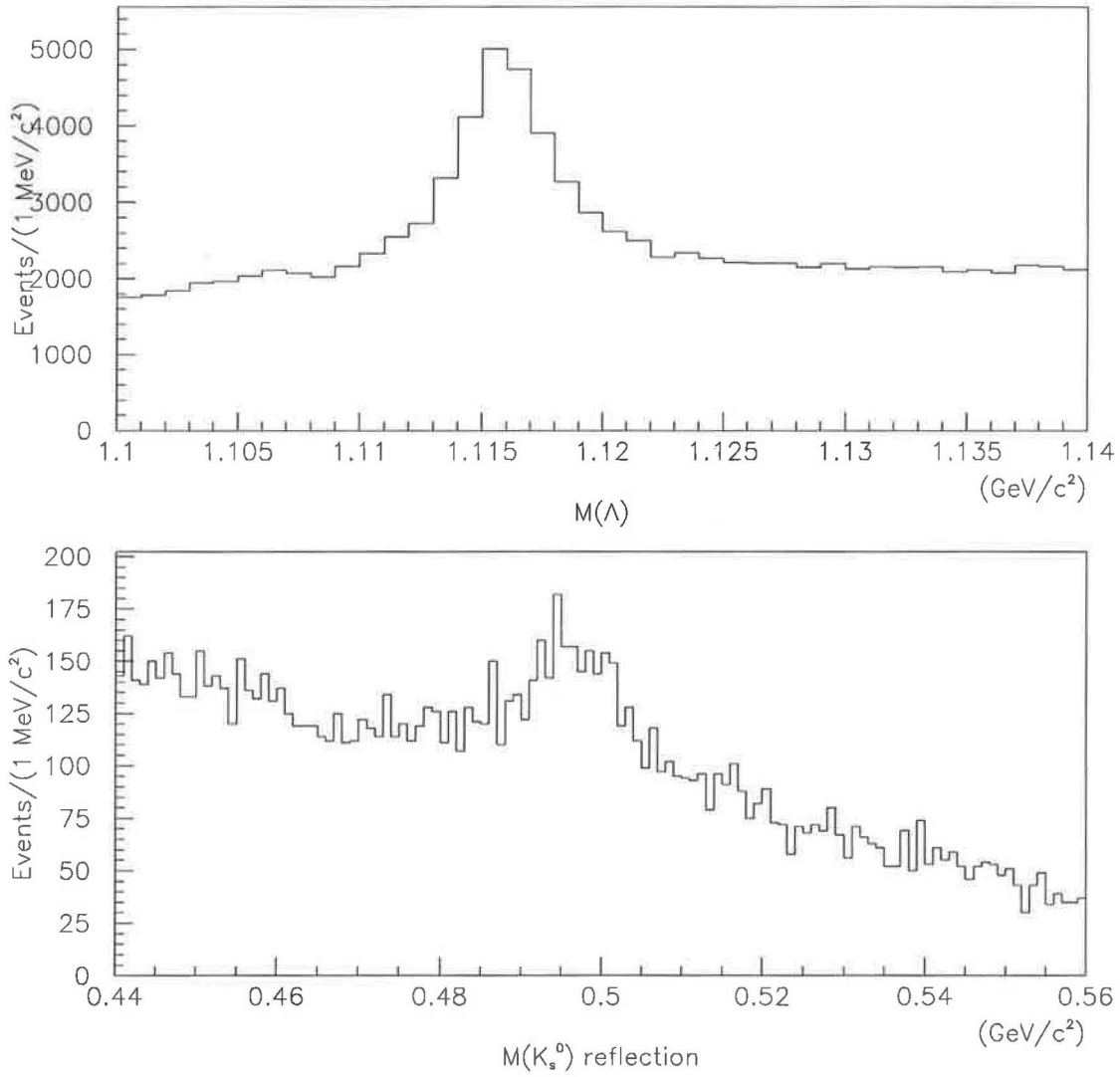


Figure A.1: Λ and its K_s^0 reflection spectrum for a Λ sample.

in this plot are typical for Run 1B.

A track of unknown specie is tested with 5 hypotheses of e , μ , π , K and p via a normalized Δ QCTC defined as in equation (A.1),

$$\Delta QCTC = \frac{QCTC^{MEA} - QCTC_i^{PRE}}{\sigma_{QCTC}} \quad (\text{A.1})$$

where $QCTC^{MEA}$ is the measured QCTC, and $QCTC_i^{PRE}$ is the predicted value of QCTC based on the hypothesis of specie i , where i can be e , μ , π , K or p . σ_{QCTC} is the uncertainty of $QCTC^{MEA}$. The normalized QCTC should have a Gaussian distribution centered at 0 with width of 1 if the hypothesis is correct. We take the p candidate in a Λ sample as an example to illustrate this point. For a better signal to background ratio, we require the impact parameter of p and π to be greater than 3σ . The Λ signal is shown in Figure A.3. We use the side-band as a model of proton background. The normalized QCTC of p candidates from peak area and side-band with p hypothesis is shown in Figure A.4. With side-band subtraction, the distribution appears to be a Gaussian distribution with $\sigma = 1$, as what we expected.

The probability that a track is consistent with the particle i hypothesis can be derived from the normalized Δ QCTC as follows.

$$\begin{aligned} Prob(i) &= \frac{1}{\sigma_{QCTC}\sqrt{2\pi}} \cdot \exp\left(-\frac{1}{2}\left(\frac{QCTC^{MEA} - QCTC_i^{PRE}}{\sigma_{QCTC}}\right)^2\right) \\ &= \frac{1}{\sigma_{QCTC}\sqrt{2\pi}} \cdot \exp\left(-\frac{1}{2}(\Delta QCTC)^2\right) \end{aligned} \quad (\text{A.2})$$

We define a proton identification confidence level based on these probabilities, as shown in equation (A.3),

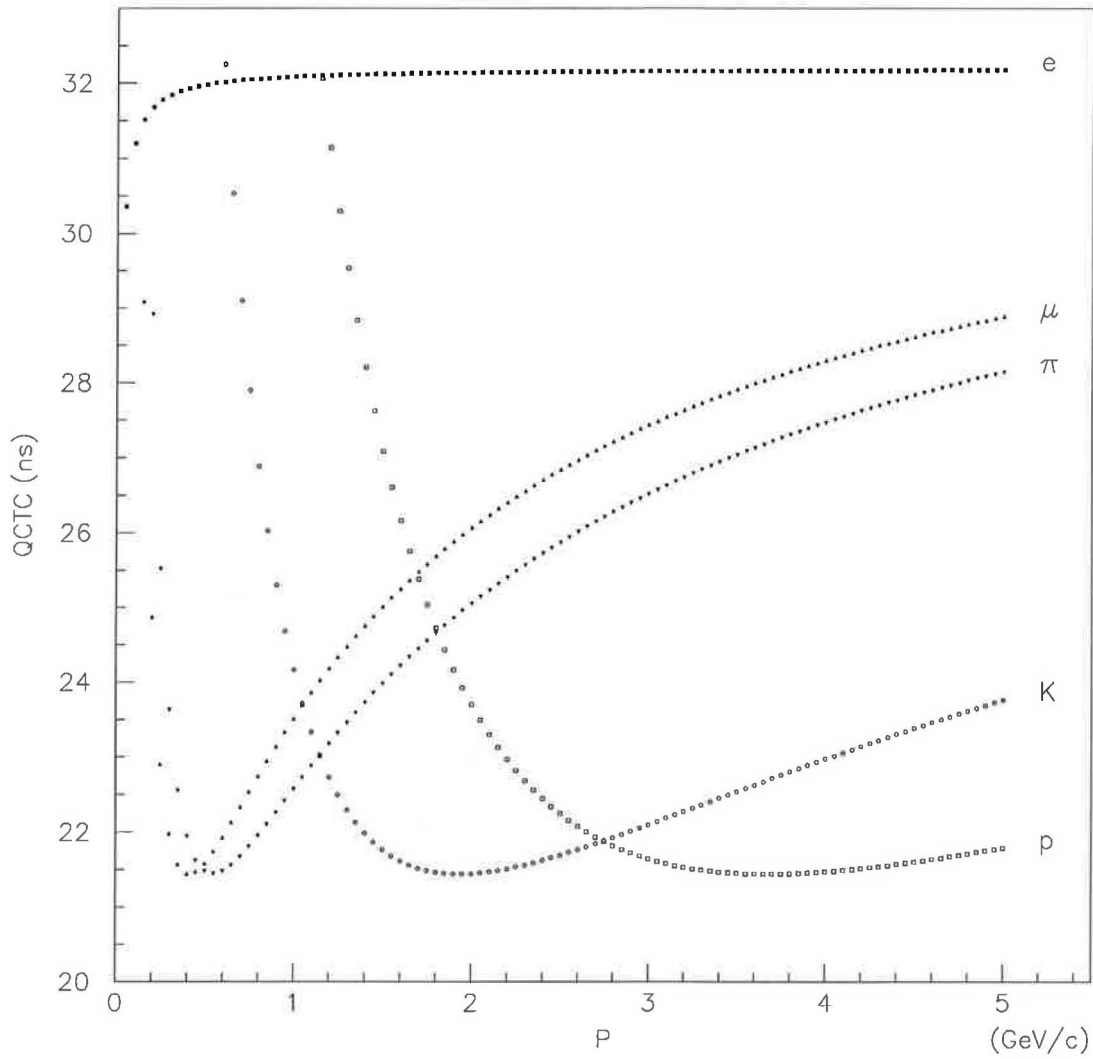


Figure A.2: A typical relation between QCTC and particle momentum for e , μ , π , K and p .

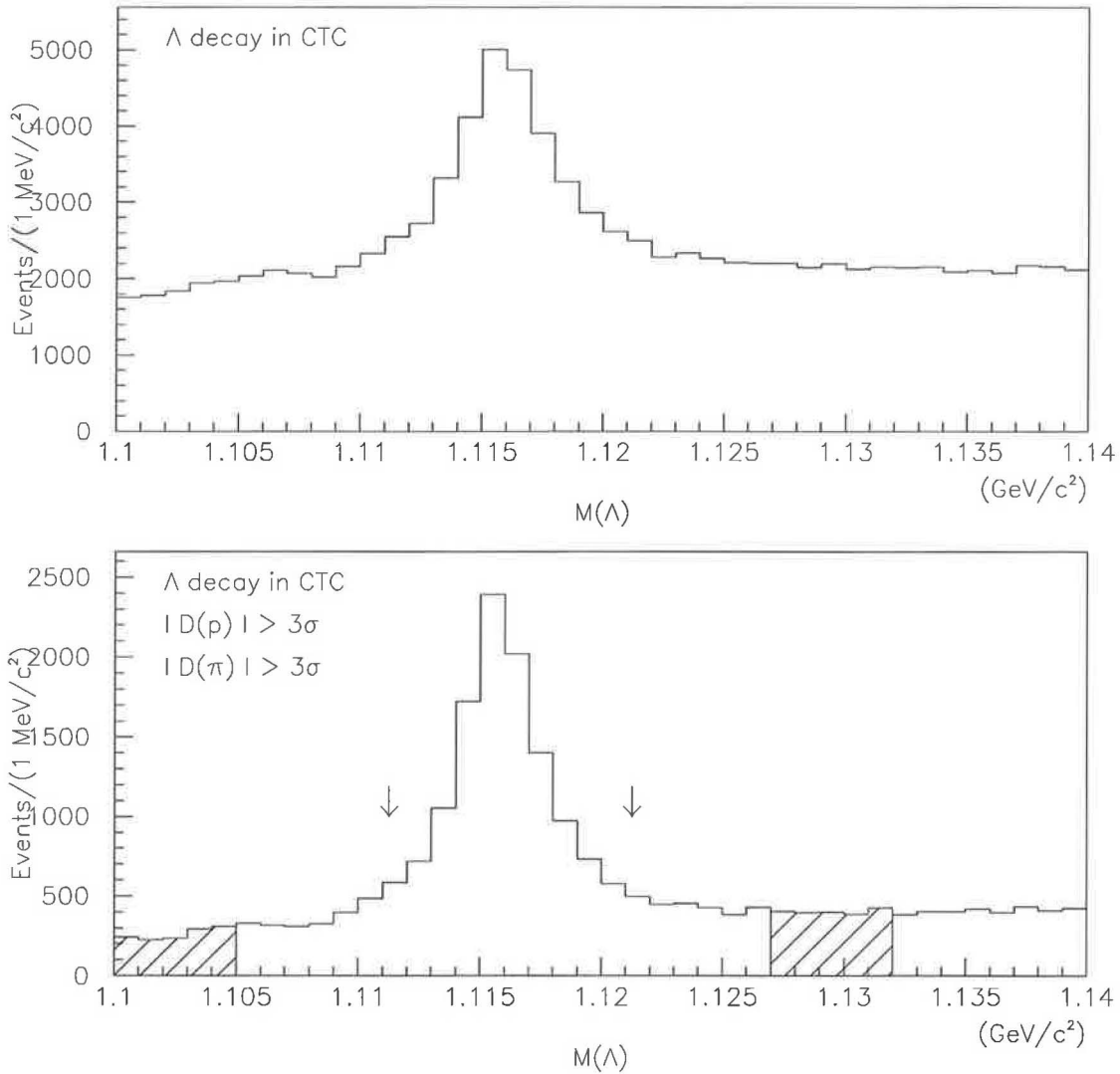


Figure A.3: (upper) The Λ sample we use to study the dE/dX property of proton. (lower) After applying the cuts $|D| > 3\sigma$ for p and π tracks, the signal to background ratio becomes better.

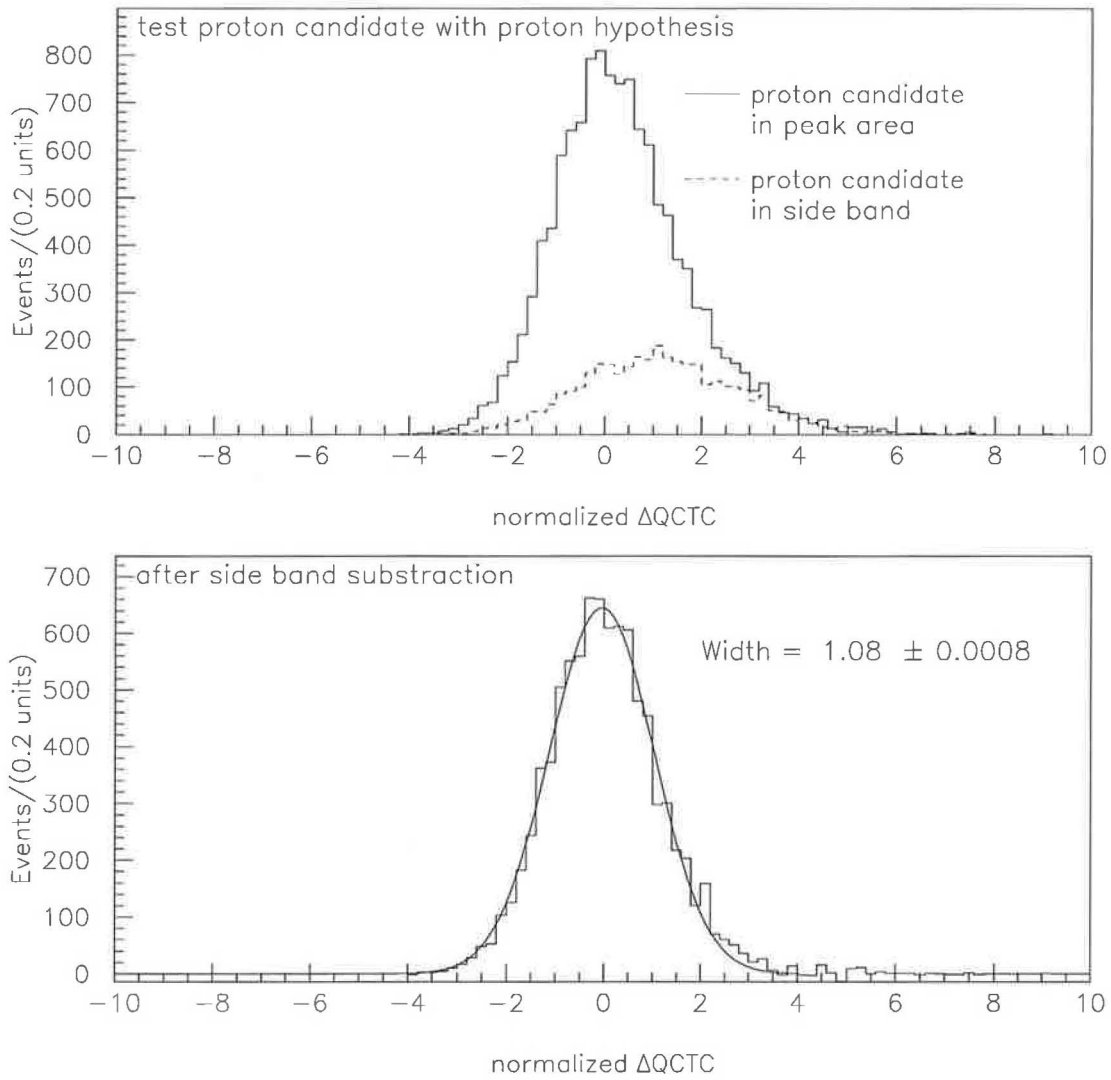


Figure A.4: (upper) The normalized $\Delta QCTC$ for the p candidates in the peak area of $M(\Lambda)$ (solid line) and in the side-band (dash line). (lower) After side-band subtraction, the normalized $\Delta QCTC$ for the p candidates become a good Gaussian distribution.

$$Level(p) = \frac{Prob(p) + Prob(K)}{Prob(p) + Prob(\pi) + Prob(K) + Prob(e)} \quad (A.3)$$

For a pure sample of p candidate, the $level(p)$ will peak around 1, otherwise it will peak around 0. The $level(p)$ distribution for p candidates from the peak area and side-band is shown in Figure A.5. In order to reject the background and keep most of the signal, in this analysis we require $level(p) > 0.2$.

With better proton identification, the fraction of K_s^0 reflection should be reduced for a Λ sample. Therefore we use the K_s^0 reflection spectrum as a monitor to survey the effect of the $level(p)$ cut. To magnify this effect, we use a tighter cut: $level(p) > 0.6$. The Λ and K_s^0 reflection with and without $level(p)$ cut are shown in Figure A.6. Clearly we see that K_s^0 reflection background is reduced significantly by the cut: $level(p) > 0.6$.

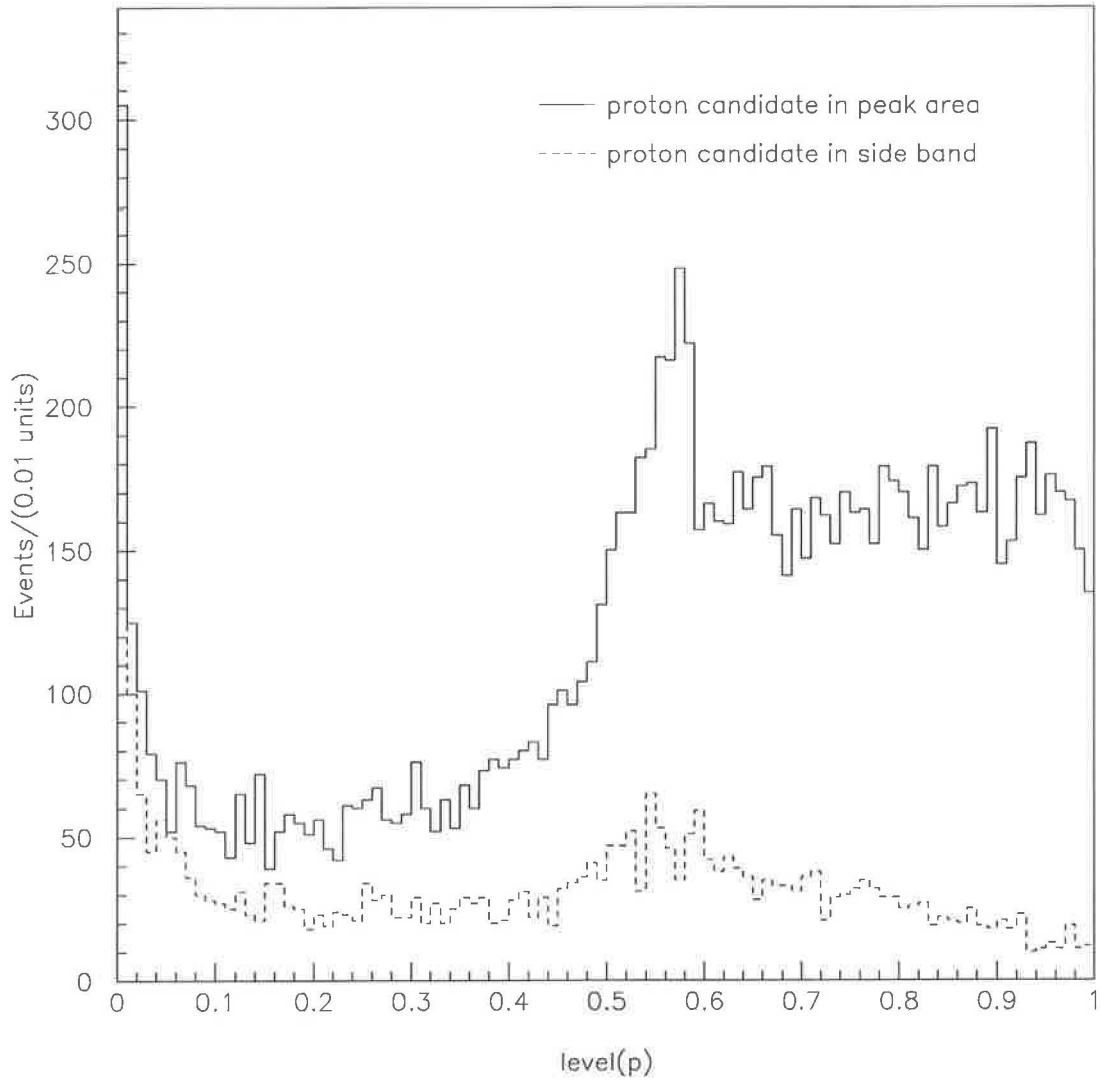


Figure A.5: The distribution of $\text{level}(p)$ for proton in peak area (solid) and in side-band area (dash).

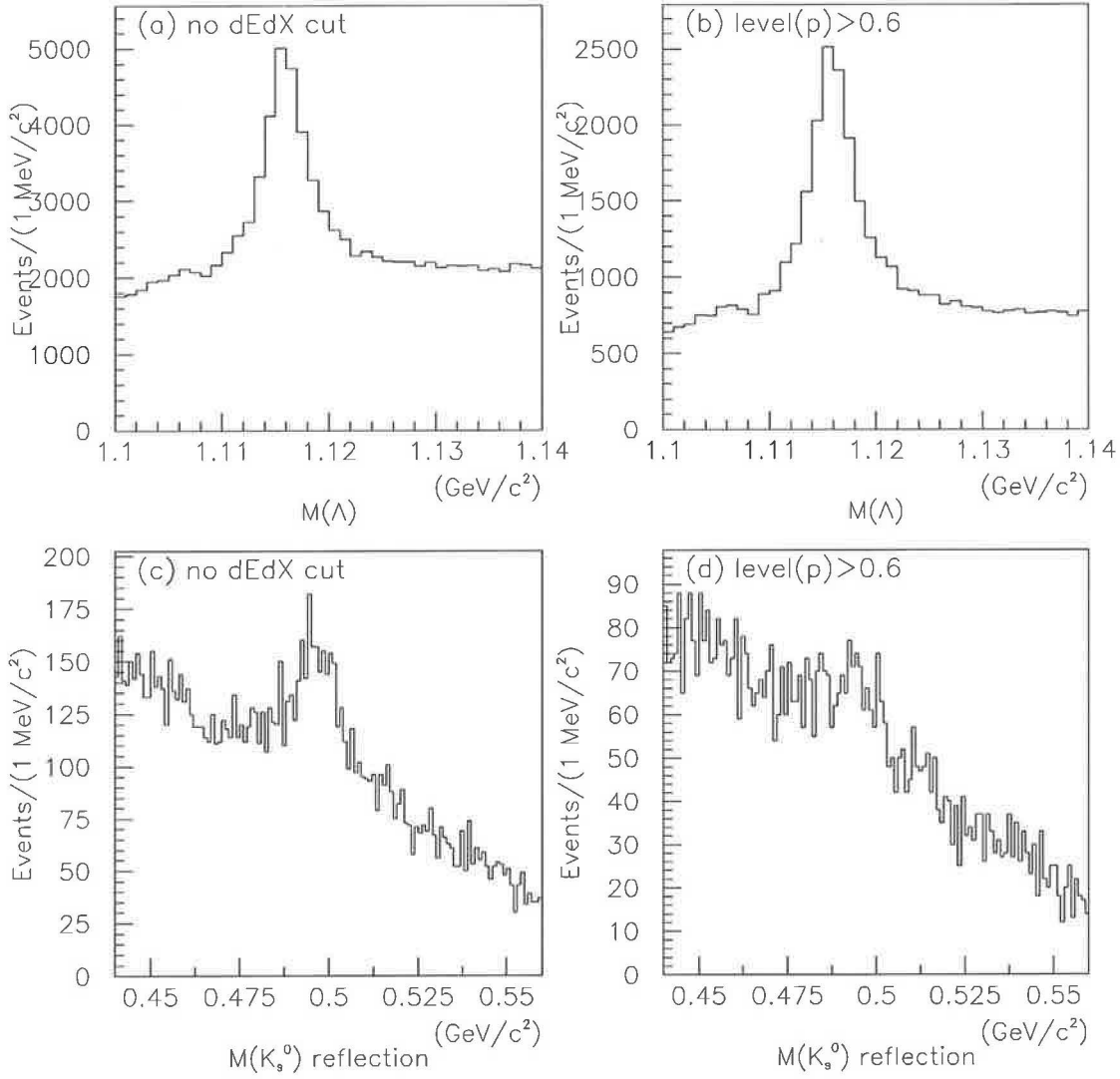


Figure A.6: (a) and (c): the $M(\Lambda)$ and its K_s^0 reflection without dE/dX cut. (b) and (d): the $M(\Lambda)$ and its K_s^0 reflection with $\text{level}(p) > 0.6$. The K_s^0 reflection is reduced significantly.

Bibliography

- [1] C. L. Cowan, *et. al.*, Science **124**, 103 (1956).
- [2] J. Chadwick, Proc. Roy. Soc. **A136**, 692 (1932).
- [3] R. P. Feynman, M Gell-Mann, “Theory of Fermi Interaction.” Phys. Rev. **109**, 193 (1958).
- [4] E. C. G. Sudarshan, R. E. Marshak, “Chirality Invariance and the Universal Fermi Interaction.” Phys. Rev. **109**, 1860 (1958).
- [5] H. Yukawa, “On the Interaction of Elementary Particles. I.” Proc. Phys-Math. Soc. Jap. **17**, 48 (1935).
- [6] S. H. Neddermeyer, C. D. Anderson, “Note on the Nature of Cosmic-Ray Particles.” Phys. Rev. **D51**, 884 (1937).
- [7] G. P. S. Occhialini, C. F. Powell, “Nuclear Disintegrations Produced by Slow Charged Particles of Small Mass.” Nature **159**, 186 (1947).
- [8] G. Danby, J. M. Gaillard, K. Goulianos, L. M. Lederman, N. Mistry, M. Schwartz, J. Steinberger, “Observation of High-Energy Neutrino Reactions and the Existence of Two Kinds of Neutrinos.” Phys. Rev. Lett. **9**, 36 (1962).

- [9] M. L. Perl, *et. al.*, “Evidence For Anomalous Lepton Production In $E^+ - E^-$ Annihilation.” *Phys. Rev. Lett.* **35**, 1489 (1975).
- [10] M. L. Perl, *et. al.*, “Properties Of Anomalous $E \mu$ Events Produced In $E^+ E^-$ Annihilation.” *Phys. Lett.* **63B**, 466 (1976).
- [11] M. Gell-Mann, “The Eightfold Way: A Theory of Strong Interaction Symmetry.” Caltech Internal Note CTSL-20(1961), unpublished.
- [12] Y. Neeman, “Derivations of Strong Interactions from a Gauge Invariance.” *Nucl. Phys.* **26**, 222 (1961).
- [13] E. D. Bloom *et. al.*, “High-Energy Inelastic $E P$ Scattering At 6-Degrees And 10-Degrees.” *Phys. Rev. Lett.* **23**, 930 (1969).
- [14] M. Breidenbach *et. al.*, “Observed Behavior Of Highly Inelastic Electron - Proton Scattering.” *Phys. Rev. Lett.* **23**, 935 (1969).
- [15] N. Cabibbo, “Unitarity Symmetry and Leptonic Decays.” *Phys. Rev. Lett.* **10**, 531 (1963).
- [16] S. L. Glashow, J. Iliopoulos, I. Maiani, “Weak Interaction with Lepton-Hadron Symmetry.” *Phys. Rev.* **D2**, 1285 (1970).
- [17] J. E. Augustin *et. al.*, “Discovery of a Narrow Resonance in e^+e^- Annihilation.” *Phys. Rev. Lett.* **33**, 1406 (1974).
- [18] C. Bacci *et. al.*, “Preliminary Result of Frascati(ADONE) on the Nature of a New 3.1 GeV Particle Produced in e^+e^- Annihilation.” *Phys. Rev. Lett.* **33**, 1408 (1974).
- [19] M. Kobayashi, K. Maskawa, “CP Violation in the Renormalizable Theory of Weak Interaction.” *Prog. Theor. Phys.* **49**, 652 (1973).

- [20] S. W. Herb *et. al.*, “Observation of a Dimuon Resonance at 9.5 GeV in 400 GeV Proton-Nuclear Collisions.” *Phys. Rev. Lett.* **39**, 252 (1977).
- [21] F. Abe. *et. al.* CDF Collaboration, “Evidence for Top Quark Production in $p\bar{p}$ Collisions at $\sqrt{s} = 1.8$ TeV.” *Phys. Rev.* **D50**, 2966 (1994).
- [22] L. Wolfenstein, “Parametrization of the Kobayashi Maskawa Matrix.” *Phys. Rev. Lett.* **51**, 1945 (1983).
- [23] A. D. Martin, R. G. Roberts, W. J. Stirling, “Parton Distribution Updated.” *Phys. Lett.* **B306**, 145 (1993).
- [24] A. D. Martin, R. G. Roberts, W. J. Stirling, “New information on parton distributions.” *Phys. Rev.* **D47**, 867 (1993).
- [25] J. Botts *et. al.* CTEQ Collaboration, “CTEQ Parton Distributions and Flavor Dependence of Sea Quarks.” *Phys. Lett.* **B304**, 159 (1993).
- [26] P. Nason, S. Dawson, R. K. Ellis, “The One Particle Inclusive Cross Section for Heavy Quark Production in Hadronic Collisions.” *Nucl. Phys.* **B327**, 49 (1989).
- [27] C. Peterson, D. Schlatter, I. Schmitt, and P. M. Zerwas, “Scaling Violations in Inclusive e^+e^- Annihilation Spectra.” *Phys. Rev.* **D27**, 105 (1983).
- [28] J. Chrin, “Upon the Determination of Heavy Quark Fragmentation Functions in e^+e^- Annihilation.” *Z. Phys.* **C36**, 163 (1987).
- [29] C. Caso *et. al.* Particle Data Group, “Review of Particle Physics.” *Eur. Phys. J.* **C3**, 1 (1998).

- [30] J. Alcaraz *et. al.* LEP B Lifetime Group, “Averages of B Hadron Lifetimes.”
<http://wwwcn.cern.ch/~claires/lepblife.html>.
- [31] M. Neubert, “Heavy quark Symmetry.” *Phys. Rep.* **245**, 259 (1994).
- [32] M. Neubert, C. T. Sachrajda, “Spector Effects in Inclusive Decays of Beauty Hadrons.”
Nucl. Phys. **B483**, 339 (1997).
- [33] I. I. Bigi, B. Blok, M. Shifman, N. Uraltsev, and A. Vainshtein, “Non-Leptonic Decays of Beauty Hadrons – from Phenomenology to Theory.” In *B Decays*, edited by S. Stone, Second Edition (World Scientific, Singapore, 1994), p. 132.
- [34] D. Buskulic *et. al.* ALEPH Collaboration, “Measurement of the b Baryon Lifetime and Branching Fractions In Z Decays.” *Eur. Phys. J.* **C2**, 197 (1998).
- [35] P. Abreu *et. al.* DELPHI Collaboration, “Measurement of the Lifetime of b-baryons.”
 CERN-PPE/99-016. Submitted to *Eur. Phys. J. C*.
- [36] R. Akers *et. al.* OPAL Collaboration, “Measurement of the Average b-Baryon Lifetime and the Product Branching Ratio $f(b \rightarrow \Lambda_b) \cdot BR(\Lambda_b \rightarrow \ell^- \bar{\nu} X)$.” *Zeit. Phys.* **C69**, 195 (1996).
- [37] R. Akers *et. al.* OPAL Collaboration, “Measurement of the B_s^0 and Λ_b Lifetime.” *Phys. Lett.* **B426**, 161 (1998).
- [38] F. Abe *et. al.* CDF Collaboration, “Measurement Of The Λ_b Lifetime Using $\Lambda_b \rightarrow \Lambda_c^+ \ell^- \bar{\nu}$.”
Phys. Rev. Lett. **77**, 1439 (1996).
- [39] J.D. Richman, Proceedings of the 28th International Conference on High Energy Physics, 25-31 July 1996, Warsaw, Poland

- [40] M. Neubert, Invited talk presented at the Second International Conference on B Physics and CP violation, Honolulu, Hawaii, 24-27 March 1997
- [41] D. Mohl, G. Petrucci, L. Thorndahl and S. van der Meer, "Physics and Technique of Stochastic Cooling." Phys. Rep. **58**, 73 (1980).
- [42] F. Abe *et. al.*, "The CDF detector: An Overview." Nucl. Instrum. Meth. **A271**, 387 (1988).
- [43] D. Amidei *et. al.*, "The Silicon Vertex Detector of the Collider Detector at Fermilab." Nucl. Instrum. Meth. **A350**, 73 (1994).
- [44] F. Bedeschi *et. al.*, "Design and Construction of the CDF Central Tracking Chamber." Nucl. Instrum. Meth. **A268**, 50 (1988).
- [45] L. Balka *et. al.*, "The CDF Central Electromagnetic Calorimeter." Nucl. Instrum. Meth. **A267**, 272 (1988).
- [46] L. Nodulman *et. al.*, "Central Shower Counter Prototype for the Fermilab Collider Detector Facility." Nucl. Instrum. Meth. **A204**, 351 (1983).
- [47] S. Bertolucci *et. al.*, "The CDF Central and Endwall Hadron Calorimeter." Nucl. Instrum. Meth. **A267**, 301 (1988).
- [48] G. Ascoli *et. al.*, "CDF Central Muon Detector." Nucl. Instrum. Meth. **A268**, 33 (1988).
- [49] D. Amidei *et. al.*, "The CDF Trigger." Nucl. Instrum. Meth. **A265**, 326 (1988).
- [50] N. Ellis, A. Kernam, "Heavy Quark Production at the CERN $p\bar{p}$ Collider." Phys. Rep. **195**, 23 (1990).

- [51] F. Bedeschi, S. Dell’Agnello , “Combining the Primary Vertex Finder with the SVX Beam Line Measurement.” cdf note **2055**.
- [52] F. Bedeschi, S. Dell’Agnello , “Handling multiple primary interactions with the Primary Vertex Finder.” cdf note **2084**.
- [53] F. Abe *et. al.* CDF Collaboration, “Measurement of the antiproton-proton total cross section at $\sqrt{s} = 546$ and 1800 GeV.” Phys. Rev. **D50**, 5550 (1994).
- [54] N. Solomey, A. B. Wicklund, “Study of Electromagnetic Showers in the CDF Central electromagnetic Calorimeter.” cdf note **247**.
- [55] M. Gold , “Identification of Conversion Electron Pairs.” cdf note **913**.
- [56] P. Sphicas, “A $b\bar{b}$ Monte Carlo Generator.” cdf note **2655**.
- [57] N. Isgur *et. al.*, “Semileptonic B and D Decays in the Quark Model.” Phys. Rev. **D39**, 799 (1989).
- [58] J. Lewis, P. Avery, “CLEOMC: The CDF Interface to the CLEO Monte Carlo (QQ).” cdf note **2724**.
- [59] M. Shapiro *et. al.*, “A User’s Guide to QFL.” cdf note **1810**.
- [60] J. Marriner, “Secondary Vertex Fit.” cdf note **1996**.
- [61] D. Cinabro, *et. al.* CLEO Collaboration, “A Study Of Baryon Production In B Decay : Search For Semileptonic Decays Of B Mesons To Charmed Baryons And The First Observation Of Ξ_c Production In B Decay.” CLEO-CONF-94-8 (1994).

- [62] J. Tseng, B. Barnett, J. Skarha, T. Miao, "Observation of Bottom Baryon Semileptonic Decay." cdf note **3353**.
- [63] F. James, "MINUIT - Function Minimization and Error Analysis." CERN Program Library Logn Wirteup D506 (1994).
- [64] M. D. Peters, "Run 1B dE/dX Corrections." cdf note **3807**.